Mapping Functional Riparian Zones in Agricultural Watershed Using LiDAR and Photogrammetry Methods

by

Joan Grau

BSc. Biology, Autonomous University of Barcelona, 2011

A Thesis Submitted in Partial Fulfillment
of the Requirements for the Degree of

Master of Science in Forestry

in the Graduate Academic Unit of
Forestry and Environmental Management

Supervisors: Fan-Rui Meng, PhD, Forestry & Environmental Management
Bonnie J. Robertson, P.Eng., Agriculture & Agri-Food Canada

Examining Board: Charles Bourque, PhD, Forestry & Environmental Management
Sheng Li, PhD, Agriculture & Agri-Food Canada
Yun Zhang, PhD, Geodesy & Geomatics Engineering

This thesis is accepted by the
Dean of Graduate Studies

THE UNIVERSITY OF NEW BRUNSWICK

October 2021

ABSTRACT

This thesis reports on a new photogrammetry method to map functional riparian areas across agricultural watersheds, developed near Havelock, New Brunswick. The main objective was to assess the feasibility of using consumer-grade Unmanned Aerial Vehicles (UAV) as means of predicting the extents of this ecotone. To do so, we explored how to optimally set flight parameters, such as image overlap, pre-planned flight grid, flight height, and the camera angle for image reconstruction and successful 3D point extraction.

Near ground aerial images were collected during different seasons over the study site. These images were used to map the variability in the field conditions, including watercourses and riparian vegetation. We also generated a UAV-photogrammetric digital elevation model (DEM), which was compared to Service New Brunswick Geospatial datasets (Coarse resolution with average point spacing of 70 meters and LiDAR-derived DEMs, at 1.2 points/m^2 and 6 points/m^2).

The coarse resolution DEM was interpolated at a 2 meter cell size, whereas LiDAR and UAV-derived DEMs were interpolated at a 30cm cell size. We used these topographic models to estimate the surface area occupied by stream channels, using the Slope Gradient (SG) raster and the Vertical Slope Position (VSP). Furthermore, we tested the accuracy of these topographic models in predicting the extents of the functional riparian area using the Vertical Distance To Channel Network (VDTCN).

We found that the UAV-derived DEM achieved the best accuracy in predicting the area occupied by stream channels when the SG was used, followed by LiDAR collected at 6 points/m^2 (LiDAR 6.0), with mean squared errors (MSE) of 1.81 and 1.91, respectively.

We also found that LiDAR and UAV-derived DEMs achieved 63% agreement (as measured in Kappa Coefficient) in predicting the extents of functional riparian areas, even though the UAV provided higher terrain detail. However, coarse resolution DEM did not provide accurate topographic detail for estimating the channel surface area nor the functional riparian zone extents.

The results presented herein proved that UAVs were an accurate and economic means for prediction, management, assessment, and monitoring of riparian ecosystems over agricultural landscapes.

ACKNOWLEDGEMENTS

I would like to sincerely thank Dr. Fan-Rui Meng, PhD, supervisor of this project and the Professor of hydrology and watershed management at UNB, for his continued guidance, support, and insight throughout the field of remote sensing and wet areas mapping. I also wish to thank Jae Ogilvie, Research Associate and Director of Geomatics Developments at UNB for his technical assistance and project guidance throughout my progress.

I want to thank Bonnie Robertson, water resources engineer at Agriculture and Agri-food Canada (AAFC) for the opportunity to learn from the functional riparian zone variable buffers, to mitigate the environmental problem in Atlantic Canada in agricultural landscapes, and the continuous financial support through this Government organization. Especial thanks to Robert Hicks and Amalia David for allowing me to conduct this research on their farm, and for their flexibility in scheduling visits to their farm during my data collection.

I would like to show my gratitude to Kang Liang for the guidance provided in the statistical analysis, and Fangzhou Zheng for data acquisition and for sharing his photogrammetry knowledge in the field of agriculture.

I would like to recognize Mohammad Rezaee for the help provided in Remote Sensing and Photogrammetry analysis. Thanks to Madisyn Harper for her assistance in field tasks, coordinating the logistics of this project, arranging material for field tasks, and the technical help provided.

Finally, a special thanks to the chair of the Forest Watershed center, Dr. Paul Arp for encouraging me to undertake studies in this research field.

Table of Contents

List of Tables

List of Figures

List of Symbols, Nomenclature or Abbreviations

AAFC: Agriculture and Agri-Food Canada

AGB: Aboveground biomass

AGL: Above Ground Level

ALS: Aerial Laser Scanning

ASL: Above mean Sea Level

CMOS: Complementary Metal Oxide Semiconductor

CSAs: Critical Source Areas

DEM: Digital Elevation Model

DSM: Digital Surface Model

DTM: Digital Terrain Model

DTW: Depth-To-Water

FOV: Field of View

FRDC: Fredericton Research and Development Center

GPS: Global Positioning System

GSD: Ground Sample Distance

GWL: Groundwater Level

HSAs: Hydrologic Sensitive Areas

IDW: Inverted Distance Weighted

KGE: Kling-Gupta Efficiency

LAI: Leave Area Index

LiDAR: Light Detection and Ranging

MRE: Mean Relative Error

MSE: Mean Squared Error

RFAP: Riparian Function Assessment Protocol

RMSE: Root Mean Squared Error

ROC: Receptive Operating Curves

R^2: Coefficient of Regression

SD: Standard Deviation

SD-card: Secure Digital Card.

SG: Slope Gradient

VDTCN: Vertical Distance To Channel Network

VSP: Vertical Slope Position

UAV: Unmanned Aerial Vehicle

UNB: University of New Brunswick

WGS: World Geodetic System

CHAPTER 1: Introduction

1. 1. Riparian zone functions and human alterations

Riparian zones define particular vegetation communities and support a unique complex ecosystem with distinctive resource values within a watershed. Many terrestrial species travel through or settle for a short period of their life cycles as they seek suitable shelter in riverine ecotones (Wipfli, 1997; Forman, 1995). The surrounding trees and plants provide important food sources for aquatic insects that are themselves the main food source in the aquatic food chain. The riparian ecosystem also creates ideal habitat for insects, as well as refuge for birds (Peak & Thompson, 2006), small mammals (Steel *et al*., 1999) and large mammals (Osbourne *et al*., 2005), and forest-floor invertebrates (Rykken *et al*., 2007). The shoreline vegetation offers shade and wind protection that helps regulate water temperature (Sridhar *et al*., 2004; Cassie, 2006; Garner *et al*., 2014; Kalny *et al*. 2017).

Riparian zones play a vital role in the health of water bodies by reducing pollution, stabilizing banks and buffering surface water flows. Riparian plant species, or phreatophytes, have specific adaptations traits, such as adventitious roots, predominantly into or below the capillary fringe and saturated zone. This fact allows them to feed on water obtained directly from the stream, or from groundwater in the alluvial aquifer. As a consequence, this deep-binding root structure can help improving the stream bank stability. The deep rooting system can also increase soil pore space and increase soil infiltration capacity, which in turn, help in reducing the risk of flood and minimizing soil erosion. The high infiltration capacity of a deep rooting system can also help to absorb and dissipate water energy during floods (Marti et al. 2000; Micheli & Kirchner, 2002). Previous

research also concluded that riparian buffer zones can help reduce chemical pollution (Meehan *et al*., 1977; Swanson *et al*., 1982; Dabney *et al*., 2006).

Due to their fertile soil and particular position in the landscape, most common disturbances to riparian areas are related to land use activities, such as agricultural crop production or timber harvesting. These activities can not only strip the riparian zone vegetation, but also lead to soil compaction and an increase in suspended solid concentrations that can propagate downstream (Story *et al*. 2003; Feller 2005; Wilkerson *et al*., 2006; Bisson *et al*., 1987; Bilby & Ward, 1991).

Removal of vegetative shelter at the water's edge can lead to a rise in water temperatures by increasing the sunlight reaching the stream (Virgona *et al*., 2006). This intensified sunlight coupled with increased nutrient export (as a consequence of fertilizer use in agricultural activities), could promote a substantial rise in primary production and induce eutrophication (Feller, 2005; Bladon *et al*., 2008).

Livestock grazing in riparian areas for extended periods can reduce the overall vegetation cover and minimize competition, which can offer opportunities for upland plant species to move into the riparian zone (Morgan *et al*., 2008). However, these upland vegetation species are not adapted to waterlogged environments and do not have the extensive rooting system to protect stream banks against the impacts of flooding (Garssen *et al*., 2015). The disturbed riparian zone could accelerate channel erosion during subsequent periods of high flow (Sedell & Beschta, 1991).

1. 2. The need for precise mapping techniques

The success of riparian management strategies requires accurate mapping of the whole ecosystem's matrix in order to make effective management decisions. Firstly, defining the stream channel shape is crucial to locate where this riparian forest begins. The stream's dynamic change represents an important influence on channel morphology, particularly on the variability in the volume, also referred to as the magnitude. This dynamic variation over time is a result of the frequency, duration, and timing of water delivered to a stream, as well as its pattern. Ultimately, this variation can lead to constant changes in the channel width, depth, sinuosity, riffle spacing, etc. (Poff *et al*.,1997). In many cases, the size of the riparian zone is related to the size of the stream channel, the position of stream within the watershed, and the hydrologic regime (Puckridge *et al*., 1998; Lytle & Poff, 2004; Lind *et al*., 2014).

Watershed models often require physiographic information such as configuration of the channel network, channel length, channel slope, watershed boundaries, and subcatchment geometric properties. Traditionally, these parameters are obtained from maps or field surveys, which becomes time consuming, expensive, and difficult in vast watersheds. Over the past few decades, mapping the potential extents of the channel surface has been achieved with some success with the use of digital elevation models (DEMs) for larger river basins (Mark, 1984; Freeman, 1991; Montgomery & Foufoula-Georgiou, 1993). Unfortunately, the performance of previous methods was poor when used to reproduce areas with narrower streams, which is limited by mapping resolution, i. e. coarse resolution DEMs (Fairfield & Leymarie, 1991; Garbrecht & Martz, 1994). In addition, because stream channels are influenced by constant erosion and sedimentation processes,

DEMs can become rapidly outdated, since they cannot reflect these ongoing changes (Smart *et al*., 2001; Abood, 2012; Fernández *et al*., 2012).

In recent years, LiDAR (Light Detection and Ranging) has had an impact on the accuracy of DEM horizontal and vertical resolutions in extracting geomorphological and hydrological data (Rocha *et al*., 2020). These LiDAR-derived DEMs can locate the stream path and detect the ephemeral streams more accurately since they can represent terrain models more precisely. This fact enables better hydraulic analyses of the channel detailing better stream geometries relevant for modelling overland flows (Cobby *et al*., 2003; Sharpley *et al*., 2000; Sonneveld *et al*., 2006). However, LiDAR datasets are periodically updated every five years and the costs of data collection and post-processing steps become dramatically expensive due to the need for trained personnel and costly equipment.

Alternatively, unmanned aerial vehicles (UAV) have been widely used in agriculture to collect data in order to help increase crop production, to enhance profitability, and to reduce environmental impacts to farmland (Xiang & Tiang, 2011). UAV technology provides an alternative fast and inexpensive method to obtain high resolution DEMs using photogrammetry methods (Bevanda *et al*., 2014; Corbane *et al*., 2015). Nonetheless, information on how to set optimal flight parameters, such as image overlap, pre-planned flight grids, flight height, and camera angle for image reconstruction and successful 3D point extraction have not yet been explored in detail (Pajares, 2016; Liu *et al*., 2018).

1. 3. Research objectives

The long-term objective of the proposed project is to develop a GIS-based decision support tool to assess the goods and services provided by riparian areas using a function-

based approach, incorporating information regarding nutrient removal, differences in plant functional communities, earthworm population, soil Carbon, pollinator habitat, and changes in macroinvertebrate communities, as well as locating at-risk areas on the agricultural landscape where better riparian management would benefit the landowner, or where agricultural practices could be altered to reduce direct impacts to the riparian area. This tool will ultimately result in reducing impacts to surface water from agricultural practices.

The specific objectives of the present study include:

1. Estimate optimal UAV data collection parameters, including flight height, image overlap rate and camera angles.
2. Develop a model to predict stream channel boundary and area using digital elevation model data collected with a UAV photogrammetry method.
3. Develop a method for the prediction of functional riparian zone boundaries in narrow streams based on selected DEMs data using the Vertical Distance to Channel Network (VDTCN).
4. Conduct field validation of riparian zones based on DEMs with vegetation indicators, soil survey, and near ground aerial photos.

1. 4. Thesis overview

The thesis was organized into five chapters as shown in Figure 1.1.

Chapter 1 defines the current problem in agriculture landscapes in regards to riverine ecosystems' protection in Atlantic Canada. Secondly, it provides background information for the impacts of the DEM resolution in detecting the boundaries of small streams and

how riparian areas have been classified in past studies. Finally, the objectives of this thesis have been defined.

Chapter 2 outlines my research on the UAV method, and defines the optimal parameters for UAV data collection. It also analyzes and compares optimal UAV configurations to undergo a detailed point cloud analysis and understand the potential distortions prior to generating the datasets needed in this study. It documents the best camera angle and image overlap to be used to estimate the volume, height, and area of a measurable object.

I tested three hypotheses in this chapter:

Hypothesis 1: Lower flight heights produce higher point cloud densities than higher flight heights.

Hypothesis 2: A larger number of vertical camera angles results in more precise estimates of the variables measured (height, area and volume of a measurable object).

Hypothesis 3: Greater image overlap increases both the accuracy and the computer processing time.

Chapter 3 analyses the impact the topographic detail of the different DEMs used has in estimating the stream channel width boundaries and quantifying the surface area occupied by channels within an agricultural watershed, when using the Slope Gradient (SG) raster and the Vertical Slope Position (VSP) methods. Hypothesis: Higher resolution DEMs can estimate the stream channel area with higher accuracy.

Chapter 4 details the accuracy of the DEMs used in this study in classifying functional riparian zones in the main study site, using the Vertical Distance to Channel Network

(VDTCN) method. Hypothesis: Higher resolution DEMs provide more topographic detail to predict the functional riparian area extension.

Chapter 5 summarizes the conclusions of this study, details potential applications and gives some direction for future work.

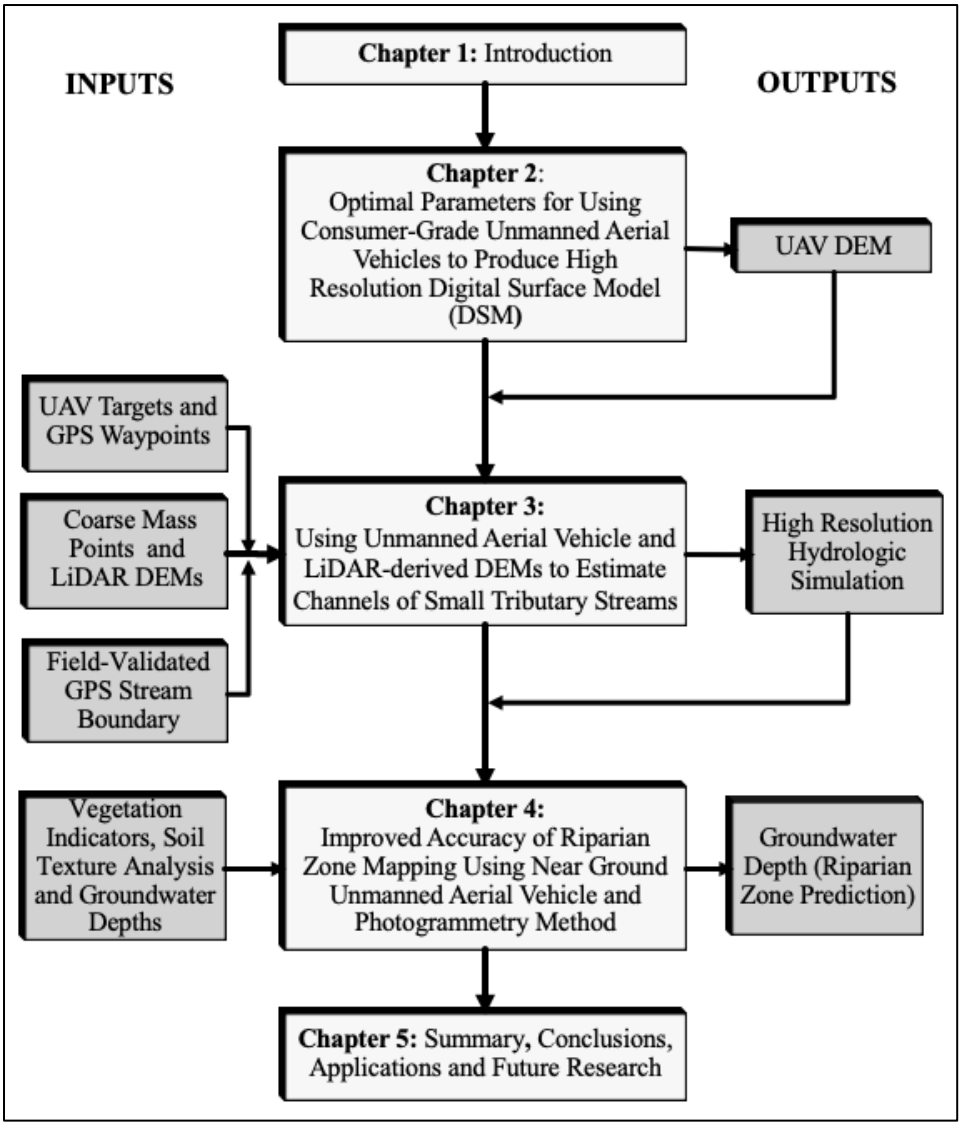

Figure 1.2. Thesis flow chart

References

Abood, S. A., Maclean, A. L., Mason, L. A. 2012. Modeling riparian zones utilizing dems and flood height data. Photogrammetric Engineering and Remote Sensing, 78, 259–269.

Bevanda, M., Horning, N., Reineking, B., Heurich, M., Wegmann, M., Mueller, J. 2014. Adding Structure to Land cover–Using Fractional Cover to Study Animal Habitat Use. Movement Ecology 2 (1): 26. https://doi:10.1186/s40462-014-0026-1

Bilby, R. E., Ward, J. W. 1991. Characteristics and function of large woody debris in streams draining old-growth, clear-cut, and 2nd-growth forests in southwestern Washington. Canadian Journal of Fisheries and Aquatic Sciences 48:2499–2508.

Bisson, P. A., Bilby, R. E., Bryant, M. D., Dolloff, C. A., Grette, G. B., House, R. A., Murphy, M. L., Koski, K. V., Sedell, J. R. 1987. Large woody debris in forested streams in the Pacific Northwest past, present, and future. In: Salo EO, Cundy TW (eds) Streamside management, forestry and fishery interactions. University of Washington Press, Seattle, pp 143–190.

Bladon, K. D., Silins, U., Wagner, M. J., Stone, M., Emelko, M. B., Devito, K. J., Mendoza, C. A., Boon, S. 2008. Wildfire impacts on nitrogen export and production from headwater streams in southern Alberta's Rocky Mountains. Canadian Journal of Forest Research 38: 2359–2371.

Bock, M., Köthe, R., 2008. Predicting the depth of hydromorphic soil characteristics influenced by ground water. Hamburger Beiträge zur Physischen Geographie und Landschaftsökologie, 19, pp.13–22.

Boehner, J., Koethe, R., Conrad, O., Gross, J., Ringeler, A., Selige, T. 2002. Soil Regionalisation by Means of Terrain Analysis and Process Parameterisation. In: Micheli, E., Nachtergaele, F., Montanarella, L. [Ed.]: Soil Classification 2001. European Soil Bureau, Research Report No. 7, EUR 20398 EN, Luxembourg. pp.213-222.

Boochs, F., Kupfer, G., Dockter, K., Kühbauch, W. 1990. Shape of the red edge as vitality indicator for plants, International Journal of Remote Sensing, 11:10, 1741-1753, https://10.1080/01431169008955127

Buchanan, B. P., Fleming, M., Schneider, R. L., Richards, B. K., Archibald, J., Qiu, Z., Walter, M. T. 2014. Evaluating topographic wetness indices across central New York agricultural landscapes, Hydrol. Earth Syst. Sci., 18, 3279-3299, https://doi.org/10.5194/hess-18-3279-2014

Cassie, D. 2006. The thermal regime of rivers: A review. Freshwater Biology 51: 1389–1406.

Cobby, D.M., Mason, D. C., Horritt, M.S., Bates, P. D. 2003. Two-dimensional hydraulic flood modelling using a finite element mesh decomposed according to vegetation and topographic features derived from airborne scanning laser altimetry. Hydrological Processes, 17. pp. 1979-2000.

Cooper, J. R., Gilliam, J. W., Daniels, R. B., Robarge, W. P. 1987. Riparian areas as filters for agricultural sediment. Journal of Soil Science Society America 51:416-420.

Corbane, C., Lang, S., Pipkins, K., Alleaume, S., Deshayes, M., Millán, V. E. G., Strasser, T., Borre, J. V., Toon, S., Michael, F. 2015. Remote Sensing for Mapping Natural Habitats and Their Conservation Status – New opportunities and Challenges. International Journal of Applied Earth Observation and Geoinformation 37: 7–16. https://doi:10.1016/j.jag.2014.11.005

Dabney, S. M., Moore, M. T., Locke, M. A. 2006. Integrated Management of in-Field, Edge-of-Field, and after-Field Buffers. Journal of The American Water Resources Association 42(1):15-24.

Fairfield, J., Leymarie, P. 1991. Drainage Networks from Grid Digital Elevation Models. Water Resources Research, 30(6):1681-1692.

Feller, M. C. 2005. Forest harvesting and streamwater inorganic chemistry in western North America: a review. Journal of the American Water Resources Association 41:785–811.

Fernández, D., Barquín, J., Álvarez-Cabria, M., Peñas, F. J. 2012. Quantifying the performance of automated GIS-based geomorphological approaches for riparian zone delineation using digital elevation models, Hydrol. Earth Syst. Sci., 16, 3851-3862 https://doi.org/10.5194/hess-16-3851-2012

Forman, R. T. T. 1995. Land mosaics: The ecology of landscapes and regions. Cambridge Univ. Press, Cambridge, UK.

Freeman, G. T. 1991. Calculating catchment area with divergent flow based on a regular grid, Comput. Geosci., 17, 413– 422.

Fu, B., Li, Y., Wang, Y., Campbell, A., Zhang, B., Yin, S., Zhu, H., Xing, Z., Jin, X. 2017. Evaluation of riparian condition of Songhua River by integration of remote sensing and field measurements. Scientific Reports 7, Article number: 2565.

Gallant, J. C., Dowling, T. I. 2003. A multiresolution index of valley bottom flatness for mapping depositional areas. Water Resources Research, 39(12), 1347.

Garbrecht, J., Martz, L. W. 1994. Grid size dependency of parameters extracted from digital elevation models. Comput Geosci 20:85–87.

Garner, G., Malcolm, I. A., Sadler, J. P., Hannah, D. M. 2014. What causes cooling water temperature gradients in a forested stream reach? Hydrol Earth Syst Sci 18: 5361–5376.

Garssen, A. G., Baattrup-Pedersen, A., Voesenek, L. A. C. J., Verhoeven, J. T. A., Soons, M. B. 2015. Riparian plant community responses to increased flooding: a meta-analysis. Global Change Biology, 21(8), 2881-2890. https://doi.org/10.1111/gcb.12921

Gregory, S. V., Swanson, F. V., McKee, W. A., Cummins, K. W. 1991. An ecosystem perspective of riparian zones. BioScience 41; 540-551.

Han, L., Huang, W., Yuan, X., Zhao, Y., Ma, Z., Qin, J. 2017. Denitrification Potential and Influencing Factors of the Riparian Zone Soils in Different Watersheds, Taihu Basin. Water Air Soil Pollut. 228, 108. https://doi.org/10.1007/s11270-017-3287-7

Hengl, T., Reuter, H. I. 2008. Geomorphometry: Concepts, Software, Applications**.** Developments in Soil Science, vol. 33, Elsevier, 211-218 pp.

Hickey, M. B. C., Doran, B. 2004. A review of the efficiency of buffer strips for the maintenance and enhancement of riparian ecosystems. Water Quality Research Journal of Canada 39:311-317.

Kalny, G., Laaha, G., Melcher, A., Trimmel, H., Weihs, P., Rauch, H. P. 2017. The influence of riparian vegetation shading on water temperature during low flow conditions in a medium sized river Knowl. Manag. Aquat. Ecosyst., 418 (2017) 5 https://doi.org/10.1051/kmae/2016037

Kasi, V., Botter, B. 1994. Streambank fencing for the remediation of agricultural nonpoint source pollution. Pages 301-305. In: Riparian Ecosystems in the Humid U.S.: Functions, Values, and Management. Proceedings of a conference March 15-18, 1993. Atlanta Ga. National Association of Conservation Districts. Washington, D.C. 445 pages.

Lind, L., Nilsson, C., Polvi, L. E., Weber, C. 2014. The role of ice dynamics in shaping vegetation in flowing waters Biological Reviews. https://doi.org/10.1111/brv.12077

Liu, J., Skidmore, A. K., Jones, S. D., Wang, T., Heurich, M., Zhu, X., Shi, Y. 2018. Large off-nadir scan angle of airborne LiDAR can severely affect the estimates of forest structure metrics. ISPRS journal of photogrammetry and remote sensing, 136, 13-25. https://doi.org/10.1016/j.isprsjprs.2017.12.004

Lovell, S. T., Sullivan, W. C. 2005. Environmental benefits of conservation buffers in the United States: evidence, promise, and open questions. Agr Ecosyst Environ.;112:249–60.

Lozano de Sosa, L., Glanville, H. C., Marshall, M. R., Abood, S. A., Williams, A. P., Jones, D. L. 2017. Delineating and mapping riparian areas for ecosystem service assessment. Ecohydrology Vol 11, Issue 2. https://doi.org/10.1002/eco.1928

Lytle, D. A., Poff, N. L. 2004. Adaptation to natural flow regimes. Trends in Ecology & Evolution. Vol 19, Issue 2, pp 94-100.

Mark, D. M. 1984. Automated detection of drainage networks from digital elevation models, Cartographica, 21, 168– 178.

Marti, E., Fisher, S.G., Schade, J. D., Grimm, N. B. 2000. Flood frequency and stream-riparian linkages in arid lands. In: Jones, J.B. and P.J. Mulholland (eds.), Streams and Ground Water. Academic Press. New York, NY. pp. 111-136.

Meehan, W.R., Swanson, F. J., Sedell, J. R. 1977. Influences of riparian vegetation on aquatic ecosystem with particular reference to salmonid fishes and their food supply. In: Importance, Preservation and Management of Riparian Habitat. USDA Forest Serv. Gen. Tech. Rep. RM-43: 137- 643.

Micheli, E. R., Kirchner, J. W. 2002. Effects of wet meadow riparian vegetation on streambank erosion. 2 measurements of vegetated bank strength and consequences for failure mechanics. Earth Surf. Process. Landforms 27, 687-697.

Montgomery, D. R., Foufoula-Georgiou, E. 1993. Channel network source representation using digital elevation models, Water Resour. Res., 29, 3925– 3934.

Moore, I.D., Grayson, R.B., Ladson, A.R. 1991. Digital Terrain Modelling: A Review of Hydrological, Geomorphological, and Biological Applications. Hydrological Processes, 5, 3-30. https://doi.org/10.1002/hyp.3360050103

Morgan, J.; Ferris, G.; Williams, C.; D'Amico, V. 2008. Excluding invasive plants with riparian corridors. In: McManus, K.A; Gottschalk, K.W., eds. Proceedings, 19th U.S. Department of Agriculture Interagency Research Forum on Invasive Species, 2008. Gen. Tech. Rep. NRS-P-36. Newtown Square, PA: U.S. Department of Agriculture, Forest Service, Northern Research Station.

National Research Council. 2002. Riparian Areas: Functions and Strategies for Management. Washington, DC: The National Academies Press. https://doi.org/10.17226/10327

Nobre, A. D., Cuartas, L. A., Hodnett, M., Rennó, C. D., Rodrigues, G., Silveira, A., Waterloo, M., Saleska, S. 2011. Height Above the Nearest Drainage-a hydrologically relevant new terrain model. Journal of Hydrology, 404(1-2), 13-29. https://doi.org/10.1016/j.jhydrol.2011.03.051

Osbourne, J. D., Anderson, J. T., Spurgeon, A. B. 2005. Effects of Habitat on Small-Mammal Diversity and Abundance in West Virginia. Wildlife Society Bulletin 33(3):814-822.

Pajares, G. 2015. Overview and current status of remote sensing applications based on unmanned aerial vehicles (UAVs) Photogramm. Eng. Remote Sens. 2015;81:281–329. https://doi:10.14358/PERS.81.4.281

Parish Geomorphic. 2007. Design Brief for the Ridge Brook Restoration, Lloyd Alward Farm, Hicksville, New Brunswick.

Peak, R. G., Thompson, F. R. 2006. Factors Affecting Avian Species Richness and Density in Riparian Areas. Journal of Wildlife Management 70(1):173-179.

Poff, N. L., Allan, J. D., Bain, M. B., Karr, J. R., Prestegaard, K. L., Richter, B. D., Stromberg, J. C. 1997. The Natural Flow Regime. BioScience, 47(11), 769-784. https://doi.org/10.2307/1313099

Puckridge, J. T., Sheldon, F., Walker, K. F., Boulton, A. J. 1998. Flow variability and the ecology of large rivers. Marine and Freshwater Research 49:55-72.

Rivenbark, B. L., Jackson, C. R. 2004. Concentrated flow breakthroughs moving through silvicultural streamside management zones: Southeastern Piedmont, USA. Journal of the American Water Resources Association 40:1043–1052.

Rocha, J., Duarte, A.; Silva, M., Fabres, S., Vasques, J., Revilla-Romero, B., Quintela, A. 2020. The Importance of High Resolution Digital Elevation Models for Improved Hydrological Simulations of a Mediterranean Forested Catchment. Remote Sens. 12, no. 20: 3287. https://doi.org/10.3390/rs12203287

Rykken, J. J., Moldenke, A. R., Olson, D. H. 2007. Headwater Riparian Forest-Floor Invertebrate Communities Associated with Alternative Forest Management Practices. Ecological Applications 17(4):1168-1183.

Sedell, J. R., Beschta, R. L. 1991. Bringing back the “bio” in bioengineering. American Fisheries Society Symposium 10:160–175.

Sharpley, A., Foy, B., Withers, P. 2000. Practical and innovative measures for the control of agricultural phosphorus losses to water: an overview. J. Environ.Qual. 29, 1–9.

Smart, R. P., Soulsby C, Cresser, M. S., Wade, A. J., Townend, J., Billett, M. F., Langan, S. 2001. Riparian zone influence on stream water chemistry at different spatial scales: a GIS-based modelling approach, an example for the Dee, NE Scotland. The Science of the Total Environment. 2001 Dec; 280(1-3):173-193. https://doi:10.1016/s0048-9697(01)00824-5

Sonneveld, M. P. W., Schoorl, J. M., Veldkamp, A. 2006. Mapping hydrological pathways of phosphorus transfer in apparently homogeneous landscapes using a high-resolution DEM. Geoderma 133, 32–42.

Sørensen, R., Zinko, U., Seibert, J. 2005. On the calculation of the topographic wetness index: evaluation of different methods based on field observations. Hydrology and Earth System Sciences Discussion 2, 1807–1834.

Sridhar, V., Sansone, A. L., LaMarche, J., Dubin, T., Lettenmaier, D. P. 2004. Prediction of stream temperature in forested watersheds. Journal of the american Water Resources association 40:197–213.

Steel, E. A., Naiman, R. J., West, S. D. 1999. Use of Woody Debris Piles by Birds and Small Mammals in a Riparian Corridor. Northwest Science 73(1):19-26.

Story, A. C., Moore, R. D., Macdonald, J. S. 2003. Stream temperatures in two shaded reaches below cut blocks and logging roads: downstream cooling linked to subsurface hydrology. Canadian Journal of Forest Research 33:1383–1396.

Swanson, F. J., Gregory, S. V., Sedell, J. R., Campbell, A. G. 1982. Land-water interactions: The riparian zone. Pages 267-291 in R. L. Edmonds, Ed. Analysis of Coniferous Forest Ecosystems in the Western United States. Hutchinson Ross: Stroudsburg, Pennsylvania.

Virgona J. M., Gummer F. A. J., Angus J. F. 2006. Effects of grazing on wheat growth, yield, development, water use, and nitrogen use. Australian Journal of Agricultural Research 57, 1307-1319. https://doi.org/10.1071/AR06085

Wilkerson, E., Hagan, J. M., Siegel, D., Whitman, A. 2006. The effectiveness of different buffer widths for protecting headwater stream temperature in Maine. Forest Science 52:221–231.

Wilson, A., Evans, T., Moore, W., Schutte, C., Joye, S., Hughes, A., Anderson, J. L. 2015. Groundwater controls ecological zonation of salt marsh macrophytes. Ecology. 96. 840-849. https://doi.org/10.1002/2014WR015984

Wipfli, M.S. 1997. Terrestrial invertebrates as salmonid prey and nitrogen sources in streams: Contrasting old-growth and young-growth riparian forests in southeastern Alaska, USA. Canadian Journal of Fisheries and aquatic sciences 54:1259–1269.

Xiang, H., Tian, L. 2011. Development of a low-cost agricultural remote sensing system based on an autonomous unmanned aerial vehicle (UAV). Biosystems Engineering, 108 (2), 174-190. https://doi.org/10.1016/j.biosystemseng.2010.11.010

CHAPTER 2: Optimal Parameters for Using Consumer-Grade Unmanned Aerial Vehicles to Produce High Resolution Digital Surface Model (DSM)

2. 1. Introduction

Agroforestry is the growing of trees and other perennial plants together with annual crops or livestock that optimizes the benefits from these biological interactions. It is a globally recommended land-use system where trees are integrated into agricultural ecosystems in order to achieve ecological, economic, and social benefits. It has been found that plant communities with higher diversity use resources more efficiently than monoculture communities (Binkley *et al*., 1992a; Liebman & Staver, 2001, Zuppinger-Dingley *et al*., 2014). Enhanced plant diversity increases the stability and resilience of the community and provides habitat connectivity for birds and mammals, which becomes critically important in fragmented ecotones (Kiær *et al*., 2009; Letourneau *et al*., 2011; Balvanera *et al*., 2014). Additionally, diversified ecosystems also provide other environmental services such as carbon sequestration and enhancement of water quality (McNeely & Schroth 2006; Udawatta *et al*., 2010).

One of the most important spatial characteristics used to assess forest ecosystems and resource inventories is canopy height. It is an ecological measure that provides essential information related to biophysical, hydrological, ecological, and agronomic processes in both natural vegetation and agricultural crops (Selkowitz *et al*., 2012). Crown diameter is often used to estimate individual tree characteristics, such as stem diameter and volume (Hyyppä *et al*., 2005). As the crown diameter is directly linked with amount of foliage, it

is also an indicator of tree competition and forest health. Stand management decisions, such as when and how much to thin a stand, rely heavily on data derived from measuring crown diameters. For instance, gaps in the canopy become critical for modeling plant regeneration on the forest floor (Shugart & West 1977; Gray & Spies 1996).

Unlike diameter at breast height (DBH), tree crown size becomes difficult to measure in the field. Due to the complexity of in-field tree measurements, crown size is often estimated indirectly using geometry and trigonometric equations (Avery & Burkhart, 1994; Bragg, 2008; Larjavaara & Muller-Landau, 2013). These indirect estimations can result in potential errors, often leading to overestimation of radiation and precipitation interception, carbon assimilation, and transpiration in the canopy (Landsberg & Waring, 1997; Song *et al*., 2009). The ability to quantify traits such as tree height and crown size through cost-efficient methods is urgently needed (Madec *et al*., 2017; Rallo *et al*., 2018).

Remote sensing technology is considered to be a promising alternative to field surveys for the estimation of tree and forest parameters. Light Detection and Ranging (LiDAR) is an accurate method to quantify forest aboveground biomass (AGB) at a landscape level (Chen, 2013; Lu *et al*., 2014). Furthermore, tree crown estimations from remote sensing can take into account tree irregularities ignored by the operator in field measurements (Moorthy *et al*., 2011). However, LiDAR exhibits some weaknesses that are difficult to overcome. For example, LiDAR does not include spectral information, and it becomes difficult to align LiDAR scans from both sides of the tree (Rosell *et al*., 2009). Additionally, the difficulty of using LiDAR to detect the exact tops of trees has also been reported (Yu *et al*., 2004; Chen *et al*., 2006; Luo *et al*., 2018). Previous studies reported

low accuracy in field measurements of the height due to umbrella-shaped tree crowns (i. e. *Pinus pinea* and *Pinus sylvestris*) which do not have a clear apical dominance (Guerra-Hernández *et al*., 2016).

In recent years, as a cost-effective alternative to Airborne Laser Scanning (ALS), unmanned aerial vehicles (UAVs) have been developed for surveying small areas, landscape feature identification, erosion studies, vegetation dynamics monitoring, and crop assessments (Küng *et al*., 2011; Restas, 2015; Manfreda *et al*., 2018; Shimura *et al*., 2018). New assessments of traditional Multi-View Stereo (MVS) photogrammetry has demonstrated comparable results and a significant reduction (~80%) in data collection requirements compared to older Structure from Motion (SfM) methods (James & Robson, 2014; Díaz-Varela *et al*., 2015; Torres-Sánchez *et al*., 2015, Mohan *et al*., 2017). Zarco-Tejada and others (2014) aimed to estimate the height of plantation olive trees using a UAV and they achieved acceptable accuracy for height measurements when generating the Digital Surface Model (DSM). Furthermore, they tested different resolutions (5, 20, 25, 30, 35, 40, and 50 cm pixel^{-1}) in order to optimize the software processing times. They found that 3D data point information extracted from DSM experienced a significant reduction in accuracy when the DSM was interpolated at a resolution below 35cm pixel^{-1}. Based on root mean square error (RMSE), errors in tree height estimation was below 15% when image resolution was 30 cm pixel^{-1}. Krause *et al*. (2019) validated the photogrammetric tree height measurements of all trees against the field-based measurements and observed a significantly low error (RMSE = 0.138 m, or 0.79%), with good repeatability.

Despite the recent technical advances in UAVs that have made them increasingly relevant tools for forest measurements, information on how to set optimal flight parameters, such as image overlap, pre-planned flight grid, flight height, and camera angle for image reconstruction and successful 3D point extraction have not been explored in detail yet (Pajares, 2016; Liu *et al*., 2018; Iglhaut *et al*., 2019; Seifert *et al*., 2019). This is due to the wide variety of types of platforms and equipped sensors that can be mounted on a UAV. The overall aim of this study is to provide the optimal parameters for consumer-grade camera (DJI Phantom 4 Pro) to survey farmland and agroforestry areas. An empirical study over farmland area was conducted to meet three main objectives: 1) Assess the influence of image overlap rate on measurement accuracy when generating 2D map and Digital Surface Model; 2) Test the impact of flight height on point cloud density; 3) Estimate the optimal oblique camera angle for estimating the height, surface area and volume of a human-made measurable object using photogrammetry.

2. 2. Materials and methods

2.2.1. Study area

The field test was done at the Fredericton Research and Development Center (FRDC) of Agriculture and Agri-food Canada (AAFC) in Fredericton, NB, Canada (Latitude: 45.923397 Longitude: −66.606842, 35m asl). The area is relatively flat with an elevation difference of less than 0.4 meters within an area of 1.6 ha. The test site was covered with short grass and does not have tall-obstacle landscape features. The testing objects were three cardboard boxes (Figure 2.1), with field-measured heights of 74, 37.4

and 35.2 cm (specific measures detailed in Table 2-1), and spatially distributed 1 meter apart from each other.

Figure 2.1. Cardboard boxes and UAV used in the Study site

Table 2–1. Measures of cardboard boxes used for the point cloud and DSM analysis (units expressed in cm.)

Feature	Colour	Height	Width	Length
Box 1	White	74	38.6	59.4
Box 2	Black	35.2	13.4	39.7
Box 3	White	37.4	17.6	53.4

2.2.2. Unmanned Aerial Vehicle and camera

The unmanned aerial vehicle used was a DJI Phantom 4 Pro (Da-Jiang Innovations, SZ DJI Technology Co., LTD). This UAV model was considered to be most versatile consumer-grade UAV in terms of dimensions, weight, flight time, and ground sample distance delivered in 2D maps (Rogers *et al*., 2020). This UAV is a vertical takeoff and landing aircraft with total payload of 1388 g (battery and propellers included). This UAV uses 4 x 2312S Brushless motors powered by a 15.2 V battery, with vertical takeoff and landing. It can reach a cruising speed of 72.0 km h^{-1} (s-mode) and a maximum climb speed

of 6 m s^{-1}. The maximum wind speed resistance is up to 10.0 m s^{-1}, with multiple satellite position navigation system (GPS & GLONASS). The maximum flight time for a single battery is 30 minutes and the UAV required a maximum flight time of up to 7 minutes for higher image overlaps, and a maximum of 3 minutes for lower image overlaps.

The onboard camera is 1" complementary metal oxide semiconductor (CMOS) with 20M effective pixels (5472 x 3648). The lenses have a field of view (FOV) of 84°, with a focal length of 8.8 mm/24 mm (35 mm format equivalent) f/2.8 - f/11, and auto focus at 1 m - ∞. During the flight, the sensor registers either vertical images captured at Nadir angle (for 2D maps), or the camera can be tilted (off-Nadir angles), for the 3D Digital Surface Model (DSM). The image trigger can be activated automatically in autopilot flight mode, with simultaneous timestamps. It records the GPS location for each image, and automatically stores the image together with its metadata on an on-board Secure Digital Card (SD-Card).

2.2.3. Data acquisition for the Digital Surface Model

The test was performed on November the 17th of 2018. The weather during the testing period was partially cloudy, with calm winds less 10 km h^{-1}. We collected 20 GPS waypoints for georeferencing purposes with a Trimble Geoexplorer 6000 Series handheld GPS (10 cm accuracy). The flight heights tested were 70 and 30 meters. These heights were chosen based on the tree height in the targeted UAV application area where the maximum height of coniferous plantation of red pine (*Pinus resinosa*) and Jack pine (*Pinus banksiana*) was 25 meters. The camera angles tested were 10, 20 and 30 degrees off-Nadir and the overlapping rates tested were 90, 80, 60 and 45% at 70 meters elevation using the

same grid size in all configurations. In addition, we acquired images at a flight height of 30 meters at Nadir and 20 degrees off-Nadir and 80% image overlap with parallel and perpendicular flight grid lines to test the impact of flight height in point cloud density.

2.2.4. Data processing

The data was processed with Pix4D software (Pix4D Inc) on a Dell Precision 5810 (Intel ® Xeon ® CPU ES-1620 v3 @ 3.50GHZ, 72.0GB RAM, Radeon T(M) Pro WX 5100 graphic card). The coordinate system used was World Geodetic System (WGS) 84 / UTM zone 19. Processing options were 3D maps, keypoints image scale full, orthomosaic as a GEO Tiff with no correction type, half image scale, high point density, with minimum number of matches as 3.

The point clouds obtained with Pix4D were interpolated with LAStools commercial software suite (Martin Isenburg, LAStools -efficient tools for LiDAR processing) to generate the DSM and deliver 1.8cm cell size. This resolution was higher than previously reported by Haval (2019) and Rogers *et al*., (2020).

2.2.5. Height, area and volume estimations

The average of ten height values on the top surface of the box, represented on interpolated DSM, was used as the predicted value for height of the box. The height values near the box edge were not considered, as we observed slight elevation errors produced by the sharp edges of the box. Similarly, area was estimated based only on entire top surface and minor edge inaccuracies represented in DSM were excluded. Finally, the volumes were calculated by the estimated area multiplied by the box height.

2.2.6. Accuracy Assessment

We calculated the bias (B_i) of each variable (height, area and volume) using the error, where *Oi* is the observed value, *Pi* predicted value and *n* is the number of observations:

$$B_i = \sum_{i=1}^{n} \left(\frac{Oi - Pi}{n}\right)$$

Additionally, the percentage of bias was calculated using:

$$\% B_i = \sum_{i=1}^{n} \left(\frac{Pi - Oi)}{Oi}\right) * 100$$

2. 3. Results and discussion

2.3.1. Camera tilt angle, area covered and 2D map resolution

Processing time, re-projection error, ground sample distance (GSD), and total mapped area with different camera angles and overlapping rates are shown in Table 2-2. We found the data processing time increased exponentially with overlapping rate (Figure 2.2). These results agree with our expectations because the number of images set to be processed increased with overlapping rate. We found that higher Nadir angles provided higher resolution whereas more oblique angles (30 degrees off-Nadir) increased the pixel size. For example, when off-Nadir angle was 10 degrees, pixel resolution was 1.80 cm for all image overlaps tested with this camera angle. However, with the camera tilted at 30 degrees off-Nadir, the pixel size was 2.10. Unlike vertical images (Nadir angle) that have a uniform scale over the entire image, images obtained with oblique angle showed a trapezoidal footprint, no uniform scale and increased distortion that may need to be corrected by image processing software (Verykokou & Ioannidis, 2015; Lingua, 2017; Haval, 2019). Overall,

our findings are in support of what was reported by Liu (2018), where more vertical angles decreased distortion and gaps observed at the boundaries of the mapped areas.

Results indicated that higher image overlap covered a larger area, if we compare the same camera angle. For instance, at 10 degree off-Nadir the area covered was 2.09 ha when image overlap was 90% and was reduced to 1.25 ha when overlap was 45%. At a given overlap rate, the tilt of camera angle to a more oblique angle increased the mapped area. For example, a 90% overlap included an area of 2.09 ha at 10 degrees off-Nadir angle, compared to 5.35 ha when 30 degrees off-Nadir angle was used. We also observed that increasing the image overlap from 80 to 90% did not cover a significantly larger area.

The number of 3D points per bundle adjustment refers to the number of 3D points that the software uses to adjust camera parameters to reconstruct a 3D image using triangulation. We found that the number of 3D points per bundle block adjustment increased with overlap rate at the same camera angle. These results agreed with our expectations because higher overlap rates also indicate more images collected over the same area. A fact worth mentioning is the point cloud software post-processing time based on image overlap. When the image overlap was changed from 45% to 80%, the software post-processing time required to generate the point cloud increased progressively. However, when image overlap was changed from 80 to 90%, the post-processing time soared by nearly five times, in all angles tested. Additionally, the number of 3D points for bundle block adjustment rose by 200%.

Table 2–2. Processing time, ground sample distance (GSD) and total mapped area with different camera angles and overlap rates. Flight height was 70 meters.

Tilt angle (Degrees)	Image Overlap %	Average GSD (cm/pixel)	Point Cloud Processing Time (minutes)	3D Points for Bundle Block Adjustment	Area Covered (ha)
10	90	1.80	117.0	629,395	2.09
	80	1.80	22.0	294,640	1.94
	60	1.80	6.0	136,254	1.63
	45	1.80	3.0	82,960	1.25
20	90	1.92	99.0	659,333	3.14
	80	1.92	21.0	295,380	2.86
	60	1.92	6.0	109,642	2.08
	45	1.92	2.7	72,729	1.70
30	90	2.10	105.0	688,360	5.35
	80	2.10	20.0	286,003	4.92
	60	2.10	5.7	93,673	2.92
	45	2.10	1.7	58,849	2.78

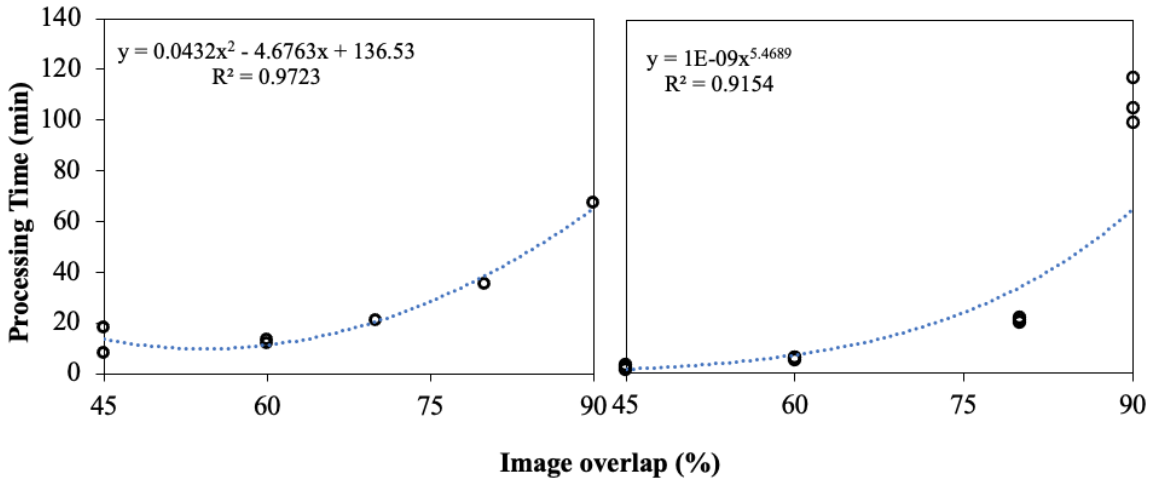

Figure 2.2. Data processing times for 2D maps (left) and the point cloud generation (right), at different image overlaps.

2.3.2. Point cloud density

Point cloud densities obtained with different flight altitudes, camera angles, overlap rates, and flight path grids are shown in Table 2-3. As expected, lower flight altitudes generated denser point clouds. With the same single flight path grid and Nadir angle, the point cloud density was 1094 per m^2 for flights at 70 meters altitude, compared with 5462 per m^2 at 30 meters, which represents an increase of five times. With the same altitude, a higher overlap rate would generate higher point cloud density; the relationship between point cloud density and overlap rate can be described as logarithmic lines (Figure 2.3). Using a 70 meter altitude as an example, when the overlap rate increased from 45% to 90%, the point cloud density increased from 522 to 2105 points per m^2, which represents an increase of 400%. Also, when the flight path was changed from single- to double-parallel grids (perpendicular to each other), the point cloud density also doubled, from 5462 to 10560 points per m^2. Results indicated that both lower flight altitude and double flight path grid can experience an increase in point cloud density. However, flights at low altitude and double grid path would increase the number of images and would require a longer time to collect and process images.

Table 2–3. Point cloud density under different flight altitude, overlap rates, flight path grids and camera angles. "Single" grid refers to pre-planned flight path using only parallel lines and "Double" refers to two set of parallel flight path perpendicular to each other.

Flight height (m)	**Image Overlap (%)**	**Grid / Camera angle (Degrees)**	**Pulses per m^2 (average)**
70	**60**	Single / Nadir	756
80	80	Single / Nadir	833
30	80	Single / Nadir	**5,462**
70	80	Single / Nadir	**1,094**
70	90	Double / 30	2,105
70	80	Double / 30	1,118
70	60	Double / 30	871
70	45	Double / 30	522
70	90	Double / 20	2,537
70	80	Double / 20	1,488
70	60	Double / 20	920
70	45	Double / 20	760
70	90	Double / 10	2,663
70	80	Double / 10	1,465
70	60	Double / 10	968
70	45	Double / 10	891
30	80	Double / 20	**10,560**
LiDAR	-	-	8.12

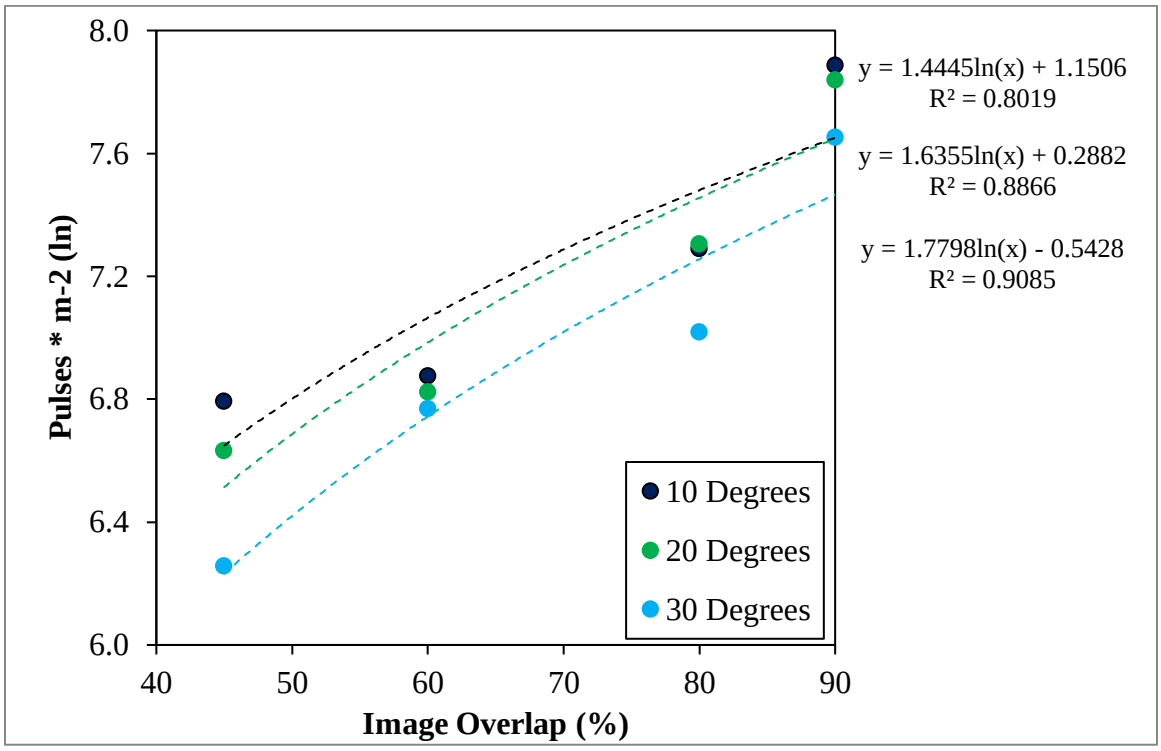

Figure 2.3. Point cloud density at different overlap rates and camera angles. From top to bottom, equations corresponding to 10 degrees, 20 degrees, and 30 degrees off-Nadir, respectively.

We observed that camera angles also have significant impacts on resulting point cloud densities, especially when the angle changes from 20 to 30 degrees (Figure 2.3). For example, at 70 meter altitude and double grid flight path, the point cloud density was 2663 at 10 degrees off-nadir, compared with 2105 at a 30 degree angle.

However, at lower overlap rates, the impacts of camera angles were more discrete. For example, when the overlap rate was 45%, the point cloud density was 891 at 10 degrees off-nadir, compared with 522 points per m^2 at a 30 degree angle.

2.3.3. Height, area, and volume estimations

Estimated height, area, and volume compared with the measured values for three cardboard boxes are shown in Figure 2.4. Generally, we found overlap percentages around 80% performed the best for camera angle of 10 degree and 20 degrees for all variables measured. In regards to height, when the overlapping rate increased from 80% overlap to 90%, R^2 decreased slightly. Similarly, we observed a modest reduction from an R^2 of 0.995 to 0.988 when the overlap rate increased from 80 to 90%, when the 20 degrees was used. When 30 degrees was used the R^2 was highest at 0.994 with 45% overlap. Conversely, R^2 resulted of 0.930 and 0.985 at 80 and 90% overlapping rate.

The relative bias of height estimation ranged from -20% to -5%, corresponding to an error ranging from 1 to 16 cm in height (Table 2-4). As can be seen, the error (bias) was lower when 60% overlap was used. In our predictions, height was underestimated in most of the results obtained (Figure 2.4). These results are in agreement with previous studies reported by Krause et al. (2019) and Rogers *et al*. (2020), and they also found that the photogrammetric method tended to slightly underestimate tree heights.

The estimated point heights for each image overlap tested expressed as increasing distance with respect to the point of the center (of box number 1) are shown in figures 2.5 and 2.6 (only for 10 degrees). Overlap rates of 90 and 80% tended to concentrate the points at the same height level, reducing the dispersion, whereas 45 and 60%, particularly, resulted in a rise in point dispersion. These errors were likely due to lower number of images collected at 45% and 60% overlap.

Additionally, figure 2.5 shows the distortion of the shape of the box. Points representing the sides of the box, at a lower height than surface, where captured at a

distance of nearly 20 cm from the center (actual width of the box was 38.6cm) for image overlaps of 90, 80, and 60%. However, when a 45% overlap rate was used, these points were also detected at a closer distance to the center, indicating a remarkable distortion of the shape represented in the DSM. These results agree with previous expectation because a higher number of images provided higher detail to represent the shape of an object in a DSM.

The standard deviation of height measurement changes with increasing distance from the box center is shown in Figure 2.7. We found that height measurement close to the box center had less bias and less variation, while these points close to the edge would have larger errors, and larger variation. The high variation and errors at points close to surface edges were likely caused by interpolation errors.

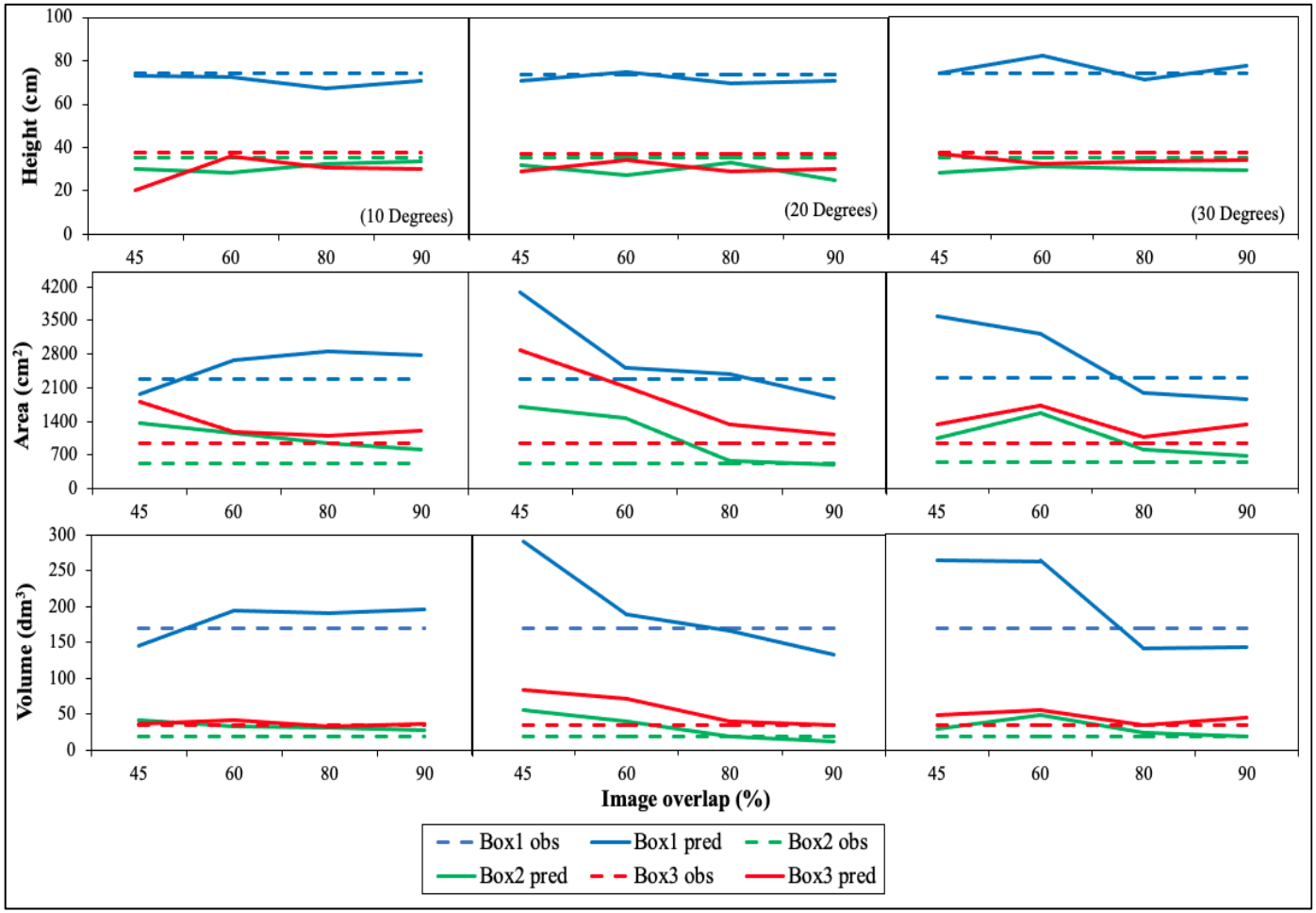

Figure 2.4. Estimation of height, area and volume using 3 different camera angles; from left to right: 10, 20 and 30 degrees off-Nadir; (obs= observed value and pred=predicted value).

Table 2–4. Percentage bias, R^2, and slope of regression line of estimated vs measured heights, areas and volumes under different overlap rates, and camera angles off-Nadir.

	Camera Angle	**10 Degrees**			**20 Degrees**			**30 Degrees**		
	Overlap (%)	**R^2**	**Slope**	**Bias (%)**	**R^2**	**Slope**	**Bias (%)**	**R^2**	**Slope**	**Bias (%)**
Height	90	0.996	0.931	-10	0.998	0.984	-18	0.992	0.985	-8
	80	0.998	0.893	-12	0.995	0.915	-11	0.997	0.930	-10
	60	**0.996**	**0.951**	**-8**	**0.991**	**0.958**	**-10**	**0.988**	**1.030**	**-5**
	45	0.968	0.890	-20	0.995	0.920	-12	0.994	0.967	-7
Area	90	0.997	1.233	34	**0.979**	**0.876**	**-2**	0.945	0.907	15
	80	0.991	1.255	40	0.985	1.094	18	0.974	0.927	16
	60	0.972	1.233	53	0.876	1.332	104	0.952	1.529	106
	45	0.833	1.085	79	0.940	2.019	168	0.996	1.553	64
Volume	90	0.999	1.157	21	0.998	0.791	-20	0.990	0.857	5
	80	0.996	1.123	25	**0.999**	**0.987**	**3**	**0.995**	**0.840**	**3**
	60	0.997	1.153	37	0.968	1.164	76	0.995	1.564	91
	45	0.972	0.875	37	0.989	1.748	133	1.000	1.549	50

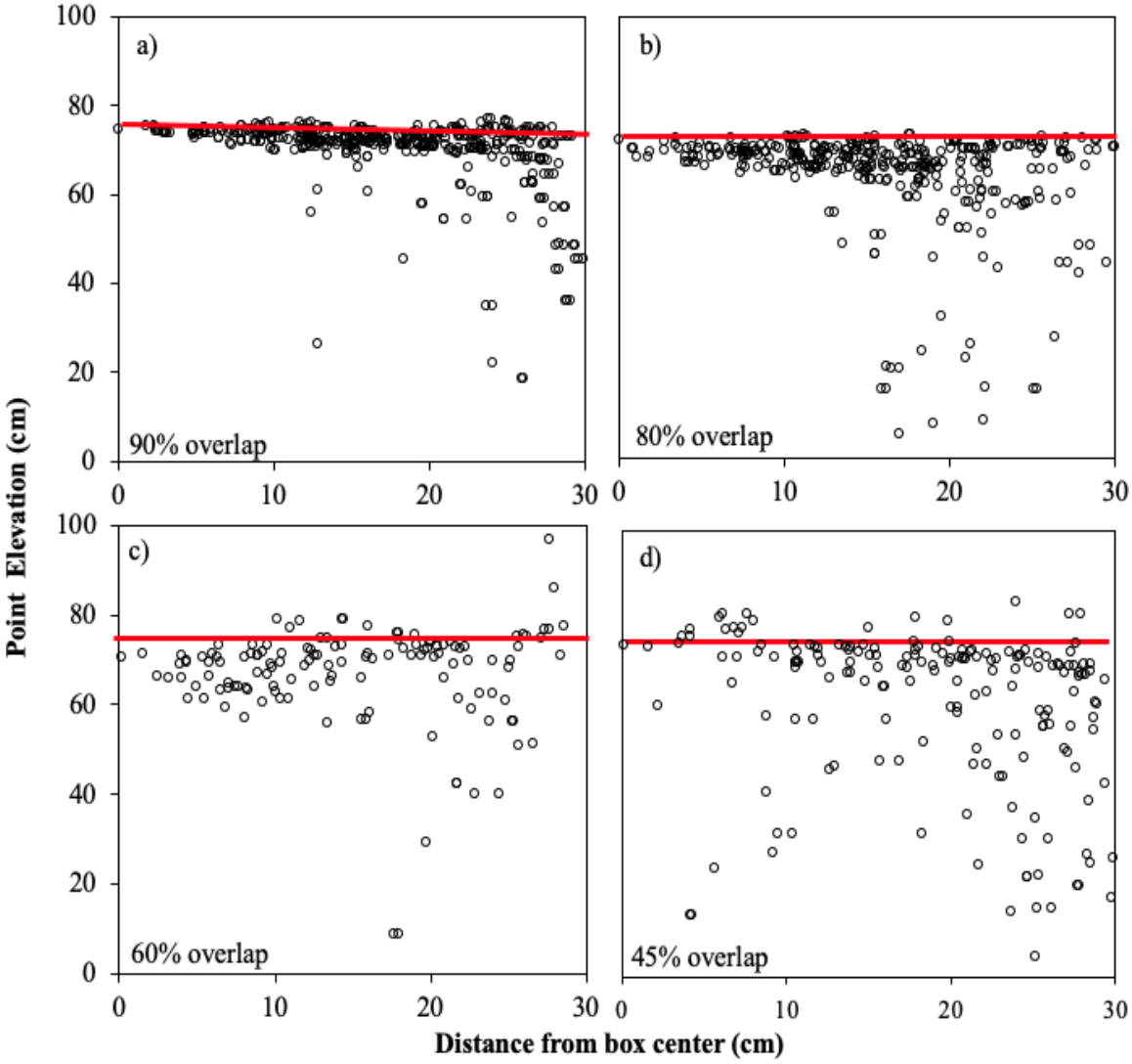

Figure 2.5. Point cloud distribution of box 1 extracted from DSM at 10 degrees off-Nadir. In red, the actual height of box 1 (74cm). Image overlaps: a) 90%, b) 80%, c) 60% and d) 45%. As can be seen, there is more dispersion of the points in 60 and 45% overlaps, whereas 80 and 90% overlap rates tended to reduce dispersion.

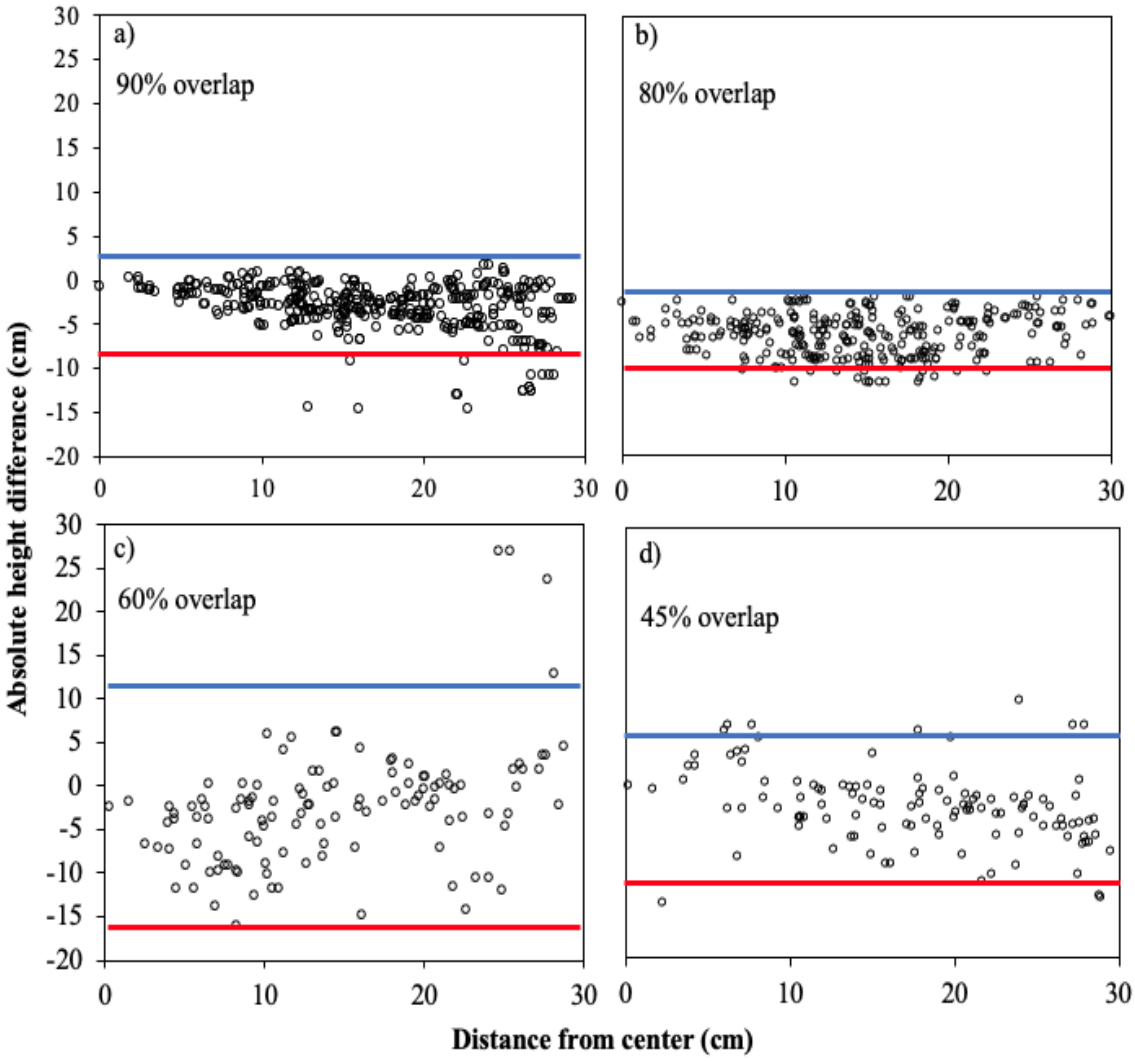

Figure 2.6. Panels representing point elevation difference across the surface of the box compared with the actual height of box number 1 (at 0 cm). Values were extracted from images obtained at 10 degrees off-Nadir at different overlaps: a) 90%, b) 80%, c) 60% and d) 45% overlap. Red and blue lines represent confidence intervals at 95%.

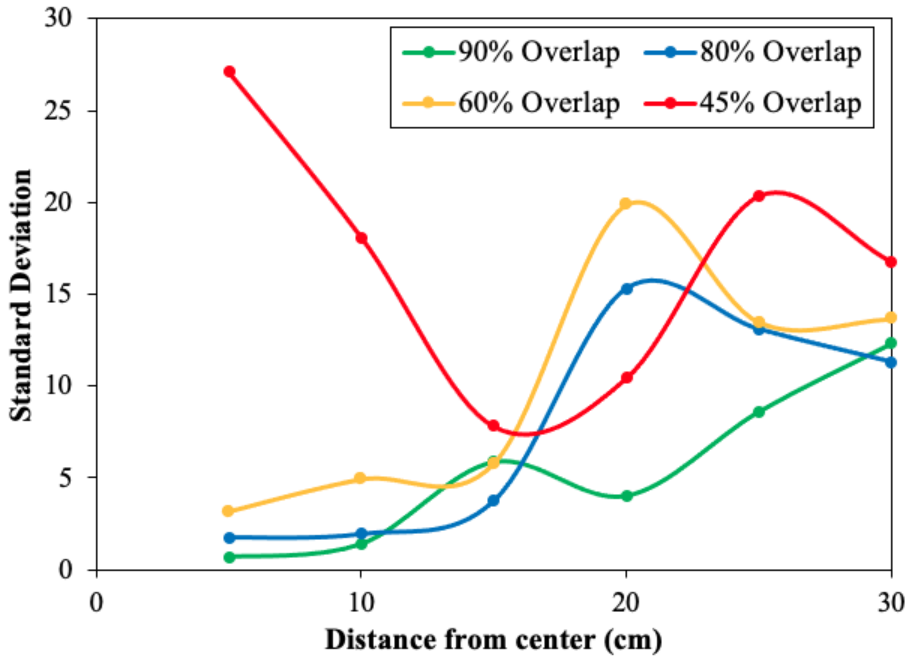

Figure 2.7. Standard deviation of the height values obtained from the point cloud dataset generated from 10 degrees off-Nadir at all overlap rates tested (90, 80, 60 and 45%). It is expressed as a variation function of the distance from the box center representing the values of box number 1. As can be seen, 90% overlap tended to maintain elevation values across the surface more uniformly.

The surface area represented in DSM was overestimated in practically all tests done. When 10 degrees was used, the R^2 experienced a significant decrease as the image overlap was reduced. For example, in 90% overlap rate, the R^2 was of 0.997 and resulted of 0.833 when the overlap rate was 45%. On the other hand, when the camera angle was 20 degrees, the R^2 ranged from 0.985, when the image overlap was 80%, to 0.876 when the image overlap used was 60%. An interesting result was found when 30 degrees was used; the R^2 was 0.996 when the image overlap was 45%, and decreased to 0.945 when 90% overlap rate was used.

When the camera angle of 10 degrees was used, the bias experienced an increase when image overlap was reduced. For instance, when the highest overlap was used (90%), the bias was 34%, indicating relatively fair agreement. However, the bias was 73% when the

image overlap was low (45%), indicating poor agreement. The same trend was observed when the camera angle was set at 20 degrees off-Nadir. The biggest error was registered when the image overlap was 45%, with a bias of 168%. Finally, when the 30 degree was used, the bias resulted of 106% with an image overlap of 60%. These results agree with our expectations, because DSMs represented objects in better detail when higher image overlaps were used, which provided more accurate area estimations.

The volume followed a similar trend observed with the results obtained for the area estimations. When 10 degrees was used, the R^2 was 0.999 with an image overlap of 90% and 0.972 when image overlap of 45%. When the angle used was 20 degrees, R^2 ranged from 0.999 at 80% image overlap to 0.968 at 60% image overlap. Interestingly, at 30 degree R^2 decreased from 1.000 when image overlap was 45% to 0.990 when the highest image overlap (90%) was used.

At 10 degrees, the bias followed an increasing trend as the image overlap was reduced. The bias ranged from 21% to 37% with image overlaps of 90 and 45%, respectively. However, the widest range of bias was found at 20 degrees; when the image overlap was 80% the bias resulted of 3%. Conversely, the biggest error (bias 133%) was found when 45% image overlap was used. Finally, when the camera was tilted to 30 degrees, the lowest error was found when 80% image overlap was used. However, the bias increased to 91% when 60% image overlap was used. The volume seemed to be best estimated with 20 and 30 degrees with 80% image overlap. These results agree with previous expectations because a higher number of images would provide better detail to represent objects in a DSM.

In the analysis of the variables estimated with DSM interpolation (the height, the area, and the volume) we aimed to contrast the difference in precision between data acquired at high and low image overlap coupled with different camera angles. However, more data needs to be acquired to obtain more definite results and provide more evidence of whether the camera angle has an influence on the variables measured.

References

Avery, T. E. Burkhart, H. E. 1994. Forest Measurements 4th Ed. McGraw- Hill, Inc, New York, NY. 408 p.

Balvanera, P., Siddique, I., Dee, L., Paquette, A., Isbell, F., Gonzalez, A., Byrnes, J., O'Connor, M. I., Hungate, B. A., Griffin, J. N. 2014. Linking biodiversity and ecosystem services: current uncertainties and the necessary next steps. BioScience, 64, 49–57.

Binkley, D., Dunkin, K. A., DeBell, D. S., Ryan, M. G. 1992a. Production and nutrient cycling in mixed plantations of Eucalyptus and Albizia in Hawaii. *For. Sci.* 38:393–408.

Bragg, Don. 2008. An Improved Tree Height Measurement Technique Tested on Mature Southern Pines. Southern Journal of Applied Forestry. 32. 38-43. 10.1093/sjaf/32.1.38.

Chen, Q., Baldocchi, D., Gong, P., Kelly, M. 2006. Isolating individual trees in a Savanna woodland using small footprint LiDAR data. Photogrammetric Engineering & Remote Sensing. Vol. 72:8. p. 923-932. ISSN 0099-1112.

Díaz-Varela, R. A., de la Rosa, R., León, L., Zarco-Tejada, P. J. 2015. High-resolution airborne UAV imagery to assess olive tree crown parameters using 3D photo reconstruction: application in breeding trials. Remote Sens. 7, 4213–4232. 10.3390/rs70404213

Gray, A. N., Spies, T. A. 1996. Gap size, within-gap position and canopy structure effects on conifer seedling establishment. J. Ecol. 84, 635–645.

Guerra-Hernández, J., González-Ferreiro, E., Sarmento, A., Silva, J., Nunes, A., Correia, A.C., Fontes, L., Tomé, M., Díaz-Varela, R. 2016. Using high resolution UAV

imagery to estimate tree variables in Pinus pinea plantation in Portugal. Forest Systems, Volume 25, Issue 2, eSC09.

Haval, A. S. 2019. Accuracy assessment using different UAV image overlaps. Journal of Unmanned Vehicle Systems. 7(3): 175-193. https://doi.org/10.1139/juvs-2018-0014

He, Q., Chen, E., An, R., Li, Y. 2013. Above-ground biomass and biomass components estimation using LiDAR data in a coniferous forest. Forests 4(4), 984–1002.

Hyyppä, J., Mielonen, T., Hyyppä, H., Maltamo, M., Yu, X., Honkavaara, E., Kaartinen, H. 2005. Using individual tree crown approach for forest volume extraction with aerial images and laser point clouds. Int.Arch. Photogramm. Remote Sens. Spat. Inf. Sci., *36*, W19.

Iglhaut, J., Cabo, C., Puliti, S., Piermattei, L., O'Connor, J., Rosette, J. 2019. Structure from Motion Photogrammetry in Forestry: a Review. Curr Forestry Rep 5**,** 155–168. https://doi.org/10.1007/s40725-019-00094-3

James, M. R., Robson, S. 2014. Mitigating systematic error in topographic models derived from UAV and ground-based image networks. Earth Surface Processes and Landforms, 39(10), 1413–1420. 10.1002/esp.3609.

Kiær, L. P., Skovgaard, I. M., Østergård, H. 2009. Grain yield increase in cereal variety mixtures: a meta-analysis of field trials. Field Crops Research, 114, 361–373.

Krause, S., Sanders, T.G., Mund, J.-P., Greve, K. 2019. UAV-Based Photogrammetric Tree Height Measurement for Intensive Forest Monitoring. Remote Sens. 11, 758.

Küng, O., Strecha, C., Beyeler, A., Zufferey, J.-C., Floreano, D., Fua, P., Gervaix, F. 2011. The accuracy of automatic photogrammetric techniques on ultra-light UAV imagery. In Proceedings of the UAV-g 2011-Unmanned Aerial Vehicle in Geomatics, Zürich, Switzerland, 14–16 September.

Landsberg, J. J., Waring, R. H. 1997. A generalized model of forest productivity using simplified concepts of radiation-use efficiency, carbon balance and partitioning, For. Ecol. Manage., 95, 209–228, https://doi:10.1016/S0378-1127(97)00026-1

Larjavaara M., Muller-Landau, H. C. 2013. Measuring tree height: a quantitative comparison of two common field methods in a moist tropical forest. Methods Ecol. Evol. 4(9): 793–801.

Letourneau, D. K., Armbrecht, I., Rivera, B. S. 2011. Does plant diversity benefit agroecosystems? A synthetic review. Ecological Applications, 21, 9–21.

Liebman, M., Staver, C.P. 2001. Crop diversification for weed management. Ecological Managment of Agricultural Weeds (eds M. Liebman, C.L. Mohler & C.P. Staver), pp. 322–374. Cambridge University Press, Cambridge, UK.

Lingua, A., Noardo, F., Spanò, A., Sanna, S., Matrone, F. 2017. 3D Model generation using oblique images acquired by UAV. Int. Arch. Photogramm. Remote Sens. Spatial Inf. Sci., XLII-4/W2, 107–115, https://doi.org/10.5194/isprs-archives-XLII-4-W2-107-2017

Liu, J., Skidmore, A. K., Jones, S. D., Wang, T., Heurich, M., Zhu, X., Shi, Y. 2018. Large off-nadir scan angle of airborne LiDAR can severely affect the estimates of forest structure metrics. ISPRS journal of photogrammetry and remote sensing, 136, 13-25. https://doi.org/10.1016/j.isprsjprs.2017.12.004

Lu, D., Chen, Q., Wang, G., Liu, L., Li, G., Moran, E. 2014.A survey of remote sensing-based aboveground biomass estimation methods in forest ecosystems. Int. J. Digit. Earth 9 63–105.

Luo L., Zhai Q., Su Y., Ma Q., Kelly M., Guo, Q. 2018. Simple method for direct crown base height estimation of individual conifer trees using airborne LiDAR data. Optics Express 26, A562–A578. 10.1364/OE.26.00A562.

Madec, S., Baret, F., de Solan, B., Thomas, S., Dutartre, D., Jezequel, S., Hemmerlé, M., Colombeau, G., Comar, A. 2017. High-Throughput Phenotyping of Plant Height: Comparing Unmanned Aerial Vehicles and Ground LiDAR Estimates. *Front. Plant Sci.* 8, 2002. https://doi: 10.3389/fpls.2017.02002

Manfreda, S., McCabe, M., Miller, P., Lucas, R., Pajuelo Madrigal, V., Mallinis, G., Ben Dor, E., Helman, D.; Estes, L., Ciraolo, G., Müllerová, E., Tauro, F., De Lima, M. I., De Lima, J. L. M. P., Maltese, A., Frances, F., Caylor, K., Kohv, M., Perks, M., Ruiz-Perez, G., Su, Z., Vico, G., Toth, B. 2018. On the use of unmanned aerial systems for environmental monitoring. Remote Sens., 10, 641.

McNeely, J.A., Schroth, G. 2006. Agroforestry and Biodiversity Conservation – Traditional Practices, Present Dynamics, and Lessons for the Future. Biodivers Conserv 15, 549–554, https://doi:10.1007/s10531-005-2087-3

Mohan, M. M., Silva, C. A., Klauberg, C., Jat, P., Catts, G. P., Cardil, A., Hudak, A. T., Dia, M. 2017. Individual Tree Detection from Unmanned Aerial Vehicle (UAV) Derived Canopy Height Model in an Open Canopy Mixed Conifer Forest. Forests. 8. 10.3390/f8090340.

Moorthy, I, Miller, J. R., Jimenez, J. A., Zarco-Tejada, P. J., Hu, B., Chen, J. M. 2011. Field characterization of olive (Olea europaea L.) tree crown architecture using terrestrial laser scanning data. Agricultural and Forest Meteorology. 151. 204-214. 10.1016/j.agrformet.2010.10.005.

Nair, P., Nair, V., Gama-Rodrigues. 2009. Soil Carbon in Agroforestry Systems: An Unexplored Treasure?. Nat Prec, https://doi:10.1038/npre.2009.4061.1

Pajares, G. 2015. Overview and current status of remote sensing applications based on unmanned aerial vehicles (UAVs) Photogramm. Eng. Remote Sens. 2015;81:281–329. https://doi:10.14358/PERS.81.4.281

Rallo, L., Barranco, D., Díez, C. M., Rallo, P., Suárez, M. P., Trapero, C., Pliego-Alfaro, F. 2018. Strategies for olive (*Olea europaea* L.) breeding: cultivated genetic resources and crossbreeding; In Advances in Plant Breeding Strategies: Fruits (New York City, USA: Springer International Publishing).

Restas, A. 2015. Thematic Division and Tactical Analysis of the UAS Application Supporting Forest fire Management. In: Viegas, X.D., Ed., Advances in Forest Fire Research, Coimbra, Portugal. http://dx.doi.org/10.14195/978-989-26-0884-6_172

Rogers, S., Manning, I., Livingstone, B. 2020. Comparing the Spatial Accuracy of Digital Surface Models from Four Unoccupied Aerial Systems: Photogrammetry Versus LiDAR. Remote Sensing. 12. 2806. 10.3390/rs12172806.

Rosell, J. R., Llorens, J., Sanz, R., Arno, J., Ribes-Dasi, M., Masip, J., Palacín, J. 2009. Obtaining the three-dimensional structure of tree orchards from remote 2D terrestrial LIDAR scanning. Agricultural and Forest Meteorology, 149(9), 1505–1515.

Running, S. W., Justice, C. O., Salomonson, V., Hall, D., Barker, J., Kaufmann, Y. J., Strahler, A. H. 1994. Terrestrial Remote Sensing Science and Algorithms Planned for EOS/MODIS. International Journal Remote Sens 15 (17): 3587–3620. https://doi:10.1080/01431169408954346

Seifert, E., Seifert, S., Vogt, H., Drew, D., van Aardt, J., Kunneke, A., Seifert, T. 2019. Influence of Drone Altitude, Image Overlap, and Optical Sensor Resolution on Multi-View Reconstruction of Forest Images. Remote Sens. 11, 1252.

Selkowitz, D.J., Green, G., Peterson, B., Wylie, B., 2012. A multi sensor LIDAR, multi-spectral and multi-angular approach for mapping canopy height in boreal forest regions. Remote Sensing of Environment 121 (1), 458–471.

Shimura, T., Inoue, M., Tsujimoto, H., Sasaki, K., Iguchi, M. 2018. Estimation of Wind Vector Profile Using a Hexarotor Unmanned Aerial Vehicle and Its Application to Meteorological Observation up to 1000 m above Surface. J. Atmos. Oceanic Technol., 35, 1621–1631, https://doi.org/10.1175/JTECH-D-17-0186.1

Shugart, H. H., West, D. C. 1977. Development of an Appalachian deciduous forest succession model and its application to assessment of the impact of the chestnut blight. Journal of Environmental Management, 5, 161−179.

Song, C., Katul, G., Oren, R., Band, L. E., Tague, C. L., Stoy, P. C., McCarthy, H. R. 2009. Energy, water and carbon fluxes in a loblolly pine stand: Results from uniform and gappy canopy models with comparisons to eddy flux data. Journal of Geophysical Research- Biogeosciences, 114, G04021. https://doi.org/10.1029/2009JG000951

Torres-Sánchez, J., López-Granados, F., Borra-Serrano, I., Peña, J. M. 2018a. Assessing UAV-collected image overlap influence on computation time and digital surface model accuracy in olive orchards. Precis. Agric. 19, 115–133. https://doi.org/10.1007/s11119-017-9502-0

Udawatta, R. P, Garrett, H. E, Kallenbach, R. L. 2010. Agroforestry and grass buffer effects on water quality in grazed pastures. Agroforestry systems, *79*, 81-87, https://doi.org/10.1007/s10457-010-9288-9

Vacca, G., Dessi, A., Sacco, A. 2017. The Use of Nadir and Oblique UAV Images for Building Knowledge. ISPRS Int. J. Geo-Inf. 2017, 6(12), 393; https://doi.org/10.3390/ijgi6120393

Verykokou, S., Ioannidis, C. 2015. Metric exploitation of a single low oblique aerial image. In FIG Working Week 2015: From the Wisdom of the Ages to the Challenges of the Modern World, May 17-21, Sofia, Bulgaria.

Yu, X., Hyyppä, J., Hyyppä, H., Maltamo, M. 2004. Effects of flight altitude on tree height estimation using airborne laser scanning. International Archives Of Photogrammetry Remote Sensing And Spatial Information Sciences, XXXVI(8-W2), 96–101.

Zarco-Tejada, P., Díaz-Varela, R., Angileri, V. Loudjani, P. 2014. Tree height quantification using very high resolution imagery acquired from an unmanned aerial vehicle (UAV) and automatic 3D photo-reconstruction methods. European Journal of Agronomy. 55. 89–99. https://doi.org/10.1016/j.eja.2014.01.004

Zuppinger-Dingley, D., Schmid, B., Petermann, J., Yadav, V., De Deyn, G. B., Flynn, D. F. B. 2014. Selection for niche differentiation in plant communities increases biodiversity effects. Nature 515, 108–111, https://doi:10.1038/nature13869

CHAPTER 3: Using Unmanned Aerial Vehicle and LiDAR-derived DEMs to Estimate Channels of Small Tributary Streams

Abstract: Defining stream channels in a watershed is important for assessing freshwater habitat availability, complexity, and quality. However, mapping channels of small tributary streams becomes challenging due to frequent channel change and dense vegetation coverage. In this study, we used an Unmanned Aerial Vehicle (UAV) and photogrammetry method to obtain a 3D Digital Surface Model (DSM) to estimate the total in-stream channel and channel width within grazed riparian pastures. We used two methods to predict the stream channel boundary: the Slope Gradient (SG) and Vertical Slope Position (VSP). As a comparison, the same methods were also applied using low-resolution DEM, obtained with traditional photogrammetry (coarse resolution) and two more LiDAR-derived DEMs with different resolution. When using the SG method, the higher-resolution, UAV-derived DEM provided the best agreement with the field-validated area followed by the high-resolution LiDAR DEM, with Mean Squared Errors (MSE) of 1.81 m and 1.91 m, respectively. The LiDAR DEM collected at low resolution was able to predict the stream channel with a MSE of 3.33 m. Finally, the coarse DEM did not perform accurately and the MSE obtained was 26.76 m. On the other hand, when the VSP method was used we found that low-resolution LiDAR DEM performed the best followed by high-resolution LiDAR, with MSE values of 9.70 and 11.45 m, respectively. The MSE for the UAV-derived DEM was 15.12 m and for the coarse DEM was 20.78 m. We found that the UAV-derived DEM could be used to identify steep bank which could be used for mapping the hydrogeomorphology of lower order streams. Therefore, UAVs could be applied to efficiently map small stream channels in order to monitor the dynamic changes occurring

in these ecosystems at a local scale. However, the VSP method should be used to map stream channels in small watersheds when high resolution DEM data is not available.

Keywords: DEM; LiDAR; UAV; Stream bank; VSP; Slope Gradient.

Grau, J.; Liang, K.; Ogilvie, J.; Arp, P.; Li, S.; Robertson, B.; Meng, F.-R. Using Unmanned Aerial Vehicle and LiDAR-derived DEMs to Estimate Channels of Small Tributary Streams. *Remote Sens.* 2021, 3380. https://doi.org/10.3390/rs13173380

3. 1. Introduction

Freshwater ecosystems provide critical habitat for insects, amphibians and other wildlife. Many terrestrial species travel through or settle for a short period of their life cycles in these areas as they seek suitable shelter (Forman, 1995; Wipfli, 1997). The riverine forest provides an important niche for many wildlife species and is also used as a travel corridor for other species, such as birds and small mammals (Naiman *et al.*, 1999; Osbourne *et al.*, 2005; Peak and Thomson, 2006; Rykken *et al.*, 2007). The shoreline vegetation offers shade and wind protection that helps regulate water temperature and increases the dissolved oxygen concentration (Lanini *et al.*, 2004; Caissie, 2006; Garner *et al.*, 2014; Kalny *et al.*, 2017).

One of the most important physical indicators related to freshwater ecosystem assessments is stream location and stream bank condition. In order to evaluate the environmental condition of riparian corridors, it is necessary to quantify vegetation coverage and stream bank morphologic characteristics (stream bed slope and sinuosity) and predict bank erosion rates (Bohn, 1986; Johansen *et al.*, 2013; Tufekcioglu *et al.*, 2020). The presence and distribution patterns of specific plant species growing on stream banks are closely related to fluvial geomorphic processes, bankfull discharge and natural dynamics occurring in these areas (Biedenharn *et al.*, 2000; Loučková, 2012). Additionally, the distribution of herbaceous plant species, woody shrubs and tree species can significantly influence the hydromorphic roughness of the floodplain. It can also affect the transition between the main channel and the floodplain, and modify the dynamics of flood waves (Tabacchi *et al.*, 2000; Forzieri *et al.*, 2012; Apollonio *et al.*, 2021).

The removal of streamside vegetation due to land use activities, such as cattle grazing, can lead to dramatic changes in stream channel size and morphology. Previous studies concluded that grazing activities not only trigger increases in sediment load, but also cause channel incision and widening (Evans *et al.*, 2006; Magner *et al.*, 2008; Zaimes *et al.*, 2019). As a consequence, the effects of increased turbidity and channel widening can severely affect channel morphology and threat fish habitat.

In order to apply management strategies to mitigate the environmental concerns in these areas, the first step is to pinpoint the bank slope position, which can serve as the starting point of further analysis of stream conditions and water quality. Satellite-derived imagery and images obtained with traditional high-altitude aerial photography have been widely used since they cover broad areas. However, the vegetation overhanging on top of a stream channel can partially shade the stream's boundaries and make it difficult to ascertain the exact location of boundaries. This fact becomes particularly exacerbated over small streams where image resolution becomes the limiting factor (Morisawa, 1957; Chorley and Dale, 1972).

Digital elevation models (DEMs) have been widely used as a source for landscape modelling and solving various environmental problems, as an alternative to satellite-derived imagery. The accuracy of DEMs could have a major impact on the quality of DEM-derived landscape matrices, including surface drainage patterns and channel geomorphology prediction (Scannavino *et al.*, 2011; Woodrow *et al.*, 2016). In addition to DEM accuracies, the resolution of DEMs is also critically important for the mapping of small streams and narrow conduits in floodplains. Therefore, coarse-resolution DEMs obtained with traditional photogrammetry cannot preserve fine topographical terrain

features, such as small stream channels, bank locations and bank slopes (Garbrech and Mart, 1994; Zhang and Montgomery, 1994; Dietrich *et al.*, 1995; Hengl, 2006; Sørensen and Seibert, 2007). Additionally, water level fluctuations coupled with stream erosion and sedimentation processes over time can lead the datasets derived from aerial photography to be rapidly outdated, since they are unable to reflect these changes periodically (Smart *et al.*, 2001; Abood *et al.*, 2012; Fernández *et al.*, 2012).

High-resolution LiDAR (Light Detection and Ranging) DEMs can provide more detail to detect and locate microtopographic features at the sub-meter scale (Lane *et al.*, 2009; Buchanan *et al.*, 2013; Thomas *et al.*, 2017). Therefore, they have been used as a source to implement mitigation strategies at critical locations to prevent pollutant transfer and increase pollutant retention (Murphy *et al.*, 2009; Doody *et al.*, 2012). However, LiDAR presents some drawbacks: the dataset production can be costly due to the expensive sensors employed, and the broad geographical areas covered require lengthy software processing times and the need of trained personnel. As a consequence, LiDAR datasets are updated periodically every five years, or longer, which is insufficient to accurately capture the frequent changes often occurring in freshwater ecosystems.

Latest developments in computer science have developed dynamic algorithms capable of data-driven decisions, i.e., Machine Learning (ML), which have been applied to environmental sciences (Haupt *et al.*, 2008; Hsieh, 2009; Thessen, 2016). With the help of ML technology, Islam *et al.* (2021) found that higher resolutions of image and elevation detail could have generated more accurate data for environmental risk assessment. Martinez-Santos and others (2021) used Random Forest (RF) and Super Vector Machines (SVM) to predict and classify the presence of water bodies. Whilst the algorithm performed

well over flat areas, the authors reported some imprecisions over ridges due to the absence of accurate DEMs.

Recent advances, availability and affordability of Unmanned Aerial Vehicles (UAV) coupled with computer algorithms have made their usage a cost-effective alternative to Airborne Laser Scanning (ALS) (Fonstad *et al.,* 2013; Escobar Villanueva *et al.,* 2019; Jeziorska, 2019). Manfreda *et al.* (2018) pointed out that UAVs could be used as the connection device between field observations and spatiotemporal constraints, which could remarkably improve environmental monitoring over small low-order streams.

The integration of a UAV-derived Digital Terrain Model (DTM) can consistently improve the classification accuracy of (1) land cover/image classification and (2) change detection (Zhang *et al.*, 2015; Aguilar *et al.*, 2019; Yao *et al.,* 2019). In this sense, Schumann *et al.* (2019) used UAVs to generate a bare-Earth model and extract floodplain and river cross-section geometries of a small stream in the U.S. They concluded that UAVs were precise and could extract highly detailed topographical data over significantly small scales. Chen *et al.* (2020) compared satellite, LiDAR and UAV-derived DEMs to estimate the vertical errors among these topographic models in order to assess their feasibility in water balance estimations over a wetland area. They concluded that photogrammetric UAVs were a cost-efficient approach for bathymetry estimations.

The proliferation of UAV-based remote sensing techniques has been applied for monitoring and managing natural and sensitive ecosystems, such as peat bogs. For example, Lendzioch *et al.* (2021) sampled groundwater levels (GWL) and soil moisture (SM) in two different locations in Czechia. They concluded that UAV-based thermal data

estimations combined with DSMs can accurately predict spatial distribution of these GWL and SM parameters on peat bogs.

In order to predict stream channel geomorphology, several authors have used different algorithms to locate abrupt changes in channel slope, or areas of rough terrain, using DEMs as a source. Meng *et al.* (2006) elaborated an algorithm called Vertical Slope Position (VSP) which produced realistic delineations of small-scale catchment areas, flow channels, depressions and wet areas. Based on this algorithm, the soil saturation is predicted to be higher in areas close in elevation to their assigned surface water, which decreases the VSP. Thereby, the VSP has been implemented to delineate hydrologic sensitive areas (HSAs) and critical source areas (CSAs) in agricultural catchments, with especial detail in areas intersecting the stream (Murphy *et al.*, 2009). Cartwright and Diehl (2017) used the Slope Gradient (SG) to classify Topographic Position Index (TPI) and predict steep bank slope areas sensitive to geomorphic instability and estimate indicators associated with fluvial erosion risk. They concluded that highly localized areas of high profile curvature and steep slope were probably excessively small to be resolved by 1 m DEMs.

Based on these previous studies, we believe that UAVs could be used as a cost-effective method to map the stream geomorphology and channel boundaries in small watersheds and provide this critical landscape structure parameter that was not easily available in the past. The main aim of this study is to assess the feasibility of precisely mapping lower order stream bank locations with UAV in comparison to LiDAR. We used two algorithms to map the bank location: (i) Slope Gradient (SG) and (ii) Vertical Slope Position (VSP). The accuracies of these two methods in predicting stream bank location were assessed using four different DEMs: a UAV-derived DEM and three provincial DEM

sources; (1) Traditional coarse resolution DEM; (2) LiDAR at 1.2 pulses m^{-2}; and (3) LiDAR at 6 pulses m^{-2}.

3. 2. Materials and methods

3.2.1. Study area

The study was conducted at the Ridge Brook Watershed, which is a small sub-watershed of the Canaan River Watershed in southeastern New Brunswick, Canada (46°01′29.0” N, 65°18′32.5” W; Figure 3.1). The climate in this Canadian maritime province is considered warm-summer humid continental (categorized as Dfb in the Köpen-Geiger system classification; Figure 3.1), with freezing snowy winters and warm summers. The cold winter is generally caused by air masses coming from interior coupled with cold currents coming from the sea. Temperatures are expected to drop to −30 °C or even lower. Summer highs are expected around 32 °C, most likely in the southern part of the province. Precipitation is distributed throughout the year, with expected amounts of 1300 mm over the southern coast, and about half of total precipitation is in the form of snow.

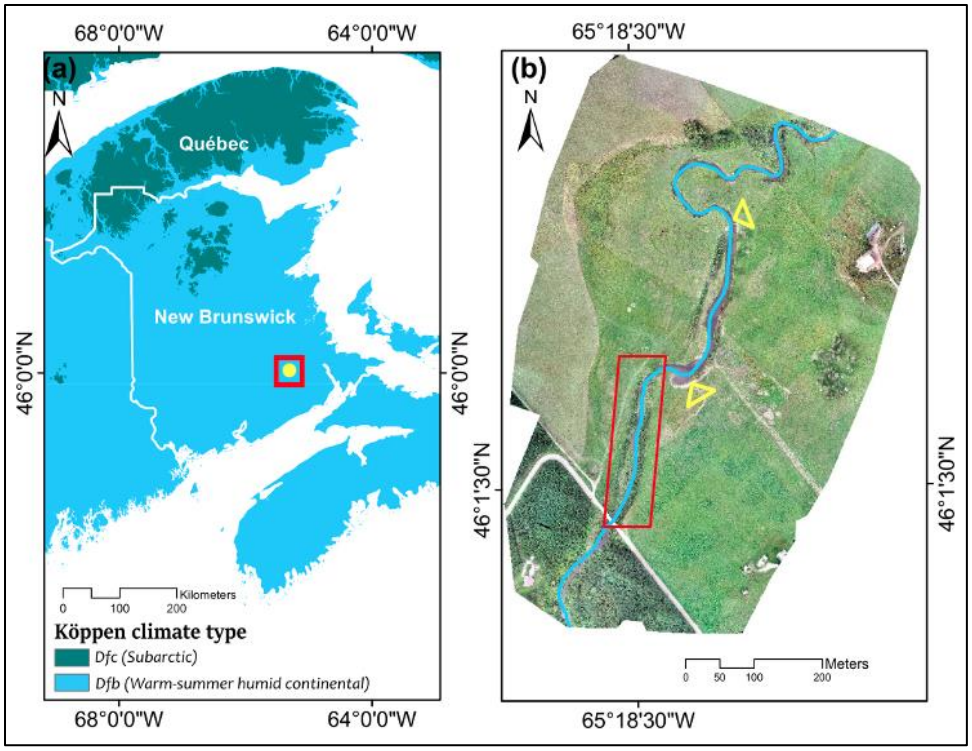

Figure 3.1. a) Köppen-Geiger climate types of Atlantic Canada and the location of The Ridge Brook sub-watershed within the province of New Brunswick (NB, Canada); and (b) the location of the study area (Hicksville settlement, Havelock, NB). In red, the area covered by the bioengineered buffer. Yellow triangles show common areas where cattle cross the stream. The stream follows a South to North direction.

The sub-watershed where the study was conducted covers an area of 7020 ha, with a small-scale limestone extraction operation near the small town of Havelock. The soil type has been classified as Luvisolic, which is commonly found in depressions with poorly drained sites coupled with Regosolic soils. These soils may have an Ah or Ae horizons as top mineral horizons. An Ah horizon is enriched with organic matter often combined with eluvial platy A horizons (Ae). Often, silicate clay has been leached by percolating water to illuvial horizons (Bt) of clay deposition and organic matter storage in imperfectly drained sites. Therefore, Luvisols are typically well supplied with base cations, such as calcium and magnesium, and have loamy or clay-dominated soil textures. Clay in Bt horizon can

be restrictive to air and water movement as well as to root growth. These types of soils are often classified as rapidly to imperfectly drained (Canadian soil classification system). The pH detected in the field is close to 5.5. In agriculture area, mix crops, including grasses, barley and legumes, are commonly observed.

The stream bank is mostly dominated by reed canary grass (*Phalaris arundinacea*), Joe-pye weed (*Eutrochium purpureum*), horse tails (*Equisetum* sp) and cattails (*Typha* sp) as the herbaceous layer. On the other hand, speckled alder (*Alnus incana*), green alder (*Alnus viridis*), red osier dogwood (*Cornus sericea*) and willows (*Salix* sp) dominated the woody shrub strata. The upstream riverine area adjacent to the farm is surrounded by two sections of planted conifer species, red pine (*Pinus resinosa*) and Jack pine (*Pinus banksiana*). These planted species may increase the acidity of the soil in the natural riparian forest, located in the southernmost part of the study area.

Over the past decades, the stream assessments of the Canaan River have reported tremendous development pressures due to forestry and agricultural activities, which have affected the quality and quantity of the adjacent water bodies. Within the study area cattle had access to the stream as a watering source which partially removed the streamside vegetation. As a consequence, sedimentation of sand and gravel deposits increased in stream which led to degradation of water and habitat quality. After a detailed fluvial geomorphic assessment, a bioengineered buffer zone was implemented over a decade ago to re-align the channel based on the natural hydraulic characteristics. This bioengineering buffer zone project added stability to the stream and allowed the recovery of the riverine corridor close to natural condition. Natural pool/riffle spacing was developed, allowing fish to move freely through this section of the brook during any flow conditions, which led

to a progressive recovery of aquatic habitat for salmonids. However, due to the lack of an off-stream watering system for cattle and absence of a dedicated livestock crossing, vegetation is still removed from grazing activities over the streamside areas outside of the bioengineered buffer.

3.2.2. Data collection and data processing

In order to delineate the riverbank and estimate the surface area of the river, four different types of datasets obtained with different methods and resolutions were applied: (1) UAV-derived DEM; (2) coarse resolution DEM, obtained with traditional photogrammetry; (3) LiDAR-derived DEM at 1.2 pulses m^{-2}; (4) LiDAR-derived DEM at 6 pulses m^{-2}.

3.2.3. Unmanned Aerial Vehicle (UAV) and sensors

A DJI Phantom 4 Pro (Nanshan, Shenzhen, China; Da-Jiang Innovations, SZ DJI Technology Co., LTD; Figure 3.2) was used for this study. The Phantom 4 Pro is a vertical takeoff and landing aircraft with total payload of 1388 g including battery and camera. This UAV uses four 2312S Brushless motors powered by a 15.2 V battery with a cruising speed of 72.0 km h^{-1} (s-mode) and a maximum climb speed of 6 m s^{-1}. The maximum wind speed resistance is up to 10.0 m s^{-1}. The reported transmission range with no obstruction or interference is up to 7000 m and the maximum service ceiling is 6000 m asl. The stated maximum flight time with a single battery is 30 min. In our tests, we observed a practical flight time of nearly 25 min, depending on wind speed and temperature (<10 km h^{-1}; >4 °C).

Figure 3.2. The DJI Phantom 4 Pro set up in the field.

The onboard camera is a 1” complementary metal oxide semiconductor (CMOS) with 20M effective pixels (5472 × 3648). The lens has a field of view (FOV) of 84° and the focal length is 8.8 mm/24 mm (35 mm format equivalent) f/2.8–f/11 auto focus at 1 m–∞. During the flight, the image trigger can be activated automatically in autopilot flight mode, with simultaneous timestamps. The sensor registers either vertical images captured at nadir angle, for 2D maps, or off-nadir angles (up to 90 degrees) for 3D Digital Surface Model (DSM) reconstructions. Due to its multiple satellite position navigation system (GPS & GLONASS), the aircraft can automatically record GPS locations. Images and metadata are automatically stored with a 64 GB Lexar high performance 633x MicroSDXC UHS-I Secure Digial Card (SD-Card).

This DJI Phantom 4 Pro was chosen due to its recognized camera stability (Shamshiri *et al.*, 2018; Krisanski *et al.*, 2020). This UAV outperformed other UAVs (e.g., DJI Mavic Pro, DJI Matrice 210 and DJI Inspire 1) tested in a previous study led by Rogers *et al.* (2020). It provided the highest prediction accuracy in four of the six land covers tested (forest, vines, bare soil and mowed grass). This study also stated that the Phantom 4 Pro provided the best balance between size and sensor resolution. Kuželka and Surový (2018)

concluded that the images acquired with this UAV had higher quality and detail than DJI Mavic Pro due to its larger sensor and higher sensor resolution.

3.2.4. UAV data collection

Parallel flight grid missions were programmed in order to collect images with the UAV. We used a side image and frontal overlap rate of 80%, during pre-leaf conditions to cover 36 ha, in May 2019. We acquired 1027 images in two flights, with an average flight speed of 7 m s^{-1} at near-ground elevation (80 m); all images were captured at nadir camera angle. Wind speed was less than 10 km h^{-1} during flight time and the sky was partially overcast, with few clouds and low sunlight intensity. This particular season provided the best field conditions to obtain aerial images of the stream, since the stream bank's herbaceous vegetation was still snow-flattened, but without residual snow cover on the ground. This helped to reduce the potential elevation error caused by the height of streamside vegetation observed during summer and fall. Therefore, no seasonal analysis was performed.

The captured images were processed under the Structure-from-Motion (SfM) algorithm to generate geo-rectified orthomosaic images using software package Pix4D 4.4 (Prilly, Switzerland; Pix4D S.A.). The latitude, longitude and altitude (WGS84 projection) recorded in metadata with onboard GPS of UAV were used to position the aerial photos first. Common points from different images in the overlap areas were used as keypoints to build a 3D projected point through aero-triangulation (Wolf and Dewitt, 2000). In order to improve the software image stitching, 10 manual tie points (mtps) were added in the planted forest area upstream. Additional errors originating from lens distortion, GPS position error, aircraft attitude uncertainty and errors in time domain can lead to decreased

accuracy in the relative UAV map geolocation (Fabian *et al.*, 2020). Therefore, the overall geolocation was corrected using the target coordinates as checkpoints, acquired with handheld GPS as relative accuracy (Grau *et al.*, 2021). Six ground control markers (square targets of 1.44 m^2) were equally distributed across the site and at the boundaries of the study area, including next to the watercourse at different elevations (Figure 3.3). In order to mark the positions of the panels with geometrical precision, a ground control point (GCP) of each target's corners was recorded with a Trimble Geoexplorer 6000 Series handheld GPS for georeferencing accuracy. For each record, the GPS device was connected to a minimum of 16 satellites available and the precision observed during the geolocation acquisition was 10 cm. The GPS was placed on a static position for 30 seconds on each GCP using Real Time Kinematics (RTK) mode.

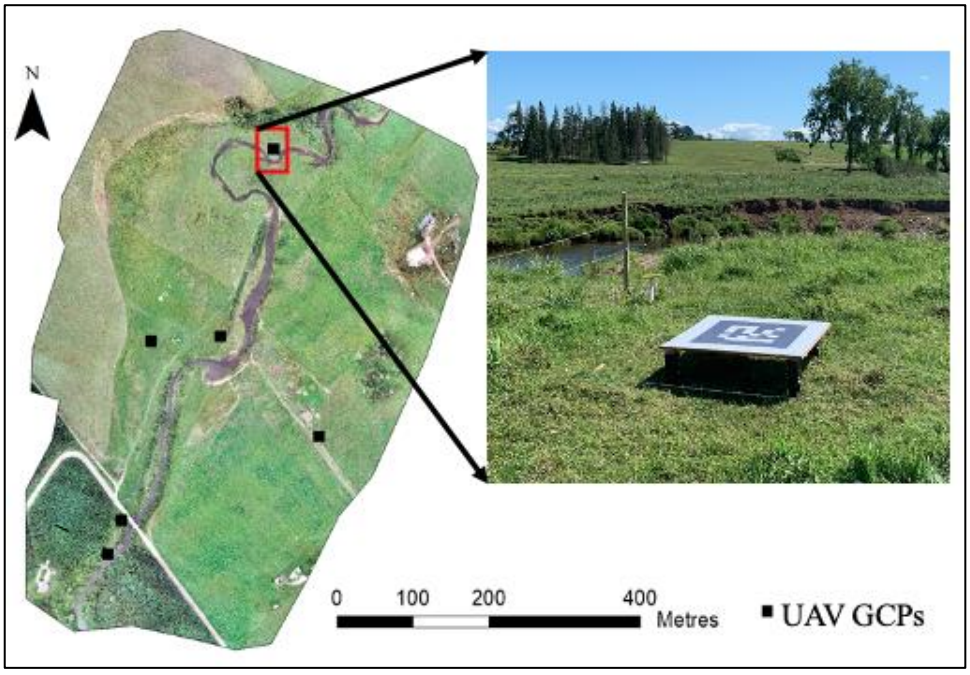

Figure 3.3. Distribution of the GCPs in the study area.

3.2.5. Point cloud editing

Overall, the software can automatically classify different land uses, such as pastures, road, buildings, high vegetation and roads, with acceptable accuracy. However, finer manual classification was undertaken in order to correct potential 3D point punctual misclassifications of ground or vegetation, to avoid errors in the digital ground surface model (Poppenga *et al.*, 2010). In addition to the error caused by stream bank vegetation, another source of error was found within the stream channel. This was potentially caused by floating objects moving on the water's surface as well as light/illumination changes between images captured at different times (i.e., reflection, absorption and refraction). In some areas, the UAV camera could penetrate the water surface and captured the stream bed, while in other high-reflection conditions the light could not penetrate the water's surface. This is a common source of error, or noise, in the estimation of surface elevation (Hashemi-Beni *et al.*, 2018; Jeziorska, 2019). For these reasons, points classified as water were removed in order to reduce the elevation uncertainties for the estimation of the stream channel, the triangulation, and the effects on the quality of the DEM (Hashemi-Beni *et al.*, 2018). The resulting point cloud had an average density of 833 points m^{-2} and it was further interpolated at 0.3 m resolution, using the LAStools commercial software suite (Martin Isenburg, LAStools-efficient tools for LiDAR processing).

3.2.6. Traditional DEM and LiDAR DEMs

The coarse resolution DEM obtained with traditional photogrammetry was acquired from the Service New Brunswick (SNB; http://www.snb.ca/geonb1/e/dc/catalogue-E.asp accessed July 1st, 2021). The accuracy of a single elevation point was approximately 2.5 m and the spacing between the elevation points was nearly 70 m on average, with increased

density in more complex terrain areas. We generated a DEM at a 2 m cell size using the Inverse Distance Weighted (IDW) interpolation method.

The LiDAR DEMs were obtained from SNB geographic database. The point cloud density of the LiDAR dataset collected in 2013 was 1.2 points m^{-2}, with horizontal accuracy of 0.3 m and vertical accuracy of 0.133 m at 95% confidence level. The point cloud density of the LiDAR dataset collected in 2018 was 6 points m^{-2}, with horizontal accuracy of 0.20 m and vertical accuracy was RMSE Z = 10.5 cm, equating to ± 20.6 cm at 95% confidence level.

It is essential to remove points being classified as water when processing LiDAR DEM. The elevations of water points (such as depressions) are lower than their surroundings, and as such the overall accuracy of the interpolated surface between points may decrease if a significant number of these points are present but not resolved. Thus, the LiDAR hydrologic enhancement correction was applied prior to DEM generation, as recommended by previous researchers (Brzank and Heipke, 2006; Wu *et al.*, 2009). The DEM raster was generated with Natural Neighbor interpolation with 30 cm resolution.

3.2.7. Stream network

Spatial hydrology tools of ArcGIS (10.5) were used to generate stream networks using the previously described DEMs as inputs. For the coarse resolution DEM, "stream burning" of the provincially field-mapped open drainage channel network (SNB Geospatial Database) was used to lower cells in the interpolated DEM to invigorate overland flow through mapped feature locations (Zhang and Montgomery, 1994). The resolution of this topographic model was excessively coarse to capture and represent narrow topographic

features such as stream channels due to surface generalizations of the terrain (Ostman, 1987; Hancock, 2005).

Although LiDAR- and UAV-derived DEMs do not require stream burning due to high point cloud density, hydro-conditioning was still required to remove local depressions created by natural or artificial landscape features. The eight-direction flow model (D8 algorithm, (O'Callaghan and Mark, 1984)) was used to derive the flow network and calculate the flow accumulation. The minimum flow initiation threshold for flow accumulation was set as 4 ha (equivalent to 444,444 DEM cells for high-resolution DEMs and 10,000 cells for coarse DEMs), to remove seasonal streams from the map and to geographically represent drainage of only the main channel with average water flows year-round.

3.2.8. Stream Channel Boundary Prediction Methods

In this study, two methods were used to represent stream hydrogeomorphology and to predict stream channel boundaries: the Slope Gradient (SG) and the Vertical Slope Position (VSP). The Slope Gradient method assumes that a marked degree of change in elevation along the land/water interface could be detected by the steep slope of a stream bank, and this abrupt steep slope could be detected with high-resolution DEMs. Average zone slope threshold values were extracted by overlaying a line feature that intersected the land/water border predicted by the DEM. Due to the relatively small extent of interest, it was assumed that the natural slope gradient was negligible and this was the average value used. With "ground" class selected in high-resolution point clouds (LiDAR and UAV), the area between both stream bank sides would be estimated as water surface, in the particular time of data collection, for each data source. In higher-resolution datasets, target raster zones

were cleaned (filtered) by a series of raster functions to (1) remove small zones (using shrink function), (2) perform an area-based threshold of remaining zones (region group and zonal geometry functions) and (3) expand remaining zones back to their original extent.

The Vertical Slope Position (VSP) is defined as the elevation differences between the land and the nearest water surface and calculated by integrating the elevation difference for each cell alone to the nearest water body (Meng *et al.*, 2006):

$$VSP = min \sum (d * s)$$

where "d" is the distance between two adjacent cells (m) and "s" is slope steepness (m m^{-1}).

The groundwater table thresholds set in DEMs are representative of the depth to water or elevation difference to water. Cells with a VSP below a threshold value were classified as stream channel and the threshold value was calibrated with field data.

3.2.9. Field-validation and statistical analysis

The Trimble Geoexplorer 6000 GPS unit (10 cm accuracy) was used to record the stream bank location in RTK mode with a minimum of 16 satellites available and a reported error of 10 cm. We recorded the location where herbaceous emergent aquatic species were found. The distribution and density of these plant species could be used as an indicator of the most representative long term processes occurring on the stream bank (Biedenharn *et al.*, 2000; Loučková, 2012). In sections where high dense riparian vegetation impeded proper human access to the stream, 150 singular GPS waypoints were collected to complete the field delineation. In addition, we also measured 25 field-cross sections selecting the areas partially covered by the dense canopy where the human access was difficult. Within a distance of 1.04 km of the stream surveyed, field-cross sections ranged from 5.5 m in the

partially restored area to 19 m in the widest section of the stream, near the section where cattle grazed more intensely.

The LiDAR hydrologic enhancement correction, detailed previously, reduced the natural land features, such as rock outcrops and small stream islands, detected by LiDAR within the stream channel. This fact isolated the slope gradient maximal change detection towards the longitudinal narrow boundary and improved its prediction. We obtained the same effect by removing the points classified as water from the UAV point cloud.

For the VSP map, different elevation thresholds were tested in order to maximize the correctness and minimize both errors of omission (false negative) and commission (false positive) by using the field-validated GPS transect as a reference.

The receiver operating characteristic (ROC) curves optimized the trade-off between the false positive rate (error) and the true positive rate in predicting the stream boundary, at various threshold settings (shown as cumulative probability; (Fawcett, 2006; Ariza López and Atkinson Gordo, 2008)). Intervals of 0.5 m of error were used to estimate the correctness (cumulative probability extracted from ROC curves) of each DEM, in order to determine the percentage of agreement between the predicted and observed stream bank locations. Mean squared errors (MSE) were used to measure of the degree of agreement between predicted and observed stream bank locations:

$$MSE = \frac{1}{n}\sum_{i=n}^{n}(Y_i - \hat{Y}_i)^2$$

where Y is the vector of observed values (precise location recorded with GPS) of the i variable predicted and $\hat{Y}$ are the predicted DEM values, measured in meters. Figure 3.4 summarizes the methodology used in this study.

Mean relative error (MRE) was used as the second indicator to assess the goodness of fit:

$$MRE = \frac{1}{n}\sum_{i=n}^{n}\frac{\left|\hat{Y}_i - Y_i\right|}{Y_i}$$

The Kling-Gupta Efficiency (KGE) proposed by Kling *et al.* (2012) was calculated to measure the goodness-of-fit. This indicator has been widely used in recent years to ensure that the bias and variability ratios were not cross-correlated (Thirel *et al.*, 2015; Pool *et al.*, 2018):

$$KGE = 1 - \sqrt{(PC - 1)^2 + (\frac{sdp}{sdo} - 1)^2 + (\frac{mp}{mo} - 1)^2}$$

where *PC* corresponds to the Pearson Coefficient value, *mo* is the average of observed values and *mp* is average of predicted (DEM) values. The standard deviation of observed values is represented as *sdo* and standard deviation of predicted values is represented in *sdp.*

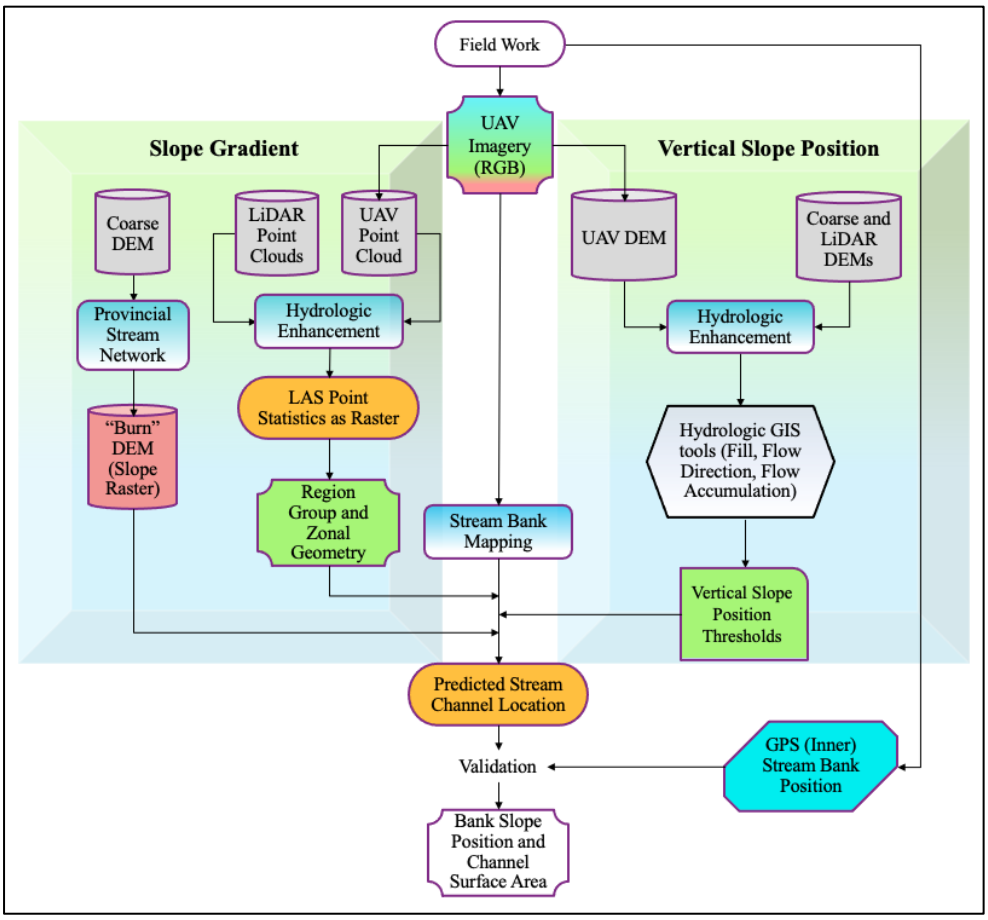

Figure 3.4. Flow chart for mapping of stream bank location and channel surface area with coarse, LiDAR and UAV-derived DEMs.

3. 3. Results

3.3.1. UAV-derived DEM geolocation accuracy

Since the Phantom 4 Pro was capable of automatically recording GPS locations, we used this product as the relative geolocation. However, adverse factors such as lens distortion, GPS position error, aircraft attitude uncertainty and errors in time domain can lead to decreased accuracy in the relative UAV map geolocation, as reported by Fabian *et al.* (2020). Therefore, the overall geolocation was corrected using the target coordinates as checkpoints, acquired with handheld GPS as relative accuracy. The elevation Root Mean

Squared Error (RMSE) for these GCPs was 0.075 m, and the horizontal RMSE for longitude and latitude were 0.078 and 0.066 m, respectively. These results indicate high precision between the measured coordinates (GCPs registered in the field) compared with the software-calculated position**.** Elevation ranges predicted for each DEM for the study area can be seen in a previous study (Grau *et al.*, 2021), where the same elevation sources were used**.**

3.3.2. Stream Channel Boundaries Prediction by Slope Gradient method

The stream bank predicted using the Slope Gradient method is shown in Figure 3.5. As shown, the highest density among these datasets can be observed in the UAV point cloud (Figure 3.5i). This dataset covered the entire study area except for a few narrow sections (empty gaps) due to presence of high vegetation located by the streamside. The LiDAR 6.0 also covered the entire study area (Figure 3.5f), except the area where the high vegetation of the bioengineered buffer was found. Conversely, due to the remarkably lower density of points collected by LiDAR 1.2 (Figure 3.5c), the portions of ground without data increased significantly. The coarse-resolution DEM was not only unable to determine the location of the stream bank's boundaries (Figure 3.5a) but also insufficient to reflect the width changes along the flow network with acceptable accuracy just by visual assessment.

Before filtering, the channel predicted by the LiDAR 1.2 DEM was significantly more accurate than that of the coarse DEM (Figure 3.5d). However, there were considerable isolated pocket areas in riparian zones being classified as stream channel based on LiDAR 1.2 DEM. This fact resulted in a significant overestimation of the stream bank boundary. After filtering, the prediction accuracy was significantly improved because those isolated pocket areas were eliminated. However, there were still remarkable errors in area with

fenced riparian zones and the predicted stream channels resulted considerably wider (light blue areas in Figure 3.5e) compared to the field-mapped stream channel within red lines.

The stream bank delineated with LiDAR 6.0 DEM resulted in a smoother and more explicit channel compared with that of LiDAR 1.2 (Figure 3.5h). However, errors in area with fenced riparian zones and predicted stream channels were still considerably wider than field mapped stream channel, which was similar to the stream channel predicted by LiDAR 1.2. The stream channel predicted by the UAV-derived DEM was more accurate than LiDAR 1.2 and LiDAR 6.0, even before the filtering method was applied (Figure 3.5j).

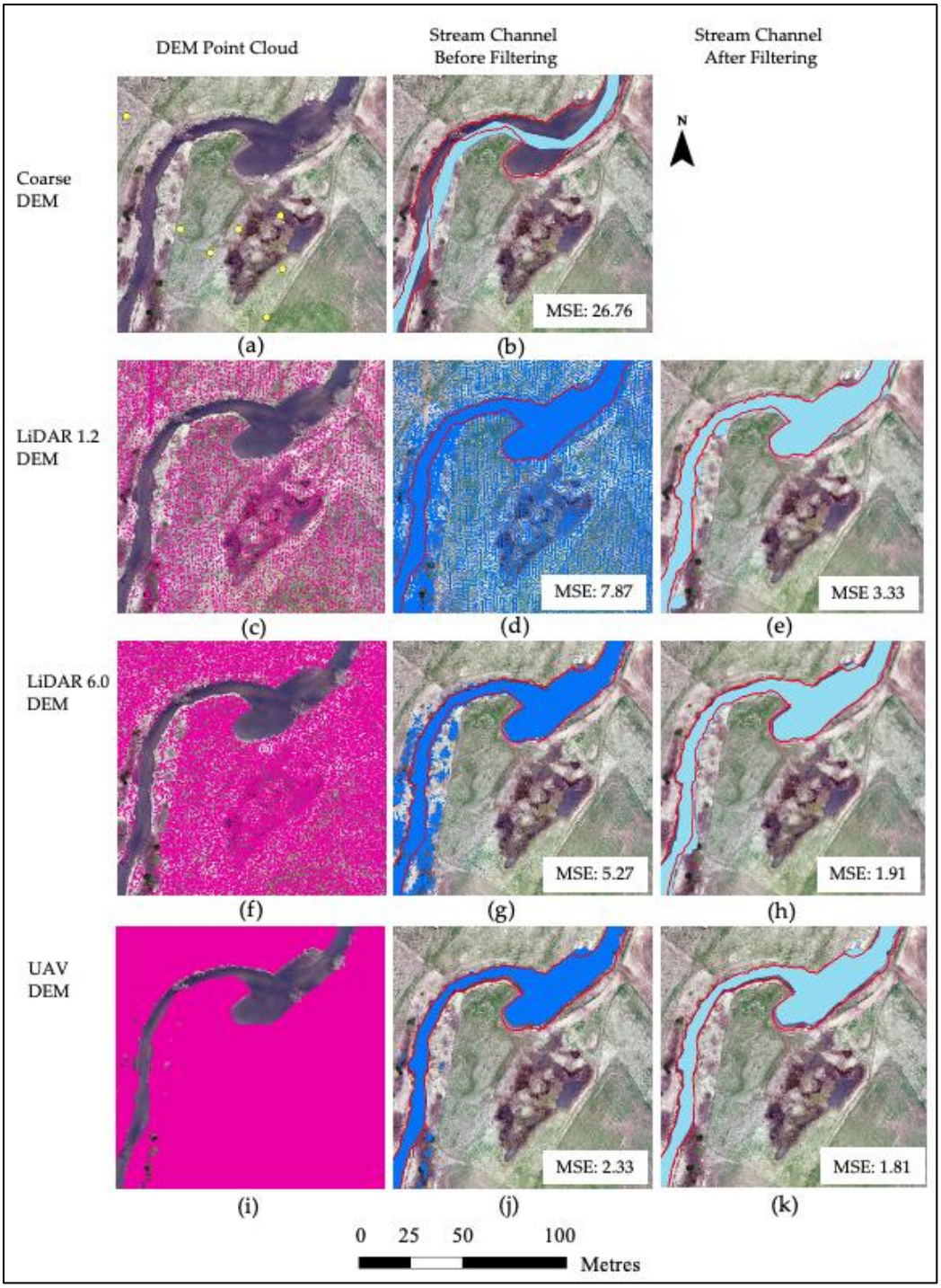

Figure 3.5. Point clouds ("ground" class) of the four different DEM sources are represented in (a) coarse DEM, (c) LiDAR 1.2, (f) LiDAR 6.0 and (i) UAV. Stream channels predicted with Slope Gradient method before applying the Region Group filter represented in (b) for coarse DEM, (d) LiDAR 1.2, (g) LiDAR 6.0, (j) UAV and after applying the Region Group filter represented in (e) for LiDAR 1.2, (h) LiDAR 6.0 and (k) UAV.

The cumulative probabilities (correctness) of the stream channel boundary predicted before filtering are shown in Figure 3.6. Channel boundary was predicted with 89% accuracy within an error of 2 m for the UAV-derived DEM, compared with the accuracy of 80% and 67% for the LiDAR 6.0 and LiDAR 1.2 DEMs, respectively. For the coarse DEM, the accuracy was only 26% for the probability of estimating the stream channel within 2 m of error.

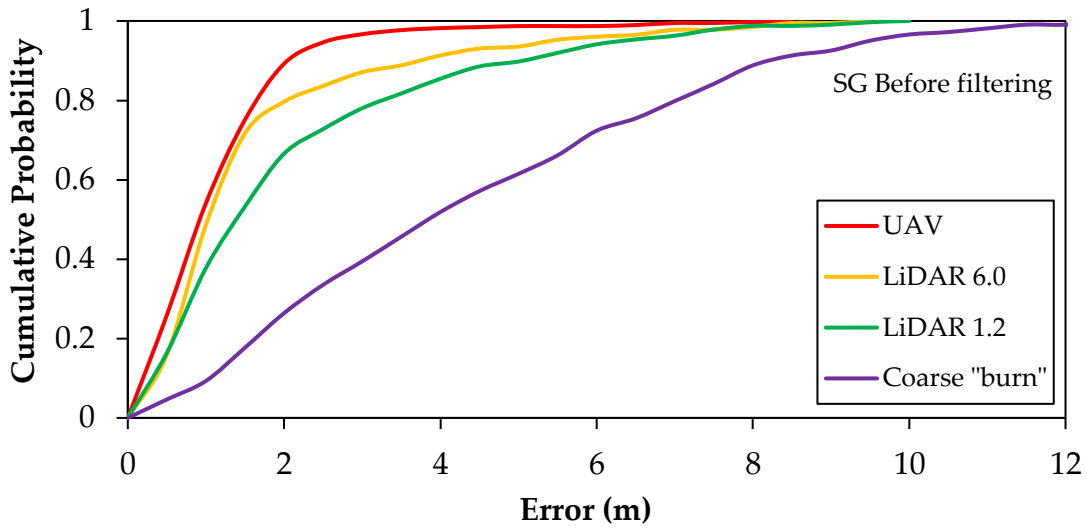

Figure 3.6. Receiver Operating Characteristic curves (ROC) representing cumulative probability of the Slope Gradient in predicting stream channel associated to error (m) prior to applying filter.

The cumulative probabilities (correctness) of stream channel boundary predicted after filtering are shown in Figure 3.7. After application of filtering, channel boundary predicted by the LiDAR 6.0-derived DEM had a probability of 88% within an error of 2 m, which represents an increase of 8% with respect to the same probability before applying the filter. A fact worth mentioning is the improvement experienced by the LiDAR 1.2-derived DEM, which was able to predict the stream bank boundary with a probability of 82% within an error of 2 m. This represents an increase of 15% in accuracy with respect to the same

probability prior to applying the filter. However, the percentage of improvement post applying the filter did not change substantially for the UAV-derived DEM compared to LiDAR, since the filter did not increase the accuracy significantly.

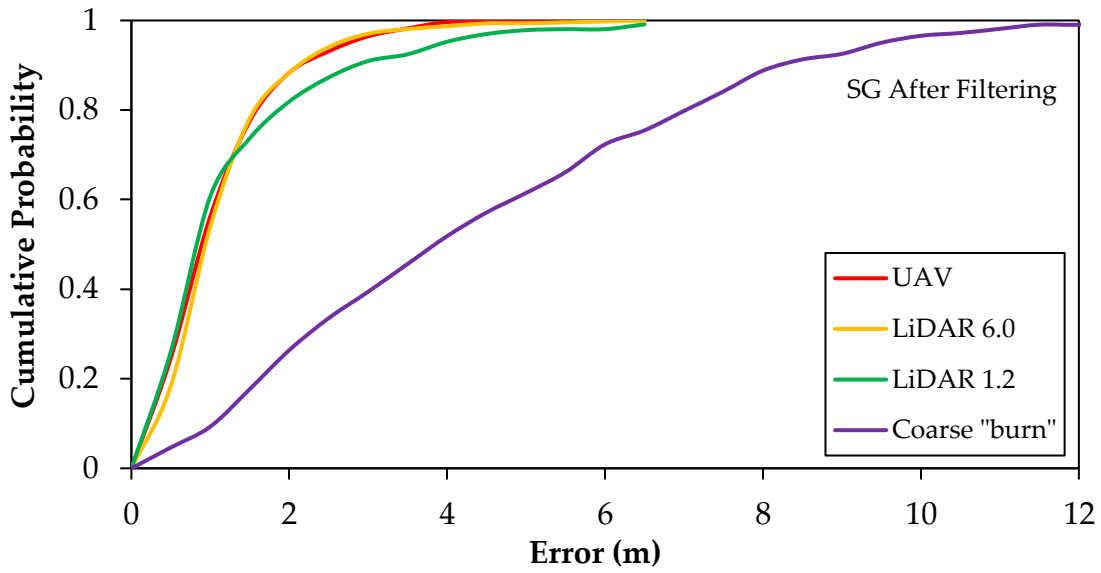

Figure 3.7. Receiver Operating Characteristic curves (ROC) representing cumulative probability of the Slope Gradient in predicting stream channel associated to error (m) after filtering.

Mean relative errors (MRE) and Kling-Gupta efficiencies (KGE) regarding the stream bank prediction for each DEM can be seen in Table 3–1. As shown, the coarse DEM registered the highest mean relative error (0.50) of all the topographic models used, and predicted the stream bank boundary with the lowest KG efficiency of only 34%. These results agree with the MSE values obtained previously, due to the low resolution of this elevation model. Among the high-resolution DEMs, the UAV-derived DEM predicted the stream bank boundary with an efficiency of 82%, followed by LiDAR 6.0 (KGE = 70%), prior to applying the filter. The LiDAR 1.2 was able to predict the stream bank boundary with an accuracy of 67% before applying the filter.

The KG efficiencies improved significantly after applying the Region Group filter. When the LiDAR 1.2 was used as a source the KGE value increased by 13%, from 67% to 80%, which reduced the MRE error by, practically, 0.1 units. A similar trend was observed in the LiDAR 6.0, where the KGE increased by 15%, from 70% to 85%. In this case, the MRE was reduced from 0.24 to 0.15 post applying the filter. The changes observed for the UAV-derived DEM were not as significant, and the MRE value was reduced from 0.17 to 0.14 post filtering. Nonetheless, the KGE achieved the highest precision among the high-resolution DEMs with 86%.

Table 3–1. Mean Squared Errors (MSE), Mean Relative Errors (MRE) and Kling-Gupta Efficiencies (KGE) before filtering (BF) and after filtering (AF) for each DEM; (N/A = not applicable).

Estimator	Coarse DEM	LiDAR 1.2	LiDAR 6.0	UAV DEM
MSE BF	26.76	7.87	5.27	2.32
MSE AF	N/A	3.33	1.91	1.81
MRE BF	0.50	0.29	0.24	0.17
MRE AF	N/A	0.20	0.15	0.14
KGE BF	0.34	0.67	0.70	0.82
KGE AF	N/A	0.80	0.85	0.86

3.3.3. Stream Channel Boundaries Prediction by Vertical Slope Position(VSP)

The stream channel, classified with the VSP thresholds method, is shown in Figure 3.8. With VSP = 0.2 m threshold, the MSE between predicted and actual stream channel was 9.70 for LiDAR 1.2, which was the optimal threshold for this dataset. With the same VSP threshold, the MSE was 11.85 for LiDAR 6.0 and 18.68 for the UAV-derived DEM. The optimal threshold for LiDAR 6.0 and UAV was 0.25 m with MSE = 11.45 and MSE = 15.12, respectively. For the coarse resolution DEM, MSE was 20.78 using 1.0 m as optimal classification threshold and 32.62 with 1.5 m as threshold classifier.

In general, predicted errors measured with MSE were substantially higher than that of the Slope Gradient method for all high-resolution DEM sources (9.70 to 15.12 compared to 1.81 to 3.33). Nonetheless, the results for the coarse-resolution DEM improved when the VSP method was applied (from 26.76 to 20.78). With the Slope Gradient method, the UAV-derived DEM produced the best results, followed by LiDAR 6.0 and LiDAR 1.2. However, with the VSP method the LiDAR 1.2 DEM performed the best, followed by the LiDAR 6.0 and UAV-derived DEMs. A related point to consider is the MSE obtained for the coarse DEM was fairly close to the performance of the UAV-derived DEM. This result indicated that the VSP method is not as sensitive to DEM accuracy and resolution compared to the Slope Gradient method. Based on the visual assessment of the image (Figure 3.8), the coarse DEM appeared to be more accurate over the narrow section of the stream than in the wider section without dense vegetation cover along the stream bank (Figure 3.8a). Similar performance was observed when the UAV-derived DEM was used as a source, where higher discrepancies were observed in areas with open water sections of the stream (Figure 3.8d).

As reflected by MSE values, LiDAR 1.2 provided high agreement with the VSP method and was able to predict the area occupied by the stream channel better than LiDAR 6.0. This was especially true in the narrowest section of the stream, located at the bottom section of Figure 3.8b. We also noticed that with the VSP method, the UAV-derived, DEM-predicted stream channels did not agree with the field survey, and this was especially true in the widest section of the stream channel. This is likely due to DEM errors caused by light reflection of water surfaces due to the lack of high vegetation coverage on the stream bank (Figure 3.8d).

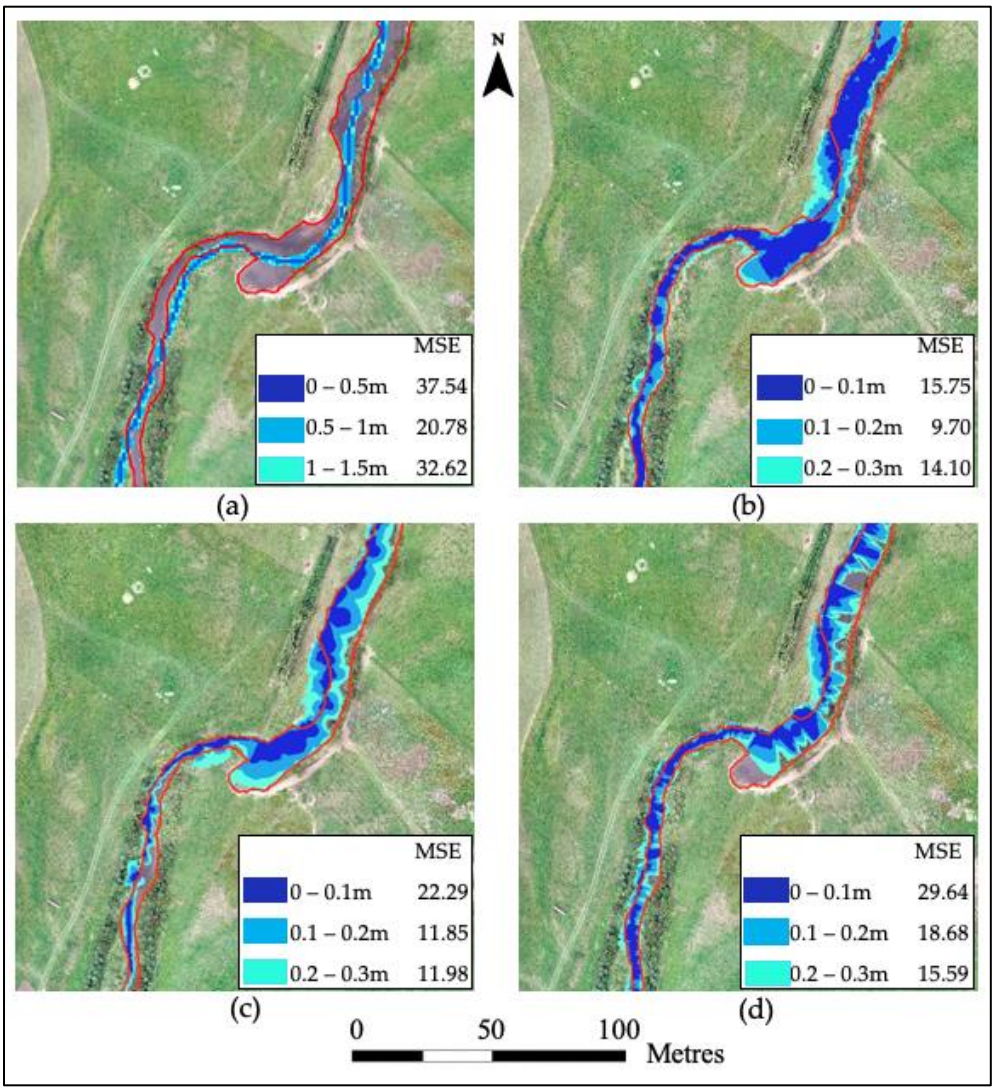

Figure 3.8. Results for the VSP thresholds tested in order to predict the channel surface overlayed on a UAV image using (a) Coarse DEM; (b) LiDAR 1.2; (c) LiDAR 6.0 and (d) UAV and the corresponding mean squared errors (MSE) in meters. In red lines, the field-validated stream bank location.

Receiver Operating Characteristic curves also confirmed that the VSP did not perform as accurate as the SG when high resolution DEMs were used as a source (Figure 3.9). As shown, the LiDAR 1.2 provided the most reliable estimation and was able to predict the channel surface with 60% agreement within an error of 2 m. When the LiDAR 6.0 was used as a source the probability of defining the stream bank with this topographic model

was 57% within an error of 2 m. The UAV-derived DEM was able to predict the stream channel with a probability of 56% with the same reported error of 2 m. When the coarse DEM was used as a source, the probability of intersecting the stream edge was 20% within an error of 2 m.

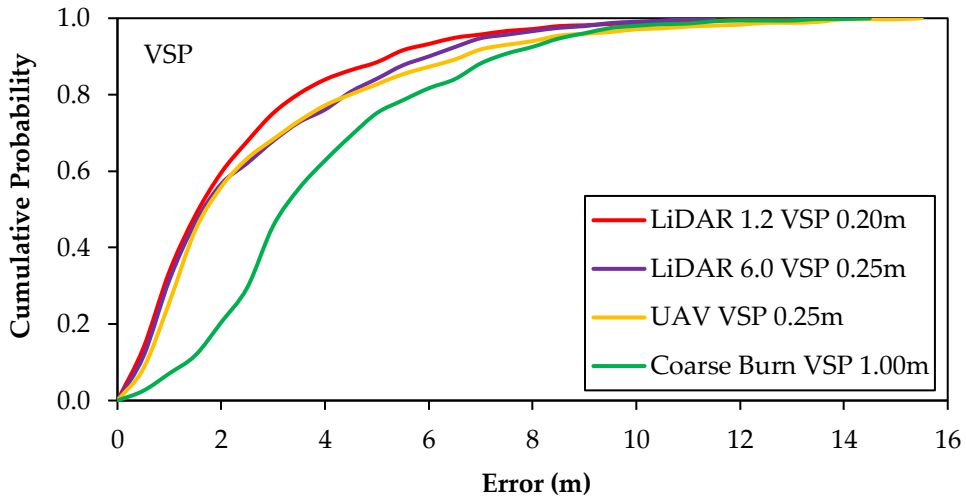

Figure 3.9. Receiver Operating Characteristic Curves (ROC) representing the accuracy of the optimal Vertical Slope Position (VSP) thresholds in mapping the channel surface using the following DEMs: Coarse DEM, LiDAR 1.2, LiDAR 6.0 and UAV.

Results for the MRE and KGE for each of the VSP thresholds tested for each DEM can be seen in Table 3–2. As shown, the coarse DEM was unable to precisely detect the stream bank's location. When this topographic model was used as a source, the boundaries of the stream were predicted with an accuracy of 28% using 1 m as a VSP threshold. The MRE for this cut-off point was remarkably high, at 0.45.

Table 3–2. Mean Squared Errors (MSE), Mean Relative Errors (MRE) and Kling-Gupta Efficiencies (KGE) for each VSP threshold tested; (N/A = not applicable).

Threshold	Coarse DEM	LiDAR 1.2	LiDAR 6.0	UAV DEM
MSE VSP 0.50 m	37.54	N/A	N/A	N/A
MRE VSP 0.50 m	0.47	N/A	N/A	N/A
KGE VSP 0.50 m	0.24	N/A	N/A	N/A
MSE VSP 1.00 m	20.78	N/A	N/A	N/A
MRE VSP 1.00 m	0.45	N/A	N/A	N/A
KGE VSP 1.00 m	0.28	N/A	N/A	N/A
MSE VSP 1.50 m	32.62	N/A	N/A	N/A
MRE VSP 1.50 m	0.48	N/A	N/A	N/A
KGE VSP 1.50 m	0.27	N/A	N/A	N/A
MSE VSP 0.10 m	N/A	15.75	22.29	29.64
MRE VSP 0.10 m	N/A	0.28	0.32	0.34
KGE VSP 0.10 m	N/A	0.59	0.40	0.38
MSE VSP 0.20 m	N/A	9.70	11.85	15.68
MRE VSP 0.20 m	N/A	0.29	0.30	0.31
KGE VSP 0.20 m	N/A	0.67	0.55	0.47
MSE VSP 0.25 m	N/A	11.86	11.45	15.12
MRE VSP 0.25 m	N/A	0.33	0.29	0.28
KGE VSP 0.25 m	N/A	0.64	0.63	0.53
MSE VSP 0.30 m	N/A	14.10	11.98	15.59
MRE VSP 0.30 m	N/A	0.37	0.35	0.35
KGE VSP 0.30 m	N/A	0.57	0.58	0.50

Among the high-resolution DEMs, LiDAR 1.2 was able to predict the stream bank with higher precision, followed by the LiDAR 6.0- and UAV-derived DEMs. When the LiDAR 1.2 was used, the VSP predicted the location of this parameter with a precision of 67% when the VSP threshold used was 0.20 m. When LiDAR 6.0 was used, the optimal efficiency (63%) was registered with a threshold of 0.25 m of depth. With this breakpoint, the boundaries of the stream bank were predicted within an error of 0.29 when this DEM

was used as a source. Finally, the same threshold proved optimal for the UAV-derived DEM and was able to predict the stream bank's location with an accuracy of 53%.

3. 4. Discussion

3.4.1. Slope Gradient method

Based on the results obtained, the Slope Gradient derived from the coarse DEM did not provide accurate results when predicting the stream's boundaries. This can be explained by the significantly lower number of points recorded in this dataset used to derive the DEM (Figure 3.5) compared to higher-resolution DEMs. This reflects its inability to locally adjust the grid size to the dimensions of the topographic land surface features and resulted in its unsuitability for the parameterization of precise drainage features, a situation exacerbated in low relief landscapes (Coverages, 1995). The absolute elevation accuracy of this provincial topographic model was reported to be 2.5 m, which makes it unable to accurately represent average elevation change per pixel (Gyasi-Agyei *et al.*, 1995; Murphy *et al.*, 2009).

Conversely, the UAV achieved the highest accuracy of all data sources, followed by high-resolution LiDAR 6.0 and LiDAR 1.2. This is likely due to the higher point cloud density generating a more precise topographic model (DEM). Furthermore, the UAV-derived DEM was obtained during the leaf-off conditions and snow-flattened stream bank vegetation, which could potentially increase the precision. Additionally, due to more sunlight penetrating these vegetated areas, the land/water boundaries were particularly discernible and represented this edge accurately. This result indicated that the accuracy of the Slope Gradient method to identify the stream channel is highly dependent on the DEM's resolution and accuracy; this is in agreement with results reported by previous

researchers (Zhang and Montgomery, 1994; Sonneveld *et al.*, 2006; Buchanan *et al.*, 2014; Petrasova *et al.*, 2017). In general, these studies found that higher-quality vertical information resulted in appreciable improvements in the smooth representation of subtle topographic surfaces, more precise delineations of hydrologically relevant parameters and more appropriate model outputs. The findings of this study provide evidence that UAVs can be applied to monitor stream bank shift, erosion and sedimentation processes over time. It could be used as a suitable means to address the limitations of field-based approaches (resource constraints and land-access restrictions) for stream bank assessments (Rahman *et al.*, 2017; Hashemi-Beni *et al.*, 2018; van Iersel *et al.*, 2018).

We observed that LiDAR (both 1.2 and 6.0) tended to overestimate the stream bank location in areas, partially those covered by high vegetation. This is likely caused by insufficient ground elevation points due to vegetation coverage. On the other hand, the stream edge was slightly underestimated in areas covered by herbaceous species. This can be explained by the season when LiDAR was acquired; LiDAR sources were acquired in summer during leaf-on conditions, when the stream's herbaceous vegetation was denser and taller compared with early spring. Therefore, LiDAR-derived DEMs performed slightly less accurately in detecting exact land/water boundaries.

3.4.2. Vertical Slope Position method

Similar to the Slope Gradient method, the coarse DEM acquired with traditional aerial photographs did not perform as precisely when predicting the stream's boundaries compared to higher-resolution sources used. This is likely due to the lack of topographic detail (Figure 3.5a). However, VSP-predicted stream channels were substantially more accurate than the Slope Gradient method, with MSE = 20.78 vs. 26.76 m. We observed

that the accuracy of the VSP method decreased dramatically for all higher-quality DEMs, from LiDAR 1.2 to UAV-derived DEMs. These results seem to agree with the findings reported in previous studies; very high-resolution DEMs may also become inappropriate for groundwater flow predictions (Kuo *et al.*, 1999; Emanuel, 2013). Groundwater paths are assumed to follow more general landscape topographies rather than small-scale surface variations. Thus, smoother topography represented in LiDAR 1.2 performed better to represent near-surface flow pathways and water table positions (Marklund, 2009; Gillin *et al.*, 2015).

The VSP method with the UAV-derived DEM as data source performed better over the bioengineered buffer but failed to predict the correct stream boundary in sections with wider channels. These mismatches can be caused by two factors: (i) mapping the stream in areas partially covered by the canopy proved the main disadvantage of photogrammetry, since the camera could not penetrate the dense canopy and would not detect the ground surface elevation (Alidoost and Arefi, 2017; Skarlatos and Vlachos, 2018). As a consequence, these canopy-shaded areas would have either unprecise elevation estimations or would have been classified as areas with missing data. This would lead to a significant reduction of data point information in these specific areas. Thus, the photogrammetric software was unable to create sufficient terrain points in these particular areas and became less accurate when interpolating the DEM, as reported by previous studies (Rahman *et al.*, 2017; Hashemi-Beni *et al.*, 2018; van Iersel *et al.*, 2018). Secondly, (ii) imagery acquired during daylight hours led to some distortion when flying the UAV over water surfaces, since water has a tendency to selectively reflect, refract or absorb light. This would increase

the noise in the section of open water. As a result of these low-quality photogrammetry sections, the stream channel became significantly more distorted and uneven.

3. 5. Conclusions

This study assessed the feasibility of using a UAV to map the stream geomorphology and stream banks over an agricultural watershed. The accuracy of the UAV-derived DEM was also compared with other commonly used DEMs including high-density LiDAR, low-density LiDAR and traditional high-altitude, orthophoto-derived coarse resolution DEM. Two methods were used to predict stream channel surface areas, namely the Slope Gradient and Vertical Slope Position methods.

When the Slope Gradient method was used, the UAV-derived DEM achieved the highest accuracy in the mapping of the stream channel and defining the stream bank locations, with a MSE of 2.33 m (KGE = 82%), followed by LiDAR 6.0 (MSE = 5.27 and KGE = 70%) and LiDAR 1.2 (MSE = 7.87 m and KGE = 67%). The coarse-resolution DEM was unable to accurately predict this parameter and the error was significantly higher, at MSE = 26.76 m (KGE = 34%). The application of a filtering method to post-process the classified topographic model could significantly improve the prediction accuracy for LiDAR-based DEMs. The value of the MSE reduced from 7.87 to 3.33 (KGE = 80%) for LiDAR 1.2, and from 5.27 to 1.91 (KGE = 85%) for LiDAR 6.0. The value of MSE for the UAV-derived DEM was modestly reduced from 2.33 to 1.81 (KGE = 86%).

We found that the VSP method performed comparably with the Slope Gradient method in the mapping of the stream channel and determining the bank locations. Interestingly, we observed a decrease in accuracy among the higher-resolution DEMs tested. The LiDAR 1.2 was able to predict the stream bank with a MSE of 9.70 m (KGE = 67%), followed by

LiDAR 6.0 (MSE = 11.45 and KGE = 64%) and UAV-derived DEM (MSE = 15.12 and KGE = 53%). Similar to the Slope Gradient, the coarse-resolution DEM was unable to predict the stream boundaries and the MSE was 20.78 m (KGE = 28%).

The present work indicated that a UAV-derived DEM could be used to predict bank slope positions using the Slope Gradient as classifier for lower-order streams, with higher accuracy than airborne high point cloud density LiDAR. As opposed to LiDAR, UAVs have the capability of accurately defining the matrix of this ecosystem, from water surface, stream bank, riparian zone and uplands. However, highly densely vegetated areas could lead to errors due to the limitations of the photogrammetry method of the UAV in detecting bare ground under dense canopy.

References

Abood, S. A., Maclean, A. L., Mason, L. A. 2012. Modeling riparian zones utilizing DEMS and flood height data. Photogrammetric Engineering & Remote Sensing 78, 259-269.

Aguilar, F. J., Rivas, J. R., Nemmaoui, A., Peñalver, A., Aguilar, M. A. 2019. UAV-based digital terrain model generation under leaf-off conditions to support teak plantations inventories in tropical dry forests. A case of the coastal region of Ecuador. Sensors 19, 1934.

Alidoost, F., Arefi, H. 2017. Comparison of uas-based photogrammetry software for 3d point cloud generation: a survey over a historical site. isprs Annals of Photogrammetry, Remote Sensing & Spatial Information Sciences 4.

Apollonio, C., Petroselli, A., Cornelini, P., Manzari, V., Preti, F., Grimaldi, S. 2021. Riparian vegetation as a marker for bankfull and management discharge evaluation: The case study of Rio Torbido river basin (central Italy). Journal of Agricultural Engineering 52.

Ariza López, F. J., Atkinson Gordo, A. D. 2008. Analysis of some positional accuracy assessment methodologies. Journal of surveying Engineering 134, 45-54.

Biedenharn, D. S., Copeland, R. R., Thorne, C. R., Soar, P. J., Hey, R. D., Watson, C. C. 2000. Effective discharge calculation: A practical guide.

Bohn, C. 1986. Biological importance of streambank stability. Rangelands Archives 8, 55-56.

Brzank, A., Heipke, C. 2006. Classification of Lidar Data into water and land points in coastal areas. Int. Archives of Photogrammetry, Remote Sensing and Spatial Information Sciences 36, 197-202.

Buchanan, B., Falbo, K., Schneider, R., Easton, Z., Walter, M. 2013. Hydrological impact of roadside ditches in an agricultural watershed in Central New York: implications for non-point source pollutant transport. Hydrological processes 27, 2422-2437.

Buchanan, B., Fleming, M., Schneider, R., Richards, B., Archibald, J., Qiu, Z., Walter, M. 2014. Evaluating topographic wetness indices across central New York agricultural landscapes. Hydrology and Earth System Sciences 18, 3279-3299.

Caissie, D. 2006. The thermal regime of rivers: a review. Freshwater biology 51, 1389-1406.

Cartwright, J. M., Diehl, T. H. 2017. Automated identification of stream-channel geomorphic features from high-resolution digital elevation models in West Tennessee watersheds. US Geological Survey.

Chen, S., Johnson, F., Drummond, C., Glamore, W. 2020. A new method to improve the accuracy of remotely sensed data for wetland water balance estimates. Journal of Hydrology: Regional Studies 29, 100689.

Chorley, R., Dale, P. 1972. Cartographic problems in stream channel delineation. Cartography 7, 150-162.

Coverages, D. 1995. Landscape Drainage Analyses. Photogrammetric Engineering & Remote Sensing 61, 51'S-522.

Dietrich, W. E., Reiss, R., Hsu, M. L., Montgomery, D. R. 1995. A process-based model for colluvial soil depth and shallow landsliding using digital elevation data. Hydrological processes 9, 383-400.

Doody, D., Archbold, M., Foy, R., Flynn, R. 2012. Approaches to the implementation of the Water Framework Directive: targeting mitigation measures at critical source areas of diffuse phosphorus in Irish catchments. Journal of environmental management 93, 225-234.

Emanuel, K. 2013. Increased global tropical cyclone activity from global warming: Results of downscaling CMIP5 climate models. Proc. Natl. Acad. Sci. USA 110, 219-212.

Escobar Villanueva, J.R., Iglesias Martínez, L., Pérez Montiel, J.I. 2019. DEM generation from fixed-wing UAV imaging and LiDAR-derived ground control points for flood estimations. Sensors 19, 3205.

Evans, D., Gibson, C., Rossell, R. 2006. Sediment loads and sources in heavily modified Irish catchments: A move towards informed management strategies. Geomorphology 79, 93-113.

Fabian, A. J., Klenke, R., Truslow, P. 2020. Improving UAV-Based Target Geolocation Accuracy through Automatic Camera Parameter Discovery. AIAA Scitech 2020 Forum, p. 2201.

Fawcett, T. 2006. An introduction to ROC analysis. Pattern recognition letters 27, 861-874.

Fernández, D., Barquín, J., Álvarez-Cabria, M., Peñas, F. 2012. Quantifying the performance of automated GIS-based geomorphological approaches for riparian zone delineation using digital elevation models. Hydrology and Earth System Sciences 16, 3851-3862.

Fonstad, M. A., Dietrich, J. T., Courville, B. C., Jensen, J. L., Carbonneau, P. E. 2013. Topographic structure from motion: a new development in photogrammetric measurement. Earth surface processes and Landforms 38, 421-430.

Forman, R. 1995. Changing mosaics. Land Mosaics: The Ecology of Landscapes and Regions. Cambridge University Press, Cambridge, UK.

Forzieri, G., Castelli, F., Preti, F. 2012. Advances in remote sensing of hydraulic roughness. International journal of remote sensing 33, 630-654.

Garbrech, J., Mart, L. 1994. Grid size dependency of parameters extracted. Computers & Geosciences 20, 85-87.

Garner, G., Malcolm, I. A., Sadler, J. P., Hannah, D. M. 2014. What causes cooling water temperature gradients in a forested stream reach? Hydrology and Earth System Sciences 18, 5361-5376.

Gillin, C. P., Bailey, S. W., McGuire, K. J., Prisley, S.P. 2015. Evaluation of LiDAR-derived DEMs through terrain analysis and field comparison. Photogrammetric Engineering & Remote Sensing 81, 387-396.

Grau, J., Liang, K., Ogilvie, J., Arp, P., Li, S., Robertson, B., Meng, F.-R. 2021. Improved Accuracy of Riparian Zone Mapping Using Near Ground Unmanned Aerial Vehicle and Photogrammetry Method. Remote Sensing 13, 1997.

Gyasi-Agyei, Y., Willgoose, G., De Troch, F. P. 1995. Effects of vertical resolution and map scale of digital elevation models on geomorphological parameters used in hydrology. Hydrological Processes 9, 363-382.

Hancock, G. R. 2005. The use of digital elevation models in the identification and characterization of catchments over different grid scales. Hydrological Processes: An International Journal 19, 1727-1749.

Hashemi-Beni, L., Jones, J., Thompson, G., Johnson, C., Gebrehiwot, A. 2018. Challenges and opportunities for UAV-based digital elevation model generation for flood-risk management: A case of princeville, north carolina. Sensors 18, 3843.

Haupt, S. E., Pasini, A., Marzban, C. 2008. Artificial intelligence methods in the environmental sciences. Springer Science & Business Media.

Hengl, T. 2006. Finding the right pixel size. Computers & geosciences 32, 1283-1298.

Hsieh, W. W. 2009. Machine learning methods in the environmental sciences: Neural networks and kernels. Cambridge university press.

Islam, A. R. M. T., Talukdar, S., Mahato, S., Ziaul, S., Eibek, K. U., Akhter, S., Pham, Q. B., Mohammadi, B., Karimi, F., Linh, N. T. T. 2021. Machine learning algorithm-based risk assessment of riparian wetlands in Padma River Basin of Northwest Bangladesh. Environmental Science and Pollution Research, 1-22.

Jeziorska, J. 2019. UAS for wetland mapping and hydrological modeling. Remote Sensing 11, 1997.

Johansen, K., Grove, J., Denham, R., Phinn, S. R. 2013. Assessing stream bank condition using airborne LiDAR and high spatial resolution image data in temperate semirural areas in Victoria, Australia. Journal of Applied Remote Sensing 7, 073492.

Kalny, G., Laaha, G., Melcher, A., Trimmel, H., Weihs, P., Rauch, H. P. 2017. The influence of riparian vegetation shading on water temperature during low flow conditions in a medium sized river. Knowledge & Management of Aquatic Ecosystems, 5.

Kling, H., Fuchs, M., Paulin, M. 2012. Runoff conditions in the upper Danube basin under an ensemble of climate change scenarios. Journal of Hydrology 424, 264-277.

Krisanski, S., Taskhiri, M. S., Turner, P. 2020. Enhancing methods for under-canopy unmanned aircraft system based photogrammetry in complex forests for tree diameter measurement. Remote Sensing 12, 1652.

Kuo, W. L., Steenhuis, T. S., McCulloch, C. E., Mohler, C. L., Weinstein, D. A., DeGloria, S. D., Swaney, D. P. 1999. Effect of grid size on runoff and soil moisture for a variable-source-area hydrology model. Water Resources Research 35, 3419-3428.

Kuželka, K., Surový, P. 2018. Mapping forest structure using UAS inside flight capabilities. Sensors 18, 2245.

Lane, S., Reaney, S., Heathwaite, A. L. 2009. Representation of landscape hydrological connectivity using a topographically driven surface flow index. Water Resources Research 45.

Lanini, J., Sridhar, V., Sansone, A. L., LaMarche, J., Lettenmaier, D.P. 2004. REPLY TO DISCUSSION by John D. Fox, Jr. 1: "Prediction of Stream Temperature in Forested Watersheds" 2. JAWRA Journal of the American Water Resources Association 40, 1661-1662.

Lendzioch, T., Langhammer, J., Vlček, L., Minařík, R. 2021. Mapping the groundwater level and soil moisture of a montane peat bog using UAV monitoring and machine learning. Remote Sensing 13, 907.

Loučková, B. 2012. Vegetation–landform assemblages along selected rivers in the Czech Republic, a decade after a 500-year flood event. River Research and Applications 28, 1275-1288.

Magner, J. A., Vondracek, B., Brooks, K. N. 2008. Grazed riparian management and stream channel response in southeastern Minnesota (USA) streams. Environmental Management 42, 377-390.

Manfreda, S., McCabe, M. F., Miller, P. E., Lucas, R., Pajuelo Madrigal, V., Mallinis, G., Ben Dor, E., Helman, D., Estes, L., Ciraolo, G. 2018. On the use of unmanned aerial systems for environmental monitoring. Remote sensing 10, 641.

Marklund, L. 2009. Topographic control of groundwater flow. KTH.

Martínez-Santos, P., Aristizábal, H., Díaz-Alcaide, S., Gómez-Escalonilla, V. 2021. Predictive mapping of aquatic ecosystems by means of support vector machines and random forests. Journal of Hydrology 595, 126026.

Meng, F.-R., Castonguay, M., Ogilvie, J., Murphy, P., Arp, P. 2006. Developing a GIS-based flow-channel and wet areas mapping framework for precision forestry planning. Proceeding for IUFRO precision forestry symposium, pp. 43-55.

Morisawa, M. 1957. Accuracy of determination of stream lengths from topographic maps. Eos, Transactions American Geophysical Union 38, 86-88.

Murphy, P. N. C., Ogilvie, J., Arp, P. 2009. Topographic modelling of soil moisture conditions: a comparison and verification of two models. Eur. J. Soil Sci. 60, 94-109.

Naiman, R. J., Steel, E. A., West, S. D. 1999. Use of woody debris piles by birds and small mammals in a riparian corridor.

O'Callaghan, J. F., Mark, D.M. 1984. The extraction of drainage networks from digital elevation data. Computer vision, graphics, and image processing 28, 323-344.

Osbourne, J. D., Anderson, J. T., Spurgeon, A. B. 2005. Effects of habitat on small-mammal diversity and abundance in West Virginia. Wildlife Society Bulletin 33, 814-822.

Ostman, A. 1987. Accuracy estimation of digital elevation data banks. Photogrammetric Engineering and Remote Sensing 53, 425-430.

Peak, R. G., Thomson, F.R. 2006. Factors affecting avian species richness and density in riparian areas. The Journal of wildlife management 70, 173-179.

Petrasova, A., Mitasova, H., Petras, V., Jeziorska, J. 2017. Fusion of high-resolution DEMs for water flow modeling. Open Geospatial Data, Software and Standards 2, 1-8.

Pool, S., Vis, M., Seibert, J. 2018. Evaluating model performance: towards a non-parametric variant of the Kling-Gupta efficiency. Hydrological Sciences Journal 63, 1941-1953.

Poppenga, S. K., Worstell, B. B., Stoker, J. M., Greenlee, S. K. 2010. Using selective drainage methods to extract continuous surface flow from 1-meter lidar-derived digital elevation data. U. S. Geological Survey.

Rogers, S. R., Manning, I., Livingstone, W. 2020. Comparing the spatial accuracy of Digital Surface Models from four unoccupied aerial systems: Photogrammetry versus LiDAR. Remote Sensing 12, 2806.

Rykken, J. J., Moldenke, A. R., Olson, D. H. 2007. Headwater riparian forest-floor invertebrate communities associated with alternative forest management practices. Ecological Applications 17, 1168-1183.

Scannavino, J., Perez-Kuroki, A., Ghobakhlou, A., Sallis, P., Shanmuganathan, S., Cruvinel, P. 2011. Spatial variability on soil pH gradient: A case study in vineyards.

Schumann, G. J.-P., Muhlhausen, J., Andreadis, K.M. 2019. Rapid mapping of small-scale river-floodplain environments using UAV SfM supports classical theory. Remote Sensing 11, 982.

Shamshiri, R. R., Hameed, I.A., Balasundram, S. K., Ahmad, D., Weltzien, C., Yamin, M. 2018. Fundamental research on unmanned aerial vehicles to support precision agriculture in oil palm plantations. Agricultural Robots-Fundamentals and Application, 91-116.

Skarlatos, D., Vlachos, M. 2018. Vegetation removal from UAV derived DSMS, using combination of RGB and NIR imagery.

Smart, R., Soulsby, C., Cresser, M., Wade, A., Townend, J., Billett, M., Langan, S. 2001. Riparian zone influence on stream water chemistry at different spatial scales: a GIS-based modelling approach, an example for the Dee, NE Scotland. Science of the Total Environment 280, 173-193.

Sonneveld, M., Schoorl, J., Veldkamp, A. 2006. Mapping hydrological pathways of phosphorus transfer in apparently homogeneous landscapes using a high-resolution DEM. Geoderma 133, 32-42.

Sørensen, R., Seibert, J. 2007. Effects of DEM resolution on the calculation of topographical indices: TWI and its components. Journal of Hydrology 347, 79-89.

Tabacchi, E., Lambs, L., Guilloy, H., Planty-Tabacchi, A.M., Muller, E., Decamps, H. 2000. Impacts of riparian vegetation on hydrological processes. Hydrological processes 14, 2959-2976.

Thessen, A. 2016. Adoption of machine learning techniques in ecology and earth science. One Ecosystem 1, e8621.

Thirel, G., Andréassian, V., Perrin, C., Audouy, J.-N., Berthet, L., Edwards, P., Folton, N., Furusho, C., Kuentz, A., Lerat, J. 2015. Hydrology under change: an evaluation protocol to investigate how hydrological models deal with changing catchments. Hydrological Sciences Journal 60, 1184-1199.

Thomas, I., Jordan, P., Shine, O., Fenton, O., Mellander, P.-E., Dunlop, P., Murphy, P. N. C. 2017. Defining optimal DEM resolutions and point densities for modelling hydrologically sensitive areas in agricultural catchments dominated by microtopography. International Journal of Applied Earth Observation and Geoinformation 54, 38-52.

Tufekcioglu, M., Schultz, R. C., Isenhart, T. M., Kovar, J. L., Russell, J. R. 2020. Riparian land-use, stream morphology and streambank erosion within grazed pastures in Southern Iowa, USA: A catchment-wide perspective. Sustainability 12, 6461.

Wipfli, M. S. 1997. Terrestrial invertebrates as salmonid prey and nitrogen sources in streams: contrasting old-growth and young-growth riparian forests in southeastern Alaska, USA. canadian Journal of Fisheries and aquatic sciences 54, 1259-1269.

Wolf, R., Dewitt, A. 2000. Elements of Photogrammetry with Application in GIS, 3rd editrion. The university of Wisconsin, Madison.

Woodrow, K., Lindsay, J. B., Berg, A. A. 2016. Evaluating DEM conditioning techniques, elevation source data, and grid resolution for field-scale hydrological parameter extraction. Journal of Hydrology 540, 1022-1029.

Wu, H., Liu, C., Zhang, Y., Sun, W. 2009. Water feature extraction from aerial-image fused with airborne LIDAR data. 2009 Joint Urban Remote Sensing Event. IEEE, pp. 1-7.

Yao, H., Qin, R., Chen, X. 2019. Unmanned aerial vehicle for remote sensing applications—A review. Remote Sensing 11, 1443.

Zaimes, G. N., Tufekcioglu, M., Schultz, R. C. 2019. Riparian land-use impacts on stream bank and gully erosion in agricultural watersheds: What we have learned. Water 11, 1343.

Zhang, Q., Qin, R., Huang, X., Fang, Y., Liu, L. 2015. Classification of ultra-high resolution orthophotos combined with DSM using a dual morphological top hat profile. Remote Sensing 7, 16422-16440.

Zhang, W., Montgomery, D.R. 1994. Digital elevation model grid size, landscape representation, and hydrologic simulations. Water resources research 30, 1019-1028.

CHAPTER 4: Improved Accuracy of Riparian Zone Mapping Using Near Ground Unmanned Aerial Vehicle and Photogrammetry Method

Abstract: In agriculture-dominant watersheds, riparian ecosystems provide a wide array of benefits such as reducing soil erosion, filtering chemical compounds, and retaining sediments. Traditionally, the boundaries of riparian zones could be estimated from Digital Elevation Models (DEMs) or field surveys. In this study, we used an Unmanned Aerial Vehicle (UAV) and photogrammetry method to map the boundaries of riparian zones. We first obtained the 3D digital surface model with a UAV. We applied the Vertical Distance to Channel Network (VDTCN) as a classifier to delineate the boundaries of the riparian area in an agricultural watershed. The same method was also used with a low-resolution DEM obtained with traditional photogrammetry and two more LiDAR-derived DEMs, and the results of different methods were compared. Results indicated that higher resolution UAV-derived DEM achieved a high agreement with the field-measured riparian zone. The accuracy achieved (Kappa Coefficient, KC = 63%) with the UAV-derived DEM was comparable with high-resolution LiDAR-derived DEMs and significantly higher than the prediction accuracy based on traditional low-resolution DEMs obtained with high altitude aerial photos (KC = 25%). We also found that the presence of a dense herbaceous layer on the ground could cause errors in riparian zone delineation with VDTCN for both low altitude UAV and LiDAR data. Nevertheless, the study indicated that using the VDTCN as a classifier combined with a UAV-derived DEM is a suitable approach for mapping riparian zones and can be used for precision agriculture and environmental protection over agricultural landscapes.

Keywords: Riparian Zone; Mapping; DEM; UAV; LiDAR; VDTCN.

Grau, J.; Liang, K.; Ogilvie, J.; Arp, P.; Li, S.; Robertson, B.; Meng, F.-R. Improved Accuracy of Riparian Zone Mapping Using Near Ground Unmanned Aerial Vehicle and Photogrammetry Method. *Remote Sens.* **2021**, *13*, 1997. https://doi.org/10.3390/rs13101997

4. 1. Introduction

Riparian zones are vegetated areas adjacent to natural water bodies with distinctive plant communities different from their upland surroundings, strongly shaped and affected by geomorphic processes occurring in the area (Naiman & Decamps, 1997; Swanson *et al*., 1988; Hill & Cardaci, 2004). The critical location of riparian zones within watersheds allows them to intercept pollutants received from uplands and prevent these pollutants from transferring downstream to estuarine systems (Cooper *et al.,* 1987; Meehan *et al*., 1977; Peterson *et al*., 2001; Swanson, *et al*., 1982). The volume of water, as well as its pathways moving through the riparian zones, are fundamental for understanding nutrient removal and retention (Likens, 2010).

From a resource management perspective, valley bottoms are often focal points of conflict between human land uses and the protection of vulnerable riparian ecotones. Harvest operations and agriculture practices can lead to deleterious effects on the stream channel. The removal of streamside vegetation not only compromises the stabilization effects of roots upon the bank soil but also reduces the hydraulic roughness of the bank, which could lead to a rise in flow velocities (Sedell & Beschta, 1991) and thus accelerate channel erosion and increase sediment input into streams (Johansen *et al*., 2007; Rivenbark & Jackson, 2004). In addition, failing riparian ecosystems cannot buffer streams against sediment and pollutants loading from uplands.

The effectiveness of riparian conservation depends largely on the accurate delineation of the riparian zone. Traditionally, riparian zone delineations have been concentrated on field measurements over a few hundred meters (Johansen *et al.,* 2007; Werren & Arthington, 2002). This task could be time-consuming and labor-intensive to evaluate a

large area such as an entire catchment or a long river corridor, particularly in remote locations. One way to reduce the time and costs is to sample representative sections. However, the selection of representative sites can suffer from subjectivity and be limited by accessibility and safety, which could introduce large uncertainties for the full characterization of a riparian zone (Fu *et al.*, 2017).

Remote sensing techniques have been used to map riparian zones due to their advantages in spatial extensiveness, non-invasiveness, and repeatability (Congalton *et al.*, 2002; Johansen & Phinn, 2006). Riparian zones can be mapped by predicting the interface between permanently wet or wetter areas due to position in the landscape using terrain attributes, such as slope gradient and elevation (Chaplot, *et al.*, 2000; Ilhardt *et al.*, 2000), and/or the presence of a permanent or fluctuating water table near the soil surface, terrain wetness index and local drainage patterns, or proximity to a watercourse. Concurrently, these factors are prone to develop a specific soil type, describing the spatial variation and distribution of saturated soils in a particular landscape.

Researchers and conservationists have attempted to map the complex soil drainage classes and riparian ecosystems using online geospatial datasets (Gallant & Dowling, 2003; Murphy *et al*., 2009; Abood *et al*., 2012). This often means the usage of coarser-resolution spatial data collected from traditional photogrammetry, offering inaccurate results when attempting to represent lower-order streams and small watersheds (Vaze *et al*., 2010; Johansen *et al.*, 2013). Conventional low-resolution DEMs are also unable to capture topographic variations in detail. For example, Murphy et al. (Murphy *et al.*, 2009) concluded that the final map imperfections and limitations were probably the result of the poorer resolution and lower initial elevation point density of these topographic models.

Therefore, for ecosystem protection, restoration, and management at smaller scales, more accurate and detailed DEMs have become necessary (Smith *et al.*, 2008; Holmes *et al.*, 2010).

Light Detection and Ranging (LiDAR) technology can collect high density elevation points, which has been used to generate DEMs with more topographic detail and lead to improved hydrological modeling accuracy. Buchanan *et al.* (2014) concluded that using a high-resolution DEM (3 m) provided better results than using a 10 m resolution DEM when estimating soil moisture conditions using a topographic wetness index. The spatial resolution and data format have a significant impact on predicting the parameters mentioned to represent the boundaries of ecotones with different soil moisture regimes.

Bock and Köthe (2008) postulated that soil characteristics influenced by groundwater hydrological processes could be mapped according to the Vertical Distance to Channel Network (VDTCN), a topographic index that reflects the average groundwater table depth based on topographic positions and the distance to existing flow channels. A similar method was used to investigate the spatial distribution of soil properties in relation to micro-topography using a 1m resolution DEM (Kokulan *et al.*, 2018), or 25 m DEM (Malone *et al.*, 2018).

Recent technological advances, as well as the increasing availability of Unmanned Aerial Vehicles (UAVs) with multimodal sensors, coupled with improved photogrammetry and computer algorithms have led to dramatic improvements in the collection and processing of terrain data using photogrammetry. This approach can produce high resolution Digital Surface Models (DSMs) with high quality and makes UAVs a cost-effective alternative to Airborne Laser Scanning (ALS) (Carrivick *et al.*, 2013; Fonstad *et*

al., 2013; Escobar Villanueva *et al*., 2019). Jeziorska (2019) assessed the suitability of DEMs obtained from UAV photogrammetry for overland flow simulations in the context of precision agriculture applications. They concluded that UAV-based data were most suitable for overland flow predictions compared with other methods including LiDAR data. Rahman and others (2017) combined orthophotography and photogrammetric point clouds acquired from UAVs to map peatland groundwater table in the Peace River area (Alberta, Canada). By identifying pockets of surface water, they obtained a direct measurement of groundwater level (GWL) in locations where it was visible and generated continuous-surface estimates over large areas through interpolation (Rahman *et al.*, 2017).

The general objective of this study was to test the feasibility of using a near ground UAV and photogrammetry method for riparian zone mapping. Specific objectives included: 1) Collecting high resolution DEM data using a UAV and photogrammetry method; 2) Using high resolution DEMs to classify riparian zones in agricultural landscapes with Vertical Distance to Channel Network; 3) Estimating optimal parameters for riparian zone delineation with DEM; 4) Assessing the accuracy of riparian zone delineation with different DEM resolutions and data sources.

4. 2. Materials and Methods

4.2.1. Study Area

The study area is located on the Ridge Brook, within the Canaan River Watershed, near Havelock in the province of New Brunswick, Canada (46°01'29.0"N, 65°18'32.5"W; Figure 4.1). The Ridge Brook sub-watershed covers an area of 7020 ha. Land use within the watershed is primarily agriculture, with small scale limestone extraction operation near the small town of Havelock.

The farm where the study was conducted grows a mix crops, including grasses, barley, and legumes. The soil type has been classified as Luvisolic, which has a forest mull Ah, and a Bt or Btg horizons. The Ah horizon is the top mineral soil horizon enriched with organic matter. While the Bt horizon is an illuvial horizon enriched with silicate clay, normally formed below an eluvial horizon, the "Btg" horizon indicates poor drainage and periodic reduction due to significant amount of clay accumulation. Therefore, gleying (anoxic) conditions are likely to occur within 50 cm of the mineral surface, and these features can be found particularly in depressions with poorly drained sites coupled with Regosolic soils. Soils in certain areas lack a distinguished "B" horizon of at least 5 cm, probably due to recent alluvium, or colluvium on slopes, in which case the nature of the material can be purely quartz sand. These types of soils are often classified as rapidly to imperfectly drained (Canadian soil classification system). The pH detected in the field is close to 5.5. The upstream riparian area adjacent to the farm is surrounded by two sections of planted conifer species, red pine (*Pinus resinosa*) and Jack pine (*Pinus banksiana*). These planted species may increase the acidity of the soil in the natural riparian forest, located in the southernmost part of the study area.

Prior to 2007, cattle had access to the stream as a watering source and used the riparian zone for grazing. These cattle activities caused some impacts on the structural integrity of the stream banks and the growth of riparian vegetation, which led to a widening of the channel and increased sedimentation. In 2007, a bioengineered buffer zone—that currently covers approximately one-third of the stream path through the farm—was implemented to increase riparian health, to add stability to the stream, and to recover the riparian zone to a more natural condition. With the help of a bioengineered buffer zone protection project,

the vegetation coverage increased as well as the bank stability, and reduced eutrophication due to accelerating the water velocity. However, due to the lack of an off-stream watering system for cattle and absence of a dedicated livestock crossing, vegetation is still removed from grazing activities in the areas outside of the bioengineered buffer. Cattle activities have also caused soil compaction along the fenced area on the eastern side of the stream.

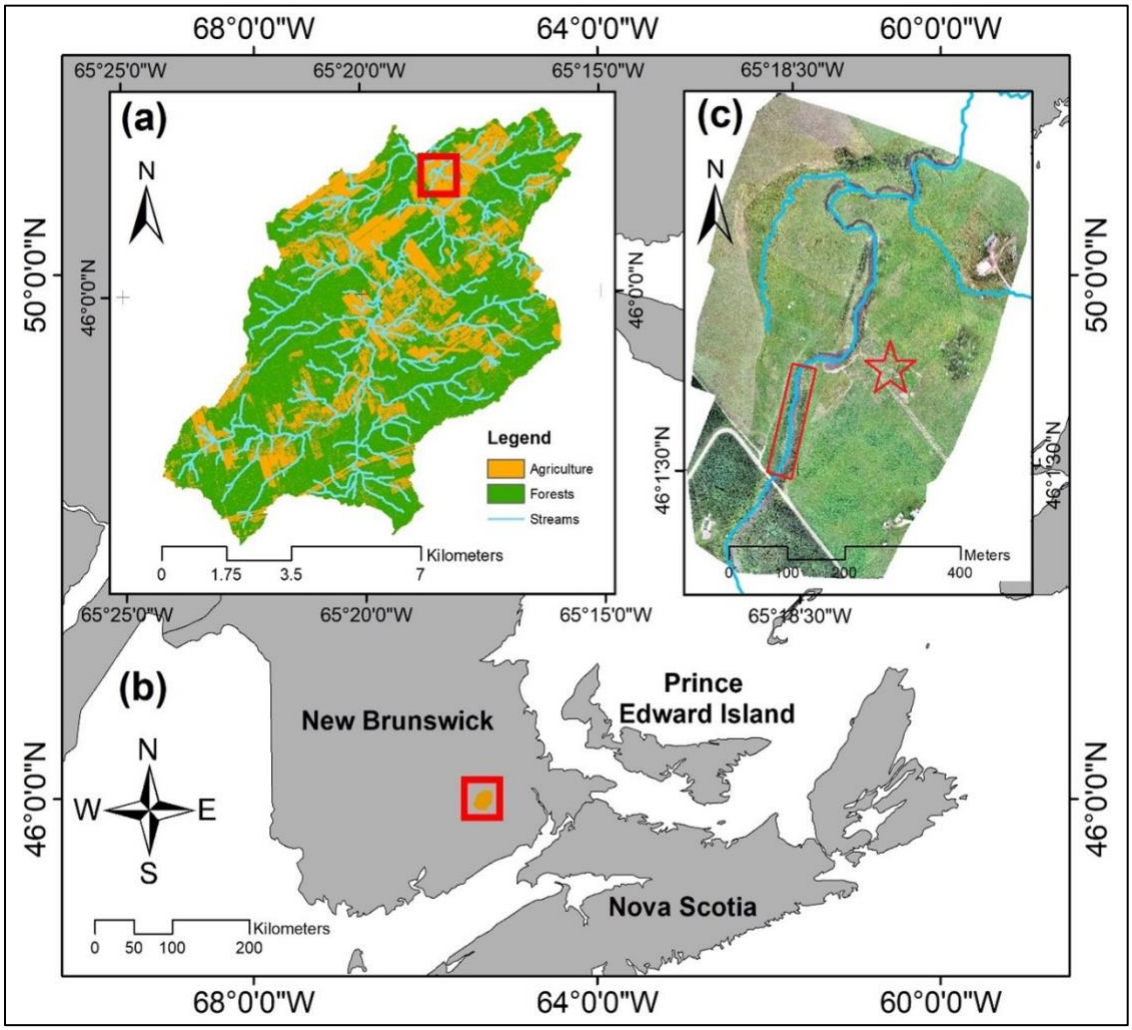

Figure 4.1. Location of study area (Hicksville settlement, Havelock, NB); (a) The Ridge Brook subcatchment; (b) the location of the watershed in New Brunswick; (c) the location of the study area within the watershed. The red rectangle in (c) covers the bioengineered buffer area. The star point is the area affected by intense cattle grazing and cattle resting. The stream follows South to North direction.

4.2.2. Online Available Data Interpolation

The traditional coarse resolution provincial DEM was obtained from the Service New Brunswick (SNB) geographic information source (http://www.snb.ca/geonb1/e/DC/DEM.asp). The accuracy of a single elevation point was approximately 2.5 m and the spacing between the elevation points was of nearly 70 m on average, with increased density in more complex terrain area. We generated a DEM at a 2 m cell size using the Inverted Distance Weighted (IDW). This DEM was hydrologically corrected in ArcMap 10.5 with field-mapped open drainage channel network ("burn" DEM) within the Service New Brunswick Geospatial Database.

The LiDAR DEMs were obtained from the Service New Brunswick Geospatial Database. The point cloud density of the LiDAR dataset collected in 2013 was 1.2 points m^{-2}. The DEM based on the 2013 LiDAR data had a horizontal accuracy of 0.3 m and the vertical accuracy of 0.133 m at 95% confidence level. The point cloud density of LiDAR dataset collected in 2018 was 6 points m^{-2}. The horizontal accuracy was 0.20 m, and vertical accuracy was RMSE Z = 10.5 cm, equating to +/− 20.6 cm at a 95% confidence level. The DEM raster was generated with Natural Neighbors interpolation with a 30 cm resolution.

4.2.3. UAV and Sensor Description

The Unmanned Aerial Vehicle (UAV) used in this study was a DJI Phantom 4 Pro (Da-Jiang Innovations, SZ DJI Technology Co., LTD; Figure 4.2). This UAV was chosen due to its recognized camera stability which is considered to be a key factor for precision agriculture and forestry purposes (Krisanski, *et al.*, 2020; Kuželka & Surový, 2018; Shamshiri *et al.,* 2018). The Phantom 4 Pro is a vertical takeoff and landing aircraft with

total payload of 1388 g, battery and propellers included. This UAV uses four 2312S Brushless motors powered by a 15.2 V battery with a cruising speed of 72.0 km h^{-1} (s-mode) and a maximum climb speed of 6m s^{-1}. The maximum service ceiling is 6000 m asl and the maximum transmission range with no obstruction and free of interference is up to 7km. The maximum payload is 1.02 lbs. The maximum wind speed resistance is up to 10.0m s^{-1}. The reported maximum flight time with a single battery is 30 minutes, with a practical flying time of around 25 minutes based on our tests depending on wind speed and temperature (<10 km h^{-1}; > 4 °C). We planned the flight durations within 20 minutes, at a flight speed of 7 m s^{-1}.

The onboard camera is 1 inch complementary metal oxide semiconductor (CMOS) with 20 M effective pixels (5472 × 3648). The lens has a field of view (FOV) of 84° and the focal length is 8.8 mm/24 mm (35 mm format equivalent) f/2.8 – f/11 auto focus at 1 m–∞. During the flight, the sensor registers either vertical images captured at Nadir angle (for 2D maps), or the camera can be tilted (off-Nadir angles) up to 90 degrees for 3D Digital Surface Model (DSM) reconstructions. The image trigger can be activated automatically in autopilot flight mode, with simultaneous timestamps and automatic recording of GPS locations due to its multiple satellite position navigation system (GPS and GLONASS). The reported vertical hover accuracy range is 0.5 m with GPS positioning and the horizontal hover accuracy is 1.5 m with GPS positioning. Images and metadata are automatically stored with a 64 GB Lexar high performance 633x MicroSDXC UHS-I Secure Digial Card (SD-Card).

Figure 4. The DJI Phantom 4 Pro set up in the field.

Rogers *et al.* (2020) tested different UAVs (DJI Inspire 1, DJI Mavic Pro, and DJI Matrice 210) including DJI Phantom 4 Pro and compared the accuracy of the UAV-derived DSMs for each UAV using a DSM created from Light Detection and Ranging (LiDAR) mounted on a DJI Matrice 600 Pro. They found that the DJI Phantom 4 pro provided higher accuracy in four of the six land covers tested (vines, bare soil, forest, and mowed grass). Among the drones tested, the DJI Phantom 4 Pro performed the best due to the higher resolution sensor (20 MP), which provides finer Ground Sample Distances (GSDs) and greater density in output point clouds. They also ranked the UAVs used in different categories, including maximum flight time, number of batteries, dimensions, resolution, and weight. The Phantom 4 Pro was considered to be the best balance between size and sensor resolution, which makes this a versatile drone widely used by professional users (Rogers *et al.*, 2020).

4.2.4. UAV Data Collection

Flights and image acquisition were scheduled on days when the temperature was above 5 °C and the wind speed was low (<10 km h^{-1}). We tried capturing images under overcast or partially overcast days to minimize shading effects. We acquired near-ground UAV

aerial data in 2018 and 2019 in three different seasons, including early Spring, Summer, and Fall (8 May, 20 August, and 17 November of 2018, and 13 May, 28 August, and 25 October of 2019). The main consideration of season selection was to map different vegetation growth stages and streamflow conditions throughout the year. The early spring provided field conditions with herbaceous vegetation that was still snow-flattened but without snow cover on the ground. This can reduce the elevation error caused by the height of streamside vegetation. Deciduous tree species were also still in leaf-off conditions. These data can be used to visually identify the starting points of ephemeral, intermittent, or permanent flows and help in determining the threshold parameter of streams for flow accumulation data. The stream initiation parameter is an important parameter for the mapping of lower-order stream network-based DEM, and it is difficult to determine due to upland variations in vegetation cover and type, topography, sediment, and soil hydraulic properties across regions due to variations in weather and climate (White *et al.*, 2012; Elmore *et al.*, 2013).

Six ground control markers (square targets of 1.44m^2) were equally positioned across the site and at the boundaries of the UAV study area, including next to the watercourse at different elevations (Figure 4.3). A ground control point (GCP) of each target's corners was recorded with a Trimble Geoexplorer 6000 Series handheld GPS (10 cm of horizontal accuracy according to the GPS manual) to mark the positions of the panels with geometrical precision for georeferencing accuracy. Each position was registered using the real-time kinematics (RTK) mode to register the location of each target (checkpoint). To do so, the GPS was placed in a static position for 30 seconds. The precision observed in

the GPS device during the geolocation acquisition was 10 cm for each record, with a minimum of 16 satellites available.

During each flight, we acquired 1027 images following pre-planned and evenly spaced parallel flight paths in two directions to form a squared grid using Pix4D app (Pix4D Inc). The side and frontal overlap rate was 80%. The average flight speed was 7 m s^{-1} at near ground elevation (80 m), with the camera set at Nadir angle for 2D mapping. The captured images were processed with the Structure from Motion (SfM) algorithm to generate geo-rectified orthomosaic images using Pix4D 4.4 (Pix4D Inc). The latitude, longitude, and altitude (WGS84 projection) in metadata were used to position the aerial photos first. Common points from different images in the overlap areas were used as keypoints to build a 3D projected point through aerotriangulation (Wolf & Dewitt, 2000). In order to improve the software image stitching, 10 manual tie points (mtps) were added in the planted forest area upstream.

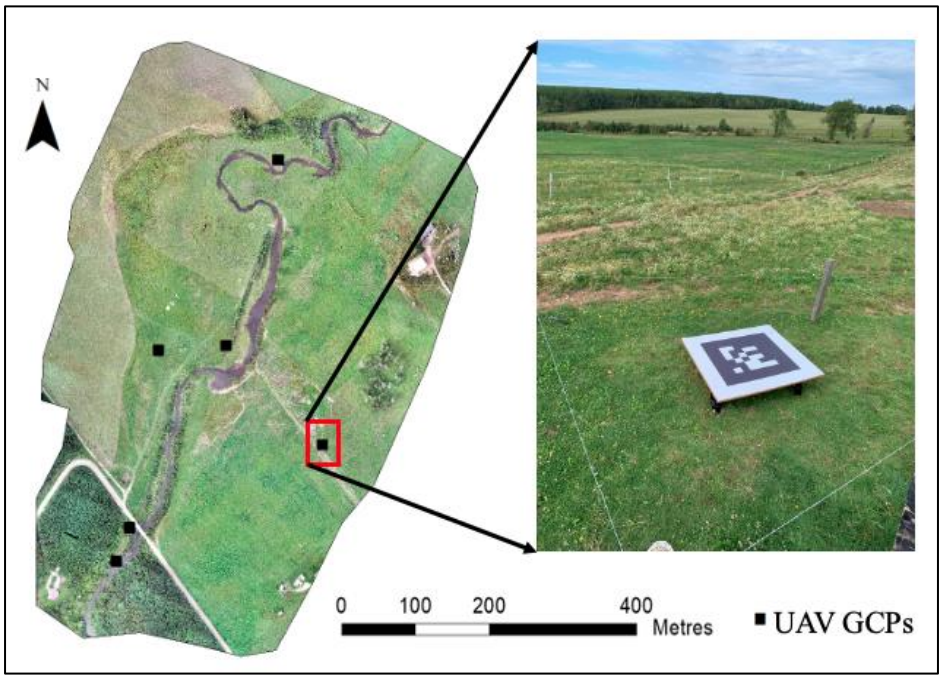

Figure 5. Distribution of the GCPs in the study area.

4.2.5. Point Cloud Cleaning

We observed that 3D information on water surfaces had a large error, potentially caused by floating objects moving on the water's surface as well as light/illumination changes between images captured at different times (i.e., reflection, absorption, and refraction). The camera could also penetrate the water surface to identify the stream bed in some cases but not in others, and this caused large errors or noise in surface elevation. Points classified as water were removed in order to reduce the uncertainties for the estimation of the stream channel, the triangulation, and the effects on the quality of the DEM (Beni *et al.*, 2018). In addition, misclassification for ground or vegetation was manually corrected to avoid errors in the surface model (Poppenga *et al.*, 2010). The resulting point cloud had an average density of 833 points m^{-2}, and it was further interpolated at 0.3 m resolution, using the LAStools commercial software suite (Martin Isenburg, LAStools -efficient tools for LiDAR processing).

4.2.6. Stream Network and Flow Initiation Thresholds

The spatial hydrology tools of ArcGIS (10.5) were used to generate stream networks. For the traditional coarse resolution DEM, the existing stream network was used to correct the flow patterns in the flow accumulation raster (Zhang & Montgomery, 1994). This is necessary because a coarse-resolution DEM could not capture and represent the topographic features, such as small streams, due to interpolation errors (Hancock, 2005). Because of their greater initial point density, LiDAR and UAV DEMs do not require stream correction. Local depressions or sinks were removed with a fill function to create a depressionless DEM. The flow direction rasters were produced with a D8 algorithm (O'Callaghan & Mark, 1984). The flow accumulation raster was derived from the flow

direction raster. The flow accumulation raster was used to derive low order stream network according to the predefined flow initiation threshold. The flow initiation threshold was used as a parameter to optimize riparian zone mapping accuracy.

4.2.7. Functional Riparian Prediction

The Vertical Distance to Channel Network (VDTCN) was used as a classifier for riparian zones. The Vertical Distance to Channel Network parameter measures the relative elevation difference between a point of interest to the elevation of the channel network. The parameter algorithm has been successful in inferring groundwater levels, aiding soil mapping processes, and predicting soil textures (Bock & Köthe, 2008). More specifically, the tool uses an algorithm that consists of two major steps: 1) It interpolates the elevation of streams and creates a base level elevation of the stream network; 2) the neighboring stream cells for points of interest are determined iteratively using the distance from the center of the cell as a weighting factor. The final VDTCN is calculated by subtracting this base level from the re-calculated DEM neighboring elevations (Bock & Köthe, 2008).

4.2.8. Field Validation

The indicator of vegetation species adapted to poorly drained and wetted soils could also be used to identify riparian areas because these vegetation species rely on access to groundwater (Brander & Schuyt, 2004; Wilson *et al.*, 2015). In this study, sedges (*Carex* sp), rushes (*Juncus* sp), grasses (*Panicum* sp or *Agropyron* sp), blue flag iris (*Iris versicolor*), and cattails (*Typha* sp) were used as indicators species to map the riparian zone since they are known to grow in partially submerged and water-logged riparian soils. Sites

with over 50% visual cover (Londo, 1976) of target species were included within the riparian field delineation.

In areas absence of hydrophytic vegetation, soil with signs of groundwater table fluctuations was used to identify riparian areas (Bouma, 1983). Fifty-four soil pits were dug in transects of 5 m increments from the highly dense riparian vegetation boundaries. The soil indicators include signs of anaerobic conditions, such as the existence of microbially reduced ferrous (Fe^{2+}) from ferric iron (Fe^{3+}), the presence of organic carbon, and grey matrix soil color caused by elluviation. In addition, redoximorphic features, such as mottling and precipitation of manganese, were also used to identify the soils exposed to periodic or prolonged periods of saturation, typical in riparian zones (Shaw *et al.*, 2002). A field survey of soil and vegetation indicators was used to register the boundary of the functional riparian zone using a handheld GPS (Trimble Geoexplorer 6000 Series). Figure 4.4 details the flowchart of the methodology.

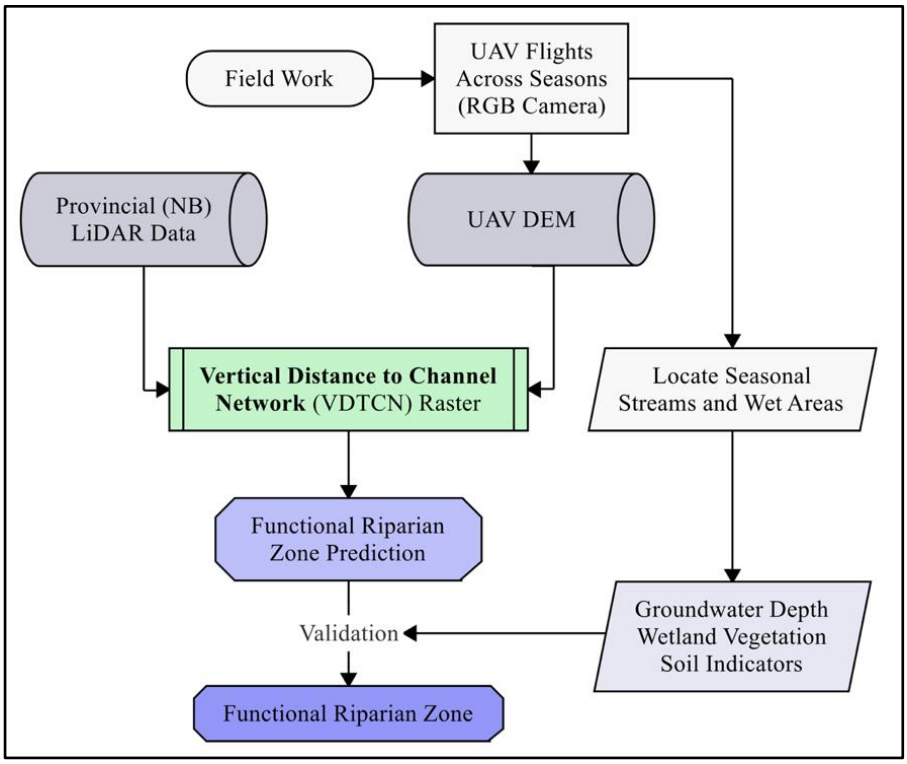

Figure 4.4. Flow chart of the methodology for delineating functional riparian zones and flow paths.

4.2.9. Statistical Analysis

The quantitative consistency and correctness achieved by VDTCN with each DEM used as a source, compared with field survey, was calculated using the Kappa Index (Congalton & Mead, 1983).

4. 3. Results

4.3.1. Interpolated DEMs and Geolocation Precision

The interpolated DEMs from point clouds of different sources are shown in Figure 4.5. As shown, the coarse DEM was visually different compared to the three high-resolution DEMs and could not represent the minor topographic features, including streams. No relevant elevation differences were observed between the LiDAR 1.2 and LiDAR 6.0-

derived DEMs. The height values shown for the UAV-derived DEM were practically equal to the LiDAR values. On average, we obtained 53,566 keypoints per image and a minimum of five images overlapping every pixel. Since the Phantom 4 Pro is capable of automatically recording GPS locations, we used this product as the relative geolocation. As reported by Fabian *et al.* (2020), adverse factors, such as lens distortion, GPS position error, aircraft attitude uncertainty, and errors in the time domain can lead to the decreased accuracy in the relative UAV map geolocation. Therefore, we corrected the overall geolocation using the target coordinates, as checkpoints, acquired with handheld GPS as relative accuracy. The elevation Root Mean Squared Error (RMSE) for these GCPs was 0.075 meters, and **t**he horizontal RMSE for longitude and latitude were 0.078 and 0.066 meters, respectively. These results indicate high precision between the measured coordinates (GCPs registered in the field) compared with the software-calculated position.

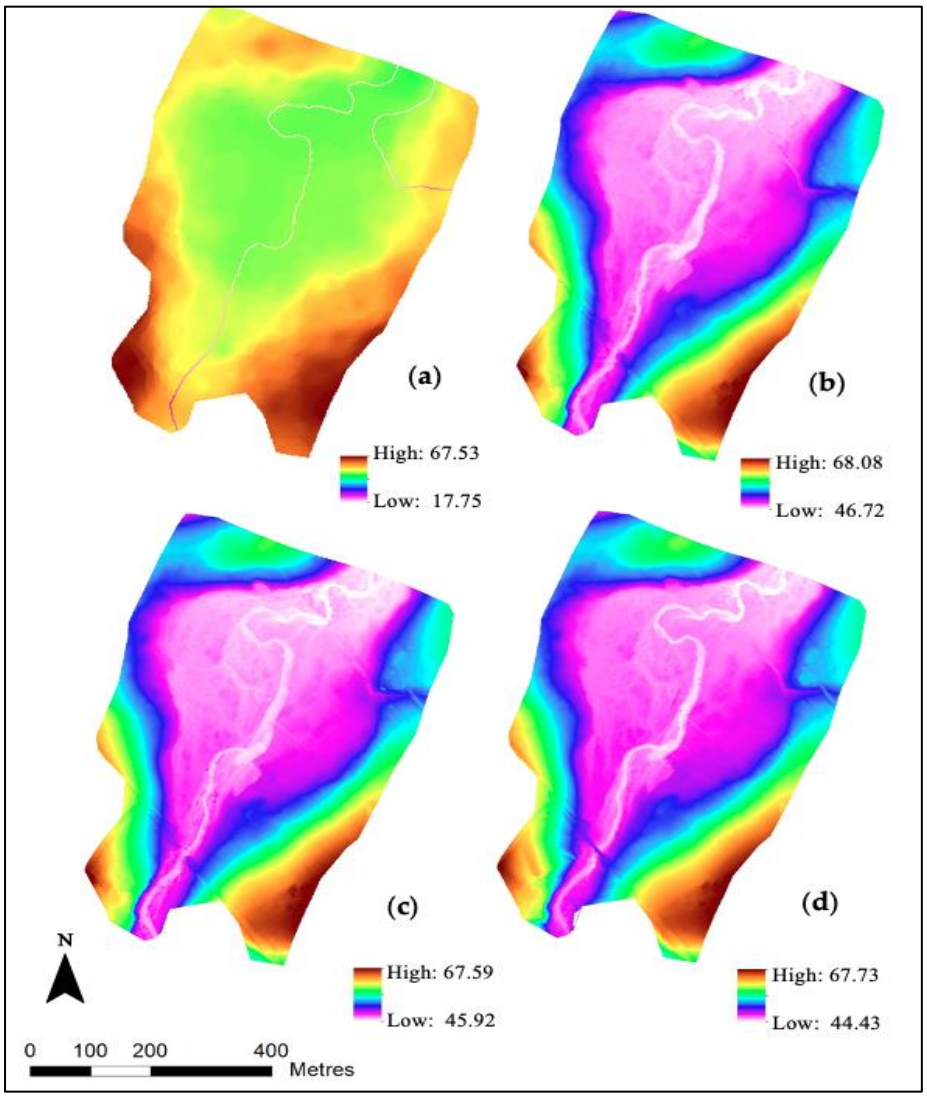

Figure 6. Interpolated DEMs with point clouds from different data sources: (a) coarse resolution ("burn" DEM); (b) LiDAR 1.2; (c) LiDAR 6.0; (d) UAV. Elevation values are displayed in meters. The difference in the lowest value registered in (a) is due to imprinting field-mapped open drainage channel network to create the "burn" DEM.

4.3.2. The Optimal Parameter for Riparian Zone Delineation

Since the traditional coarse resolution, DEM was the most available data; we optimized the flow initiation and VDTCN threshold parameters with this topographic model first. The flow network and VDTCN based on coarse resolution DEM with different flow initiation thresholds are shown in Figure 4.6. The UAV images obtained in Spring, Summer, and Fall are shown in Figure 4.7. As shown, the length of flow lines increases

with decreased flow initiation thresholds (Figure 4.6a–c). To do so, we maximized the coinciding areas and minimized errors of commission (false positive) and omission (false negative), testing different minimum flow initiation and VDTCN thresholds (Figure 4.6). Higher VDTCN thresholds included more areas classified as wet (Figure 4.6d–f).

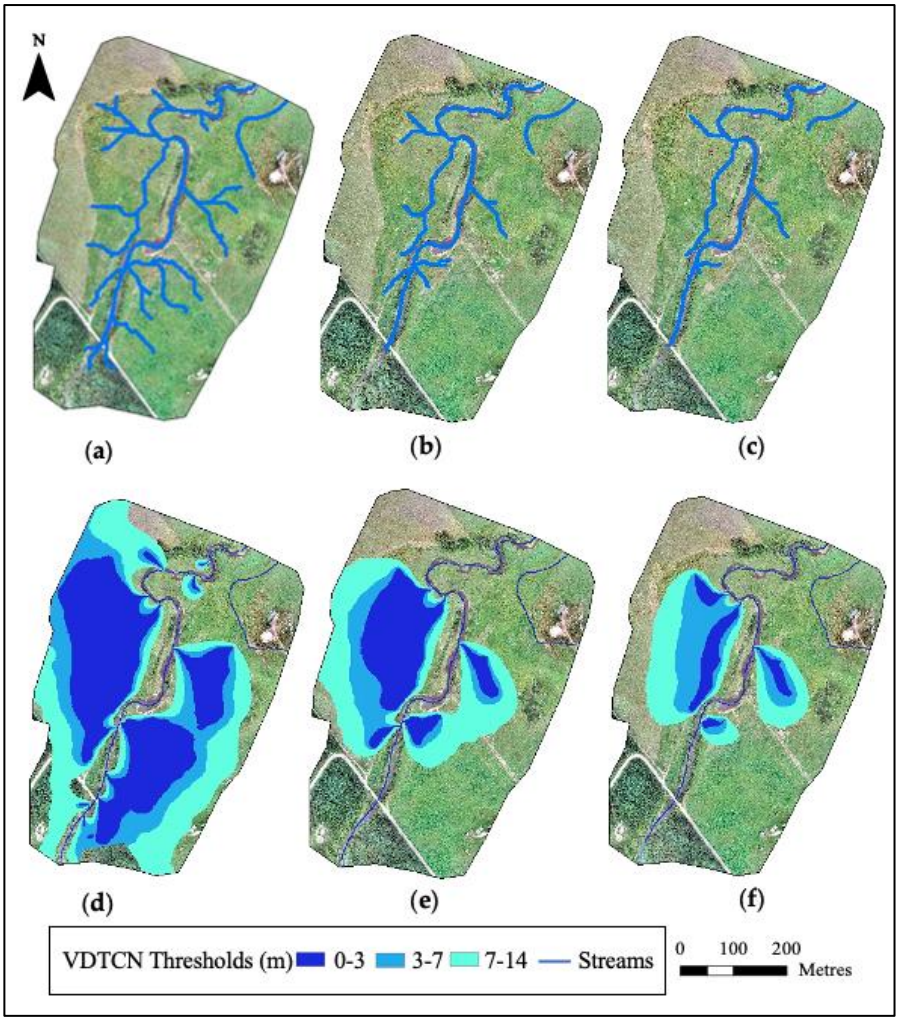

Figure 7. Stream network (Top Panels) and VDTCN (Lower Panels) with different minimum flow initiation thresholds using the coarse resolution DEM as a source: (a,d) 0.5 hectares; (b,e) 1 hectare; (c,f) 1.5 hectares. The different colors represent different VDTCN thresholds, expressed in meters.

We found that the optimal flow initiation threshold was 1.5 ha, and the optimal VDTCN threshold was 14.2m. Afterward, we applied these optimized parameters found in the

coarse resolution DEM to all other DEMs to predict the extents of riparian zones using LiDAR- and UAV-derived DEMs.

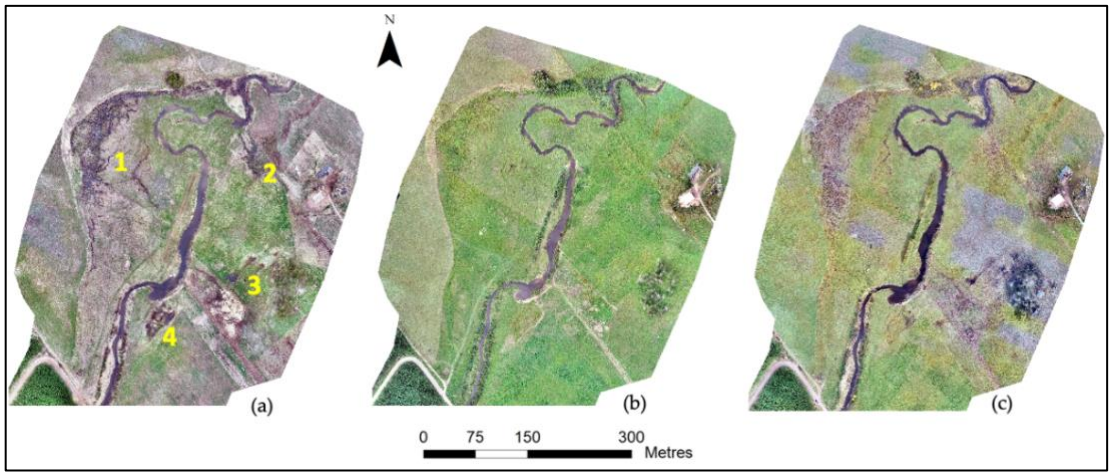

Figure 8. UAV images obtained in (a) Spring, (b) late Summer, and (c) Fall. As can be seen, (a) displays better detail of wet areas. The numbers in (a) represent the different functional riparian areas measured in the field.

The riparian zone prediction accuracies measured as Kappa Coefficients (KC) are shown in Table 4–1. The Kappa Coefficent was 0.25 for the coarse-resolution DEM. When the optimal parameters derived from the coarse resolution DEM were directly applied to high-resolution DEMs, the KC were 0.04, 0.03, and 0.03 for LiDAR 1.2, LiDAR 6.0, and UAV DEMs, respectively. The coarse resolution DEM achieved a higher prediction accuracy than higher resolution DEMs. These results indicated that optimal parameters obtained with coarse resolution DEM could not be directly used to classify riparian zones with high-resolution DEMs.

The flow network and VDTCN based on high-resolution DEMs with different flow initiation thresholds are shown in Figure 4.8. The accuracies of riparian zone prediction with different DEMs and different flow initiations are shown in Table 1. For the LiDAR1.2 DEM, we found the optimal flow initiation threshold was 0.75 ha, and the optimal VDTCN

threshold was 0.4 m, and we achieved a KC of 0.63. If the optimal parameters found for LiDAR1.2 DEM were used for LiDAR6.0 and UAV DEMs, the KC were 0.63 and 0.56, respectively (Table 4–1).

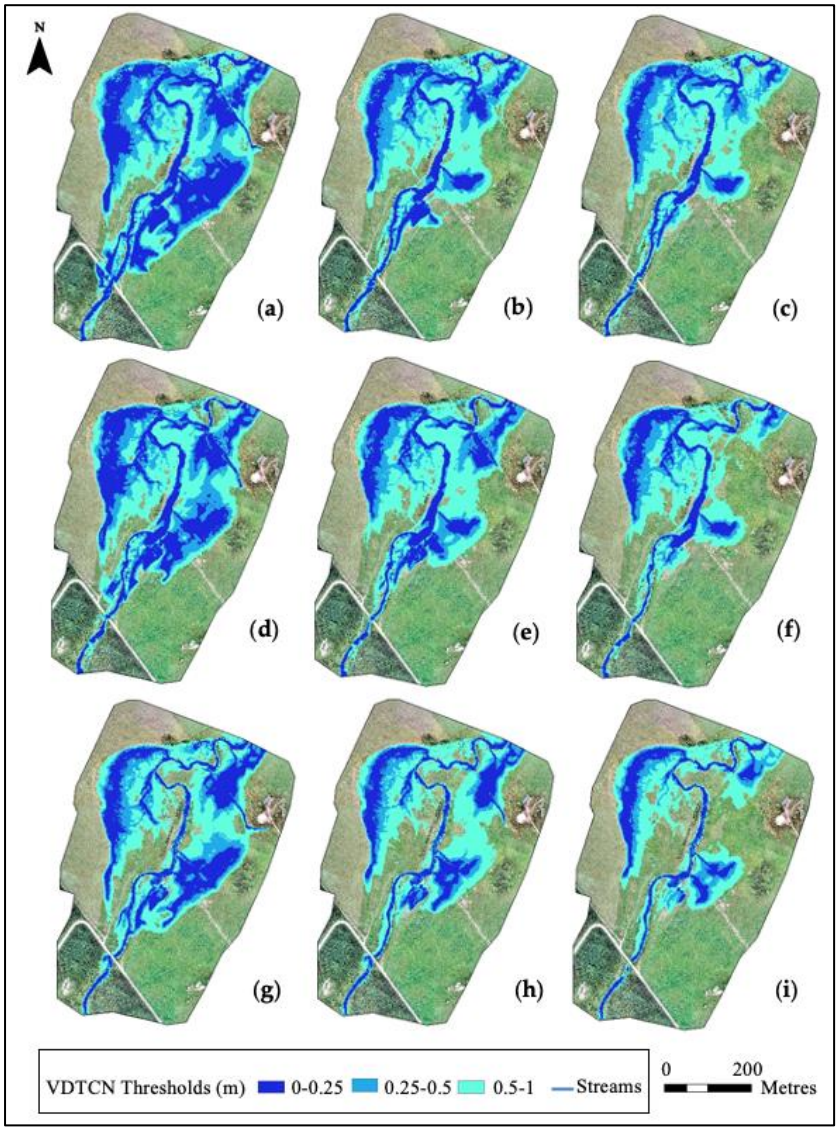

Figure 4.8. The VDTCN maps derived from different high-resolution DEMs using different flow initiation thresholds; from left to right, minimum flow initiation: 0.5 hectares; 1.0 and 1.5 ha, respectively. Figures (a–c) show the VDTCN using the LIDAR1.2 as a source. Figures (d–f) show the VDTCN using the LiDAR 6.0 as a source. Figures (g–i) show the VDTCN thresholds using the UAV-derived DEM as a source.

These results confirmed that the optimal parameters for the prediction of riparian zones with different DEMs are not the same and could not be used interchangeably. With the UAV DEM, the optimal flow initiation threshold was 0.50 ha, and the VDTCN threshold was 0.48 m.

Table 1Accuracy of riparian zone prediction with different Flow Initiation (F.I.) and VDTCN thresholds tested for each DEM, as measured using Kappa Coefficient. LiDAR1.2 = LiDAR with a density of 1.2 points m^{-2}; LiDAR 6.0= LiDAR with a density of 6 points m^{-2}.

DEM	Interpolation	F. I. (ha)	VDTCN (m)	Overall Accuracy (%)	Kappa Coefficient
Coarse	2 m	1.5	14.2	75	0.25
LiDAR 1.2	30 cm	1.5	14.2	27	0.04
LiDAR 6.0	30 cm	1.5	14.2	26	0.03
UAV	30 cm	1.5	14.2	26	0.03
LiDAR 1.2	30 cm	0.75	0.40	88	0.63
LiDAR 6.0	30 cm	0.75	0.40	89	0.63
UAV	30 cm	0.75	0.40	88	0.56
LiDAR 6.0	30 cm	0.75	0.48	88	0.64
UAV	30 cm	0.75	0.48	87	0.59
UAV	30 cm	0.5	0.48	88	0.63

4.3.3. Impacts of DEM Resolution on Prediction Accuracy

The accuracies of riparian zone prediction using optimal parameters specific to each DEM are shown in Figure 4.9. As mentioned, KC for coarse resolution DEM was 0.25, which is remarkably lower than the KC of 0.64 and 0.63 achieved by high-resolution DEMs. These results indicated a substantial improvement with high-resolution DEMs (LiDAR and UAV) compared with traditional coarse resolution DEM for delineation of riparian zones. We also found the riparian zone prediction accuracies using high-resolution

DEMs did not have significant differences, and the KC results were practically identical (0.63 and 0.64). The percentage area of the field-surveyed riparian zone being classified as upland using the three DEMs were 22.1%, 23.1%, and 22.8% for LiDAR1.2, LiDAR6.0, and UAV DEM, respectively (Figure 4.9), which reflected nearly identical performance.

Field-surveyed riparian zones together with predicted riparian zones with different DEMs are shown in Figure 4.10. With traditional coarse resolution DEM, large discrepancies between predicted and field-surveyed riparian zones were found over a large part of the north section of the study site (Figure 4.10a). Nonetheless, this area was correctly classified as a riparian zone by all higher resolution DEM including LiDAR or UAV.

On the eastern side of the stream, riparian zones predicted by DEM were substantially larger than the field-surveyed mapped riparian zones (Figure 4.10). However, the riparian zone boundary predicted by UAV and LiDAR 6.0-derived DEMs appeared to better match the field-surveyed riparian zone boundaries compared with LiDAR 1.2. The riparian zone predicted by LiDAR1.2 tended to join the two functional riparian areas located on the eastern side of the stream together (where the higher discrepancy was detected). This must have been due to the higher capability of the UAV and LiDAR 6.0 of detecting the microtopography compared with LiDAR 1.2 and divided the first two wet areas mentioned more clearly. Additionally, due to this higher resolution, the LiDAR 6.0 and UAV-derived DEM identified seasonal stream paths more accurately and therefore represented a wider stream network.

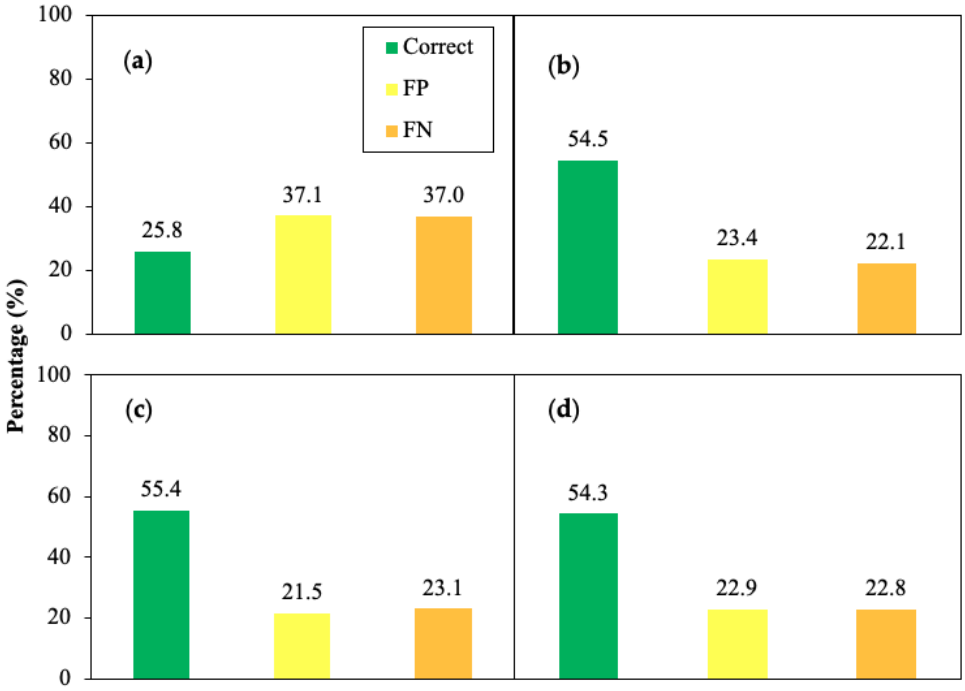

Figure 4.9. Accuracy of the VDTCN predicted functional riparian zones using different DEMs and optimal parameters: (a) mass points coarse resolution DEM, flow initiation = 1.5 ha, VDTCN threshold = 14.2 m; (b) LiDAR 1.2, flow initiation = 0.75 ha, VDTCN threshold = 0.40m; (c) LiDAR 6.0, flow initiation = 0.75 ha, VDTCN threshold =0.48; (d) UAV DEM, flow initiation = 0.5ha, VDTCN threshold = 0.48m. (FP= false positive, indicates upland being predicted as riparian zone; FN = false negative, indicates riparian zone being missclassified as upland).

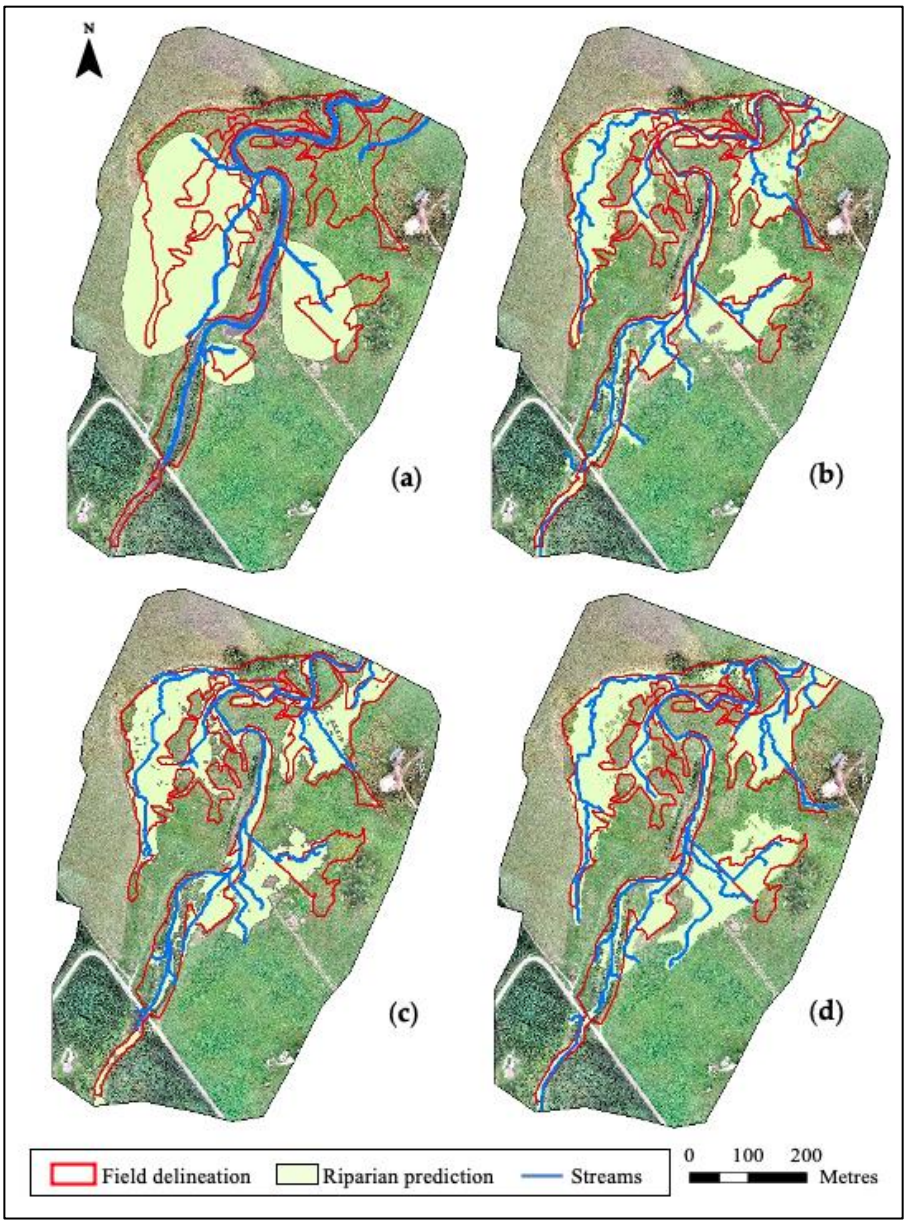

Figure 4.10. Optimal results for the functional riparian zone predicted by the VDTCN raster using each DEM as a source: (a) coarse mass points; (b) LiDAR 1.2p m^{-2}, (c) LiDAR 6.0p m^{-2}, and (d) UAV.

We also found that all DEMs misclassified the riparian zone in the section where the stream was partially restored (bioengineered buffer), located beside the planted forest where the road divides these two areas, along the southern half part of the map (Figure 4.10).

4. 4. Discussion

4.4.1. Impact of the DEM Resolution

We observed significant differences between the accuracy achieved with the traditional coarse resolution DEM compared with higher resolution DEMs. Previous studies also reported that coarse resolution DEMs could not adequately represent the topographic features due to greater terrain surface generalizations (Chang & Tsai, 1991; Thompson *et al.*, 2001; Hancock, 2005; Vaze *et al.*, 2010). This research confirmed that traditional coarse resolution DEMs could not be used for riparian zone delineation in low-order streams. With their higher elevation point density and higher vertical accuracy, higher resolution DEMs derived by LiDAR and UAV can represent the subtle elevation changes in microtopography in greater detail. Previous researchers also pointed out that higher quality vertical information resulted in appreciable improvements in the representation of topographic surface details (Sonneveld *et al*., 2006; Grabs *et al*., 2009; Nobre *et al.*, 2011; Schmid *et al*., 2011; Eltner *et al*., 2016). Higher resolution and accuracy also provided more accurate delineations of hydrologically relevant parameters and more appropriate model outputs (Sonneveld et al., 2006; Grabs *et al.*, 2009; Nobre et al., 2011; Schmid et al., 2011; Eltner *et al*., 2016;). This can ultima tely explain the differences in the VDTCN thresholds used between low resolution and high-resolution DEMs.

4.4.2. VDTCN Raster Performance in Each DEM

Analysis of results highlighted slight differences between the three high-resolution DEMs used in this study. Overall, LiDAR 1.2 displayed a more general stream network grid, whereas the LiDAR 6.0 and UAV provided a more complex detail. Consequently,

relatively shallower areas became less constrained using LiDAR 1.2-derived DEM. This seems to be the reason for the slightly lower correctness achieved compared to using UAV and LiDAR 6.0. These results seem to contradict the concept concluded by previous studies in which smoother topography represented in "coarser" resolutions would reduce the confounding effects of microtopography and increase correctness (Wolock & Price, 1994; Thompson *et al*., 2001; Sørensen & Seibert, 2007; Gillin *et al*., 2015). These studies reported that a more general topography of the landscape represented subsurface groundwater level (GWL) flow paths more accurately than a 1 m DEM.

We found that all three high-resolution DEMs performed poorly in two specific areas. The first area was located within the bioengineered buffer. In this area, a large portion of the riparian area was classified as upland. This section was fenced off and eliminated access by cattle as part of riparian zone conservation. In addition to high vegetation, the herbaceous species were also dense and tall, even during the spring. We suspected that LiDAR might not distinguish the ground surface from the grass cover, so we, therefore, captured the UAV images in early spring. However, the snow-flattened grass formed a surface that was substantially higher than bare ground and caused DEM discrepancies (Figure 4.11). These results indicated that both UAV and LiDAR had successfully isolated the presence of trees but could not distinguish the denser grass. In a future study, landmarks could be set up to estimate grass height manually in order to improve the delineation accuracy.

The second area of discrepancy was found close to the trail created by cattle traveling along a fenced area over the pasture (Figure 4.11). In this section, a large area was predicted to be a riparian zone but was not classified as riparian in the field surveys. We considered

that this area actually should be classified as a riparian zone, but grazing by cattle has removed all riparian vegetation, making it difficult to identify. Therefore, this prediction should not be considered as an error, but the area was a disturbed riparian area.

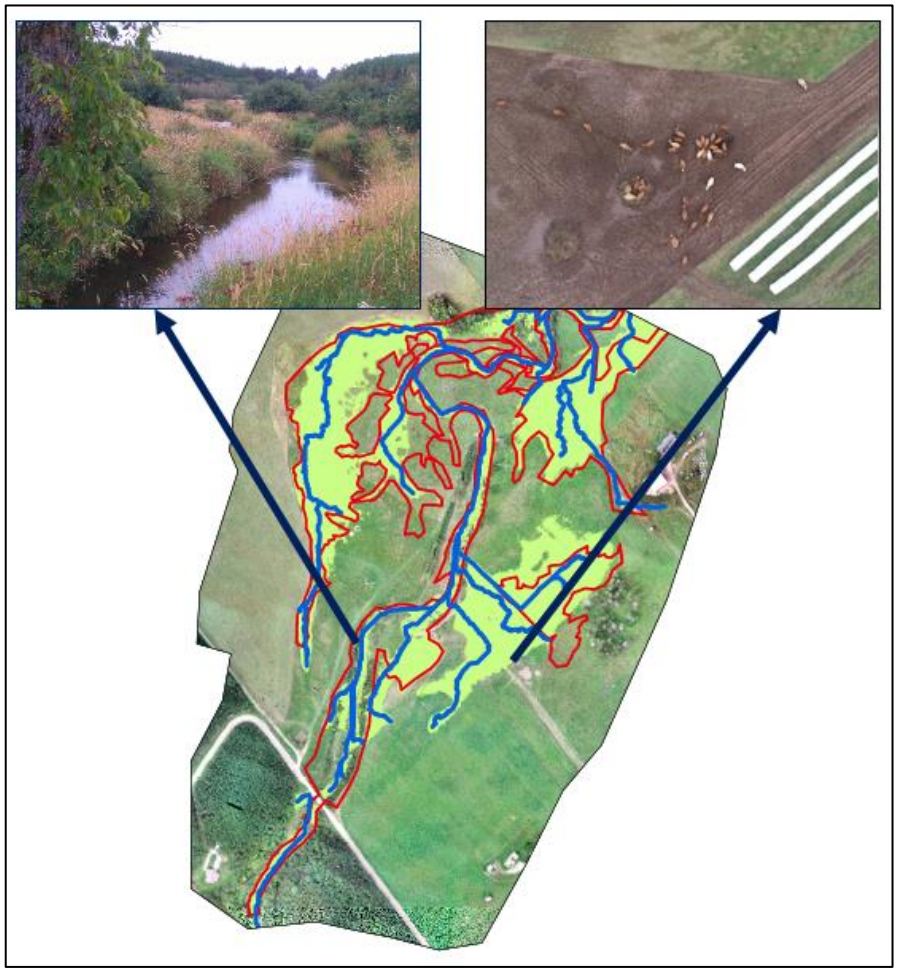

Figure 4.11. Study area showing the two areas of discrepancy. On the left, the stream capture corresponding to summer when LiDAR was collected. On the right, the cattle grazing and trampling beside the fence mentioned (the boundary between grass and grazed area).

4. 5. Conclusions

In this study, we aimed to assess the precision of predicting the extent of the functional riparian zones on a farm to further improve the detection of hydrologically sensitive areas and critical source areas in farmland with similar characteristics, land use, and topography

in southeastern New Brunswick (Canada). To do so, we compared the efficiency of the VDTCN classifying this ecotone when using different topographical models as a source: coarse mass points DEM, obtained with traditional photogrammetry, LiDAR at different resolutions (1.2 and 6 point m^{-2}), and the UAV-derived DEM.

The most noticeable differences were found between the low and high-resolution DEMs (traditional DEM vs. LiDAR and UAV DEMs). The traditional coarse resolution DEM performed poorly in classifying functional riparian zones with KC as low as 0.25 compared with KC = 0.63–0.64 for high-resolution DEMs by LiDAR and UAV. We also found that direct use of optimal parameters (minimal flow initiation threshold and VDTCN threshold) for the coarse resolution DEM to high-resolution DEMs could lead to large errors.

We found that UAV-derived DEM could be used to delineate riparian zones using VDTCN as a classifier for lower-order streams, with comparable accuracy to that of airborne high point cloud density LiDAR. However, tall grassed areas could cause misclassification using LiDAR or UAV methods.

References

Abood, S. A., Maclean, A. L., Mason, L. A. 2012. Modeling riparian zones utilizing DEMS and flood height data. Photogrammetric Engineering & Remote Sensing, 78(3), 259-269.

Beni, L. H., Jones, J., Thompson, G., Johnson, C., Gebrehiwot, A. 2018. Challenges and Opportunities for UAV-Based Digital Elevation Model Generation for Flood-Risk Management: A Case of Princeville, North Carolina. Sensors, 18(11), 3843.

Bock, M., Köthe, R. 2008. Predicting the depth of hydromorphic soil characteristics influenced by ground water. SAGA—Seconds Out, 19, 13-22.

Bouma, J. T. 1983. Hydrology and soil genesis of soils with aquic moisture regimes. Pedogenesis and soil taxonomy/edited by LP Wilding, NE Smeck, and GF Hall.
Brander, L., Schuyt, K. 2004. The economic values of the world's wetlands.

Buchanan, B., Fleming, M., Schneider, R., Richards, B., Archibald, J., Qiu, Z., Walter, M. 2014. Evaluating topographic wetness indices across central New York agricultural landscapes. Hydrology and Earth System Sciences, 18(8), 3279-3299.

Carrivick, J. L., Smith, M. W., Quincey, D. J., Carver, S. J. 2013. Developments in budget remote sensing for the geosciences. Geology Today, *29*(4), 138-143.

Chang, K.-T., Tsai, B.-W. 1991. The effect of DEM resolution on slope and aspect mapping. Cartography and geographic information systems, 18(1), 69-77.

Chaplot, V., Walter, C., Curmi, P. 2000. Improving soil hydromorphy prediction according to DEM resolution and available pedological data. Geoderma, 97(3-4), 405-422.

Congalton, R. G., Birch, K., Jones, R., Schriever, J. 2002. Evaluating remotely sensed techniques for mapping riparian vegetation. Computers and Electronics in Agriculture, 37(1-3), 113-126.

Congalton, R. G., Mead, R. A. 1983. A quantitative method to test for consistency and correctness in photointerpretation. Photogrammetric Engineering and Remote Sensing, 49(1), 69-74.

Cooper, J., Gilliam, J., Daniels, R., Robarge, W. 1987. Riparian areas as filters for agricultural sediment. Soil science society of America journal, 51(2), 416-420.

Elmore, A. J., Julian, J. P., Guinn, S. M., Fitzpatrick, M. C. 2013. Potential stream density in Mid-Atlantic US watersheds. PLoS One, *8*(8), e74819.

Eltner, A., Kaiser, A., Castillo, C., Rock, G., Neugirg, F., Abellán, A. 2016. Image-based surface reconstruction in geomorphometry–merits, limits and developments. Earth Surface Dynamics, 4(2), 359-389.

Escobar Villanueva, J. R., Iglesias Martínez, L., Pérez Montiel, J. I. 2019. DEM generation from fixed-wing UAV imaging and LiDAR-derived ground control points for flood estimations. Sensors, 19(14), 3205.

Fabian, A. J., Klenke, R., Truslow, P. 2020. Improving UAV-Based Target Geolocation Accuracy through Automatic Camera Parameter Discovery. Paper presented at the AIAA Scitech 2020 Forum.

Fonstad, M. A., Dietrich, J. T., Courville, B. C., Jensen, J. L., Carbonneau, P. E. 2013. Topographic structure from motion: a new development in photogrammetric measurement. Earth surface processes and Landforms, 38(4), 421-430.

Fu, B., Li, Y., Wang, Y., Campbell, A., Zhang, B., Yin, S., Zhu, H., Xing, Z., Jin, X. 2017. Evaluation of riparian condition of Songhua River by integration of remote sensing and field measurements. Scientific reports, 7(1), 1-16.

Gallant, J. C., Dowling, T. I. 2003. A multiresolution index of valley bottom flatness for mapping depositional areas. Water resources research, 39(12).

Gillin, C. P., Bailey, S. W., McGuire, K. J., Prisley, S. P. 2015. Evaluation of LiDAR-derived DEMs through terrain analysis and field comparison. Photogrammetric Engineering & Remote Sensing, 81(5), 387-396.

Grabs, T., Seibert, J., Bishop, K., Laudon, H. 2009. Modeling spatial patterns of saturated areas: A comparison of the topographic wetness index and a dynamic distributed model. Journal of Hydrology, 373(1-2), 15-23.

Hancock, G. R. 2005. The use of digital elevation models in the identification and characterization of catchments over different grid scales. Hydrological Processes: An International Journal, 19(9), 1727-1749.

Hill, A. R., Cardaci, M. 2004. Denitrification and organic carbon availability in riparian wetland soils and subsurface sediments. Soil Science Society of America Journal, 68(1), 320-325.

Holmes, K. L., Goebel, P. C., Morris, A. E. 2010. Characteristics of downed wood across headwater riparian ecotones: integrating the stream with the riparian area. Canadian journal of forest research, 40(8), 1604-1614.

Ilhardt, B. L., Verry, E. S., Palik, B. J. 2000. Defining riparian areas. Forestry and the riparian zone, Orono, Maine, 7-14.

Jacobs, P. M., West, L. T., Shaw, J. N. 2002. Redoximorphic features as indicators of seasonal saturation, Lowndes County, Georgia. Soil Science Society of America Journal, 66(1), 315-323.

Jeziorska, J. (2019). UAS for wetland mapping and hydrological modeling. Remote Sensing, 1*1*(17), 1997.

Johansen, K., Grove, J., Denham, R., Phinn, S. R. 2013. Assessing stream bank condition using airborne LiDAR and high spatial resolution image data in temperate semirural areas in Victoria, Australia. Journal of Applied Remote Sensing, 7(1), 073492.

Johansen, K., Phinn, S. 2006. Mapping structural parameters and species composition of riparian vegetation using IKONOS and Landsat ETM+ data in Australian tropical savannahs. Photogrammetric Engineering & Remote Sensing, 72(1), 71-80.

Johansen, K., Phinn, S., Dixon, I., Douglas, M., Lowry, J. 2007. Comparison of image and rapid field assessments of riparian zone condition in Australian tropical savannas. Forest Ecology and Management, 240(1-3), 42-60.

Kokulan, V., Akinremi, O., Moulin, A. P., Kumaragamage, D. 2018. Importance of terrain attributes in relation to the spatial distribution of soil properties at the micro scale: a case study. Canadian Journal of Soil Science, 98(2), 292-305.

Krisanski, S., Taskhiri, M. S., Turner, P. 2020. Enhancing methods for under-canopy unmanned aircraft system based photogrammetry in complex forests for tree diameter measurement. Remote Sensing, 12(10), 1652.

Kuželka, K., Surový, P. 2018. Mapping forest structure using UAS inside flight capabilities. Sensors, 18(7), 2245.

Likens, G. E. 2010. Lake ecosystem ecology: a global perspective: Academic Press.

Londo, G. 1976. The decimal scale for releves of permanent quadrats. Vegetatio, 33(1), 61-64.

Malone, B. P., Odgers, N. P., Stockmann, U., Minasny, B., McBratney, A. B. 2018. Digital mapping of soil classes and continuous soil properties. In Pedometrics (pp. 373-413): Springer.

Meehan, W. R., Swanson, F. J., Sedell, J. R. 1977. and Their Food Supply., 2. Paper presented at the Importance, Preservation and Management of Riparian Habitat: A Symposium, Tucson, Arizona, July 9, 1977.

Murphy, P. N. C., Ogilvie, J., Arp, P. 2009. Topographic modelling of soil moisture conditions: a comparison and verification of two models. European Journal of Soil Science, 60(1), 94-109.

Naiman, R. J., Décamps, H. 1997. The ecology of interfaces: riparian zones. Annual review of Ecology and Systematics, 28(1), 621-658.

Nobre, A. D., Cuartas, L. A., Hodnett, M., Rennó, C. D., Rodrigues, G., Silveira, A., Saleska, S. 2011. Height Above the Nearest Drainage–a hydrologically relevant new terrain model. Journal of Hydrology, 404(1-2), 13-29.

O'Callaghan, J. F., Mark, D. M. 1984. The extraction of drainage networks from digital elevation data. Computer vision, graphics, and image processing, 28(3), 323-344.

Peterson, B. J., Wollheim, W. M., Mulholland, P. J., Webster, J. R., Meyer, J. L., Tank, J. L., Martí, E., Bowden, W. B., Valett, H. M., Hershey, A. E., McDowell W. H., Dodds, W. K., Hamilton, S. K., Gregory, S., Morrall, D. D. 2001. Control of nitrogen export from watersheds by headwater streams. Science, 292(5514), 86-90.

Poppenga, S. K., Worstell, B. B., Stoker, J. M., Greenlee, S. K. 2010. Using selective drainage methods to extract continuous surface flow from 1-meter lidar-derived digital elevation data: U.S. Geological Survey Scientific Investigations Report 2010–5059, 12 p.

Rahman, M. M., McDermid, G. J., Strack, M., Lovitt, J. 2017. A new method to map groundwater table in peatlands using unmanned aerial vehicles. Remote Sensing, 9(10), 1057.

Rivenbark, B. L., Jackson, C. R. 2004. Concentrated flow breakthroughs moving through silvicultural streamside management zones: southeastern piedmont, USA 1. JAWRA Journal of the American Water Resources Association, 40(4), 1043-1052.

Rogers, S. R., Manning, I., Livingstone, W. 2020. Comparing the spatial accuracy of Digital Surface Models from four unoccupied aerial systems: Photogrammetry versus LiDAR. Remote Sensing, 12(17), 2806.

Schmid, K. A., Hadley, B. C., Wijekoon, N. 2011. Vertical accuracy and use of topographic LIDAR data in coastal marshes. Journal of Coastal Research, 27(6A), 116-132.

Sedell, J. R., Beschta, R. L. 1991. Bringing Back the'Bio'in Bioengineering. Paper presented at the Fisheries Bioengineering Symposium: American Fisheries Society Symposium 10.

Shamshiri, R. R., Hameed, I. A., Balasundram, S. K., Ahmad, D., Weltzien, C., Yamin, M. 2018. Fundamental research on unmanned aerial vehicles to support precision agriculture in oil palm plantations. Agricultural Robots-Fundamentals and Application, 91-116.

Smith, M. P., Schiff, R., Olivero, A., MacBroom, J. 2008. The active river area: A conservation framework for protecting rivers and streams. The Nature Conservancy, Boston, MA.

Sonneveld, M., Schoorl, J., Veldkamp, A. 2006. Mapping hydrological pathways of phosphorus transfer in apparently homogeneous landscapes using a high-resolution DEM. Geoderma, 133(1-2), 32-42.

Sørensen, R., Seibert, J. 2007. Effects of DEM resolution on the calculation of topographical indices: TWI and its components. Journal of Hydrology, 347(1-2), 79-89.

Swanson, F., Gregory, S., Sedell, J., Campbell, A. 1982. Land-water interactions: the riparian zone.

Swanson, S., Miles, R., Leonard, S., Genz, K. 1988. Classifying rangeland riparian areas: the Nevada task force approach. Journal of Soil and Water Conservation, 43(3), 259-263.

Thompson, J. A., Bell, J. C., Butler, C. A. 2001. Digital elevation model resolution: effects on terrain attribute calculation and quantitative soil-landscape modeling. *Geoderma, 100*(1-2), 67-89.

Vaze, J., Teng, J., Spencer, G. 2010. Impact of DEM accuracy and resolution on topographic indices. Environmental Modelling & Software, 25(10), 1086-1098.

Werren, G., Arthington, A. 2002. The assessment of riparian vegetation as an indicator of stream condition, with particular emphasis on the rapid assessment of flow-related impacts. Landscape Health of Queensland, 194-222.

White, B., Ogilvie, J., Campbell, D. M., Hiltz, D., Gauthier, B., Chisholm, H. K. H., Wen, H. K., Murphy, P. N. C., Arp, P. A. 2012. Using the cartographic depth-to-water index to locate small streams and associated wet areas across landscapes. Canadian Water Resources Journal/Revue canadienne des ressources hydriques, 37(4), 333-347.

Wilson, A. M., Evans, T., Moore, W., Schutte, C. A., Joye, S. B., Hughes, A. H., Anderson, J. L. 2015. Groundwater controls ecological zonation of salt marsh macrophytes. Ecology, 96(3), 840-849.

Wolf, R., Dewitt, A. 2000. Elements of Photogrammetry with Application in GIS, 3rd editrion. The university of Wisconsin, Madiso*n*.

Wolock, D. M., Price, C. V. 1994. Effects of digital elevation model map scale and data resolution on a topography-based watershed model. Water Resources Research, 30(11), 3041-3052.

Zhang, W., Montgomery, D. R. 1994. Digital elevation model grid size, landscape representation, and hydrologic simulations. Water resources research, 30(4), 1019-1028.

CHAPTER 5: Summary, Conclusions, Applications and Future Research

5. 1. Summary

This study aimed to provide the first steps toward the replacement of paper-based field guidelines, which provide some recommendation for the design of variable buffer zones in the province of New Brunswick. This study has become a relevant contribution to the Riparian Function Assessment Protocol (RFAP), a project that aims to include soil nutrient turnover, differences in plant functional communities, earthworm population, and soil carbon as indicators of soil health, and potential changes in the aquatic macroinvertebrate community. As a result, this would ultimately address environmental concerns and help mitigate the effects of agricultural practices on surface water. For the purpose of the functional riparian delineation, we incorporated the UAV-derived DEM to the provincial mass points and LiDAR topographic digital sources available online. We have demonstrated that UAV provided a rapid and feasible method to satisfy the demands of this project at a field scale.

From the economic perspective, the cost of UAV LiDAR equipment has been estimated as 30 times more than the photogrammetric survey gear according to Chen *et al*., (2020). On the other hand, the cost of UAV imagery has also been reported as more economic compared with satellite imagery ($1,000 vs $3,000, respectively). Additionally, it can provide higher detail, controlled accuracy, and user friendliness, and a short time frame for data collection and processing makes the method repeatable (Manfreda *et al*., 2018).

5. 2. Conclusions

5.2.1. Optimal Parameters for Using Consumer-Grade Unmanned Aerial Vehicles to Produce High Resolution Digital Surface Model (DSM)

Concerning spatial resolution, flight above ground level (AGL) is an important parameter influencing the degree of detail achieved in the 2D mapping and Digital Surface Model for analysis in a forestry context. We explored low oblique imagery acquisition using different off-Nadir UAV low-oblique camera angles (10, 20, and 30 degrees off-Nadir) with different image overlap rates (90, 80, 60 and 45%). We observed how higher oblique camera angles increased the pixel size in 2D maps, distorted the map scale, and reduced uniformity in mapped landscape features. However, these angles mapped a significantly larger area than 10 degrees. Higher image overlap rates (80 and 90%) also mapped larger areas than low image overlap rates (45 and 60%).

We observed a reduction of five times in point cloud density when the flight height was increased from 30 to 70 meters with equal camera angle and image overlap rate. We also observed an increase of 200% in point density when the camera angle was tilted from 30 degrees to 10 degrees with the highest overlap rate tested (90%). However, this difference was not as obvious when the image overlap was low (45 and 60%).

The results herein presented indicate that the variable height was best estimated with DSM using an image overlap rate of 60%. However, this was caused by the higher point dispersion representing the surface of the box in the DSM. Secondly, the area was best estimated when using a tilt angle of 20 degrees and an image overlap of 90% and the accuracy dropped sharply when low image overlap rates were used (60 and 45%). Also, the cubical shape of the box was highly deformed in DSM when low image overlap rates

were used. This could explain why volume estimations were higher when 80% image overlap was used and were inaccurate when setting image overlaps of 45% and 60%.

5.2.2. Using Unmanned Aerial Vehicle and LiDAR-derived DEMs to Estimate Channels of Small Tributary Streams.

Stream bank location and condition is an important physical form indicator for streams related to the environmental condition of riparian corridors (Johansen *et al*., 2013). Microtopographic features, often anthropogenic at submetre scale, can be prevalent in agricultural catchments, and influence diffuse pathways of surface runoff that can entrain pollutants (Buchanan *et al*., 2013a; Lane *et al*., 2009). Therefore, they play important roles in delineating hydrologically sensitive areas (HSAs) and critical source areas (CSAs) in agricultural catchments, particularly in areas intersecting the main stream (Thomas *et al*., 2017).

We used the DEMs available in the Service New Brunswick Geospatial Datasets (coarse mass points acquired with traditional photogrammetry and LiDAR collected at 1.2 and 6 points m^{-2}). The mass points DEM was interpolated at 2 meters resolution and the LiDAR was interpolated at 30 cm. Images collected in May 2019 with UAV were used to generate the photogrammetric DEM interpolated at 30 cm. Afterwards, we derived the Slope Gradient (SG) raster and the Vertical Slope Position (VSP) raster for all topographic models. When the Slope Gradient method was used, the UAV-derived DEM achieved the highest accuracy in the mapping of the stream channel and defining the stream bank locations, with a MSE of 2.33 m (KGE = 82%), followed by LiDAR 6.0 (MSE = 5.27 and KGE = 70%) and LiDAR 1.2 (MSE = 7.87 m and KGE = 67%). The coarse-resolution

DEM was unable to accurately predict this parameter and the error was significantly higher, at MSE = 26.76 m (KGE = 34%). The application of a filtering method to post-process the classified topographic model could significantly improve the prediction accuracy for LiDAR-based DEMs. The value of the MSE reduced from 7.87 to 3.33 (KGE = 80%) for LiDAR 1.2, and from 5.27 to 1.91 (KGE = 85%) for LiDAR 6.0. The value of MSE for the UAV-derived DEM was modestly reduced from 2.33 to 1.81 (KGE = 86%).

On the other hand, we observed a decrease in accuracy among the higher-resolution DEMs tested, when the VSP method was used. The LiDAR 1.2 was able to predict the stream bank with a MSE of 9.70 m (KGE = 67%), followed by LiDAR 6.0 (MSE = 11.45 and KGE = 64%) and UAV-derived DEM (MSE = 15.12 and KGE = 53%). Fewer rugged imperfections were represented in the first DEM mentioned due to lower point terrain detail, which increased the performance. On the other hand, light/water properties significantly affected the stream channel on the UAV-derived DEM and decreased the accuracy of this raster remarkably. Even though the mass points DEM provided significantly better results when using the VSP (MSE=20.78) than SG raster, this topographic model did not perform precisely in estimating the water surface (KGE = 28%).

The present work indicated that a UAV-derived DEM could be used to predict bank slope position using the Slope Gradient as classifier for lower-order streams, with higher accuracy than airborne high point cloud density LiDAR. As opposed to LiDAR, UAVs have the capability of accurately defining the matrix of this ecosystem, from water surface, stream bank, riparian zone, and uplands. However, highly densely vegetated areas could

lead to errors due to the limitations of the photogrammetry method of the UAV in detecting bare ground under dense canopy.

5.2.3. Improved Accuracy of Riparian Zone Mapping Using Near Ground Unmanned Aerial Vehicle and Photogrammetry Method.

The effectiveness of riparian conservation depends largely on mapping technique, which implies precise geographic delineation of a zone where impacts of agriculture and forestry are limited. The riparian zone can be mapped by predicting the interface between the permanently wet, or wetter areas due to position in the landscape using terrain attributes, such as slope gradient and elevation (Ilhardt *et al*., 2000; Chaplot *et al*., 2000) and/or the presence of a permanently high or fluctuating water table near the soil surface.

We generated the Vertical Distance To Channel Network (VDTCN) raster using the DEMs detailed in Chapter 3. We optimized the flow initiation and VDTCN thresholds for the coarse mass points DEM, and it only achieved 25% agreement (as measured using the Kappa Index) in classifying riparian zones indicating poor correctness. Furthermore, we observed that minimum flow accumulation and VDTCN thresholds applied for the coarse mass points DEM, were inadequate to be applied with higher resolution DEMs. We invested further efforts in optimizing minimum flow initiation and VDTCN thresholds for higher resolution DEMs. However, we observed no remarkable differences between the higher resolution DEMs (LiDAR and UAV) in the correctness percentage and they achieved 63% agreement in the Kappa Index (K.I.). Nonetheless, the LiDAR 6.0 provided slightly higher terrain exactness in classifying the field-verified riparian ecotones (K.I.=64%) located on the eastern side of the stream. The higher quality vertical

information of this topographic model constrained remarkably shallower wet areas, thereby increasing the precision and specificity of this method.

There were two sections where the higher resolution DEMs showed discrepancies with the field-verified riparian area; the section where the bio-engineered buffer was implemented and a portion of land where cattle grazed more intensely. The first one was unable to be classified by the DEM due to elevation differences and inaccuracies caused by the streambank vegetation. The second one was located over an area that belonged to riparian zone but suffered from periodic grazing, which we considered as disturbed riparian area.

5. 3. Applications

In the present work, we have proved that UAVs can reliably estimate the height, the area, and the volume of landscape features, showing the influence of image overlap and UAV camera angle. This would have an application in silviculture practices, monitoring the recovery of disturbed areas over time (i. e. clearcuts, wildfire, blow down areas, disease maps, inventory resources, landslides, etc).

Finer resolution DEMs and derived hydrologic maps could be used as a source to increase the resolution of current digital soil maps. This can be achieved by applying machine-based regression modelling (i. e. random forest or cubist) to predict continuous soil attribute mapping at finer a resolution.

The increased soil compaction located in areas of intense grazing can lead to a high propensity of generating surface run off, known as hydrologically sensitive areas (HSA). In agricultural landscapes, this can lead to a rise in sediment load and fertilizer input to waterways if proper buffering is not implemented. The finer resolution DEM is able to

capture the microtopographic differences along fenced areas, and can identify areas of concentrated run off. Knowing the precise location of these areas could help landowners to apply management strategies to mitigate this concern.

Images collected with UAV can be used to estimate the surface occupied by water in a watershed over time. This can help predict groundwater levels during different seasons based on surface water levels. This knowledge could provide some guidance for more efficient applications of fertilizers and pesticides, in order to reduce subsurface water pollution.

Another useful method for stream ecology management is the production of maps depicting erosion sensitive areas (steep bank slopes and areas of bank instability), which are easily produced with DEM (Slope Gradient or Vertical Slope Position). Increased sediment input into waterways leads to a rise in water turbidity and can cause habitat impairment in lotic ecosystems (Henley *et al.*, 2000; Smiley *et al.*, 2009). Direct quantification of erosion and sedimentation processes is one of the key factors in improving riverine ecology (Erős & Lowe, 2019).

For optimal UAV-derived DEMs in agricultural landscapes, images captured in spring provided better accuracy, since vegetation may cause less distortion of the topographic representation. Using these topographic models as a source could also provide means to research how tillage can significantly modify overland flow in cultivated areas over different landscapes. A study lead by Hyväluoma (2013) introduced a flow-routing algorithm focused on anisotropic roughness resulting from tillage to quantify soil loss.

One direct application of this study would be the rapid implementation of this method to multiple field scales, with similar characteristics of climate, soil parent material, land

use, and stream orders within a watershed. Identifying these ecosystems locally could become, eventually, a rapid method to start improving stream water and groundwater quality at a watershed scale.

5. 4. Future research

Future research should be focused on solving the limitations of this study. Complementary to the work presented in Chapter 2, image distortion could be analyzed using the raster image quality examination applying Edge analysis. Lim and others (2018) used a high quality camera (Sony A5100 equipped with 6000 x 4000 resolution sensor) to find optimal UAV flight heights and showed optimal altitude ranges of image sharpness. They found that the exact optimal range varied between images taken at different weather conditions. However, they did not use any image processing software (i. e. Pix4D or Agisoft Photoscan) to compare how image overlap, camera angle, pre-planned grid design, and grid orientation affected the image quality. This would be an interesting field to investigate for UAV consumer-grade cameras to provide some guidance regarding image definition, contrast range, gradation, geometric distortion, and noise. Alternatively, the UAV geolocation accuracy could be investigated using GPS points and different image overlaps in order to provide an assessment of how this geolocation is affected by different image acquisition datasets. Consequently, this could improve efficiency in the way images are viewed, received, captured, and stored (Chandler, 2013).

Supplementary to the tests undergone in Chapter 2, previous studies have explored the reconstruction of a map using a combination of Nadir and off-Nadir images (Vacca *et al.*, 2017; Lingua *et al.*, 2017). Lingua and others reported that VisualSfM had major problems

in areas with more irregular geometries, such as rich vegetation present in the study area. Similarly, where our experiment was conducted, we observed that the point cloud performed more noisilyin the stream channel at points where they were surrounded by dense high vegetation. Even though their purpose was focused on urban building reconstruction, this technique has not been applied in vegetation studies that we are aware of. Therefore, it may be interesting to test the processing of types of image acquisition to strengthen the photogrammetric block.

Artificial intelligence and machine learning algorithms could be tested in order to accelerate the human point cloud edition, i. e., improve the DEM by discerning vegetation from bare ground features. Also, flattening the water level surface within the stream channel by smoothing the excessive noise (reported in Chapter 3) is urgently needed. Where results of this algorithm were successful, we would encourage acquiring near ground aerial data using double parallel flight grid lines perpendicular to each other (double grid mission). Thus, UAV would be registering a higher density of points and, presumably, be able to capture higher detail of the stream bank geomorphology (partially covered by high vegetation).

Also, a further comparison could be testing how the point cloud density affects the terrain detail in the DEM, using parallel gridlines contrasted with parallel and perpendicular gridlines. This could provide some evidence of the terrain curvature analysis and the effects on hydrologic representation (i. e. stream network) performed by these two different flight modes.

Regarding stream network modelling, breaching DEM obstructions has been reported to be more appropriate than filling the sinks (Garbrecht *et al.*, 1996; Martz & Garbrecht, 1999a). This could be an alternative method to be explored in order to generate the DEM stream network prior to using the VDTCN and VSP rasters. Obstruction breaching has been claimed to be particularly effective in DEMs representing relatively flat areas. This is because sinks caused by flow path obstruction are more prevalent in these digital landscape representations.

References

Alidoost, F., Arefi, H. 2017. Comparison of UAS-based photogrammetry software for 3d point cloud generation: a survey over a historical site. ISPRS Annals of Photogrammetry, Remote Sensing and Spatial Information Sciences. IV-4/W4. 55-61. 10.5194/isprs-annals-IV-4-W4-55-2017.

Buchanan, B. P., Falbo, K., Schneider, R. L., Easton, Z. M., Walter, M. T. 2013a. Hydrological impact of roadside ditches in an agricultural watershed in Central New York: implications for non-point source pollutant transport. Hydrol.Processes 27, 2422–2437.

Chandler, D. 2013. Seven Challenges in Image Quality Assessment: Past, Present, and Future Research. ISRN Signal Processing. https://doi.org/10.1155/2013/905685

Chaplot, V., Walter, C., Curmi, P. 2000. Improving soil hydromorphy prediction according to DEM resolution and available pedological data. Geoderma, 97, 405-422.

Chen, S., Johnson, F., Drummond, C., Glamore, W. 2020. A new method to improve the accuracy of remotely sensed data for wetland water balance estimates. Journal of Hydrology: Regional Studies, 29, 100689.

Erős, T., Lowe, W.H. The Landscape Ecology of Rivers: from Patch-Based to Spatial Network Analyses. Curr Landscape Ecol Rep 4, 103–112. https://doi.org/10.1007/s40823-019-00044-6

Garbrecht, J., Starks, P. J., Martz, L. W. 1996. New Digital Landscape Parameterization Methodologies. In Proceedings of AWRA Annual Symposium on GIS and Water Resources, AWRA, September 22-26, 1996, Fort Lauderdale, FL, p. 357-365.

Henley, W., Patterson, M., Neves, R., Lemly, A. 2000. Effects of sedimentation and turbidity on lotic food webs: a concise review for natural resource managers: Reviews in Fisheries Science, V. 8, no. 2, p. 125-139.

Hyväluoma, J., Lilja, H. J., Turtola, E. 2013. An anisotropic flow-routing algorithm for digital elevation models. Computers & Geosciences. 60. 81-87. https://doi.org/10.1016/j.cageo.2013.07.012

Ilhardt, B. L., Verry, E. S., Palik, B. J. 2000, Defining riparian areas, in E. S. Verry, J. W. Hornbeck and C. A. Dolloff (eds.), Riparian Management in Forests of the Continental Eastern United States, Lewis Publishers, Boca Raton, FL, pp. 23–42.

Jeziorska, J. 2019. UAS for Wetland Mapping and Hydrological Modeling. Remote. Sens., 11, 1997.

Johansen, K., Grove, J., Denham, R., Phinn, S. R. 2013. Assessing stream bank condition using airborne LiDAR and high spatial resolution image data in temperate semirural areas in Victoria, Australia, Journal of Applied Remote Sensing 7(1), 073492 (28 October 2013). https://doi.org/10.1117/1.JRS.7.073492

Lane, S. N., Reaney, S. M., Heathwaite, A. L. 2009. Representation of landscape hydrological connectivity using a topographically driven surface flow index. Water Resour. Res. 45, W08423.

Lim, P.-C., Kim, T., Na, S.-I., Lee, K.-D., Ahn, H.-Y., Hong, J. 2018. Analysis of UAV image quality using edge analysis. ISPRS - International Archives of the Photogrammetry, Remote Sensing and Spatial Information Sciences. XLII-4. 359-364. 10.5194/isprs-archives-XLII-4-359-2018.

Lingua, A., Noardo, F., Spanò, A., Sanna, S., Matrone, F. 2017. 3D Model generation using oblique images acquired by UAV. Int. Arch. Photogramm. Remote Sens. Spatial Inf. Sci., XLII-4/W2, 107–115, https://doi.org/10.5194/isprs-archives-XLII-4-W2-107-2017

Liu, J., Skidmore, A. K., Jones, S. D., Wang, T., Heurich, M., Zhu, X., Shi, Y. 2018. Large off-nadir scan angle of airborne LiDAR can severely affect the estimates of forest structure metrics. ISPRS journal of photogrammetry and remote sensing, 136, 13-25. https://doi.org/10.1016/j.isprsjprs.2017.12.004

Manfreda, S., McCabe, M., Miller, P., Lucas, R., Pajuelo Madrigal, V., Mallinis, G., Ben Dor, E., Helman, D.; Estes, L., Ciraolo, G., Müllerová, E., Tauro, F., De Lima, M. I., De Lima, J. L. M. P., Maltese, A., Frances, F., Caylor, K., Kohv, M., Perks, M., Ruiz-Perez, G., Su, Z., Vico, G., Toth, B. 2018. On the use of unmanned aerial systems for environmental monitoring. Remote Sens., 10, 641. https://doi.org/10.3390/rs10040641

Martz, L.W., Garbrecht, J. 1999. An Outlet Breaching Algorithm for the Treatment of Closed Depressions in a Raster DEM. Computers & Geosciences (in press).

Rogers, S., Manning, I., Livingstone, B. 2020. Comparing the Spatial Accuracy of Digital Surface Models from Four Unoccupied Aerial Systems: Photogrammetry Versus LiDAR. Remote Sensing. 12. 2806. 10.3390/rs12172806.

Smiley, P., Knight, S., Shields, D., Cooper, C. 2009. Influence of gully erosion control on amphibian and reptile communities within riparian zones of channelized streams: Ecohydrology, V. 2, p. 303-312.

Thomas, I. A., Jordan, P., Shine, O., Fenton, O., Mellander, P. E., Dunlop, P., Murphy P. N. C., 2017. Defining optimal DEM resolutions and point densities for modelling hydrologically sensitive areas in agricultural catchments dominated by microtopography. Int. J. Appl. Earth Obs. Geoinf. 54, 38–52.

Vacca, G., Dessi, A., Sacco, A. 2017. The Use of Nadir and Oblique UAV Images for Building Knowledge. ISPRS Int. J. Geo-Inf. 2017, 6(12), 393; https://doi.org/10.3390/ijgi6120393

Curriculum Vitae

Candidate's full name: Joan Grau Martin

Universities attended: Autonomous University of Barcelona: BSc in Biology, 2011
University of New Brunswick: MSc in Forestry, 2021

Publications:

Grau, J.; Liang, K.; Ogilvie, J.; Arp, P.; Li, S.; Robertson, B.; Meng, F.-R. Using Unmanned Aerial Vehicle and LiDAR-derived DEMs to Estimate Channels of Small Tributary Streams. *Remote Sens.* 2021, 3380. https://doi.org/10.3390/rs13173380

Grau, J.; Liang, K.; Ogilvie, J.; Arp, P.; Li, S.; Robertson, B.; Meng, F.-R. Improved Accuracy of Riparian Zone Mapping Using Near Ground Unmanned Aerial Vehicle and Photogrammetry Method. *Remote Sens.* **2021**, *13*, 1997. https://doi.org/10.3390/rs13101997

Teaching assisted courses at UNB:

-*Autecology of Vegetation (shrubs)*. Mentored students on vegetation identification features (Sep – Dec 2018).

-*Advanced GIS for Forestry*. Mentored students on interpretation of GIS analysis (Jan-Apr 2018).

Work experience:

Research assistant | University of New Brunswick | SEP 2019

Mapped eelgrass density using drone technology along shoreline of James Bay for Canada Goose habitat restoration in collaboration with the local Cree, Wemindji and Chisasibi indigenous community.

Research assistant | Scenesharp Technologies Inc | MAY 2019 – APRIL 2020

Identified higher vegetation species using drone technology to validate externally-derived satellite imagery and predicted tree species via implementation of LiDAR technology (i.e. DEMs and DSMs) in collaboration with the project: SST-NBIF Voucher: Dual-Camera Video Prototyping and Processing (Professor: Dr. Yun Zhang).

Teaching lab assistant | Autonomous University of Barcelona (UAB), Catalonia | MAR-MAY 2011

Mentored students on interpretation of biology cell lab results from microbiology experiments.

Anthropology / Forensic lab assistant | Autonomous University of Barcelona, Catalonia | NOV 2010-FEB 2011

Collaborated with doctoral-level anthropological research team on reconstructing human skeletons from museum collections. Variables measured to detect potential illnesses, age and sex determination, and attributing identity of bone fragments.

Forestry research assistant | Autonomous University of Barcelona (Uab) | JUN – SEP 2005

Collaborated with doctoral research in the Ecology and Forestry Research Department (CREAF) analyzing regeneration of vegetation communities following forest fires. Tasks included:

-Botanical surveys for tree identification purposes and wetland indicators

-Collected samples to analyze and quantify chemical nutrient elements to compare soil richness in different forest stands.

Conferences and Posters Presented:

(1) Grau, J. 2018. Riparian Management and Use of UAV in Mapping, Fredericton Research and Development Centre Envirothon Seminars, Fredericton, NB.

(2) Grau, J. 2018. Riparian zone delineation based on geospatial data set analysis. AAFC Seminar, Fredericton, NB.

(3) Grau, J. 2018. Functional Riparian Areas Delineation Based Using Geospatial Datasets. 5th Natural Channels Systems, Guelph, ON (Virtual Poster presentation).

(4) Grau, J. 2018. Functional Riparian Areas Delineation Based Using Geospatial Datasets. Vancouver Convention Centre for the 4th Future Forestry Leaders Symposium (FFLS), November 2018. (Virtual Poster presentation).

(5) Grau, J. 2018. Stream boundaries prediction using geospatial data set analysis. Graduate Research Conference, 2018, Fredericton, NB.

(6) Grau, J. 2019. Functional Riparian Areas Delineation Using Geospatial Datasets. Graduate Research Conference 2019, Fredericton, NB.